Numerical Analysis of Drag Reduction in Channel Flow by Traveling Wave-Like Blowing and Suction

March 2012

Hiroya MAMORI

School of Science for Open and Environmental Systems

Graduate School of Science and Technology

Keio University

This thesis is available as a pdf file.
Please feel free to contact me by e-mail: “mamori.hiroya@gmail.com”.

Acknowledgements

I am deeply grateful to my supervisor Professor Koji Fukagata. He has always supported, helped, and encouraged me concerning not only the research topics but also my master and doctor life. I would not have completed my Ph .D study without him. Again, I would like to show my true gratitude.

I appreciate Professor Shinnosuke Obi, Professor Kenji Yasuoka and Professor Takeshi Yokomori for invaluable discussion on the present thesis. Especially, I would like to show my gratitude to Professor Shinnosuke Obi for fruitful discussion on various topics since I was an undergraduate student. I would like to show my gratitude to Professor Shigeaki Masuda who was my supervisor when I was the undergraduate student. I greatly appreciate Professor Jerome Hoepffner of UPMC for supporting me at my international internship and Professor Shinntaro Takeuchi of Osaka University for discussion. I also appreciate Professor Nobuhide Kasagi, Professor Yosuke Hasegawa, and Professor Kaoru Iwamoto for fruitful discussion at a series of the meetings of 'Grant-in-Aid for Scientific Research (A) (Grant No. 20246036)'.

I would like to show gratitude to the members of Masuda-Obi-Fukagata laboratories for making my research life enjoyable. In particular, I thank to Drs. Yoshitsugu Naka and Rio Yokota for teaching and helping me all the time. In addition, I was happy to work with Yukinori Kametani, Kosuke Higashi, Rio Nakanishi, and Yasuhito Murai, with whom I spent much time together or wrote papers with a lot of fun.

Of course, I do appreciate to my family for supporting me all the time.

This work has been financially supported by Japan Society for the Promotion of Science (JSPS), Grant-in-Aid for JSPS Fellows, 23·3928, 2011 and

in part by Grant in Aid for the Global Center of Excellence Program for ”Center for Education and Research of Symbiotic, Safe and Secure System Design” from the Ministry of Education, Culture, Sport, and Technology in Japan.

Abstract

Flow control to reduce skin-friction drag of wall-turbulence is worth studying not only from the scientific point of view, but also the industrial one. The objective of this thesis is to clarify the skin-friction drag reduction mechanism of a traveling wave-like blowing/suction control (Min et al., 2006) in a fully developed laminar and turbulent channel flows by means of numerical analysis. This control is very simple, while it induces a large amount of drag reduction without using any sensors.

For the laminar flow, an employed linear analysis perfectly reproduces Min *et al.*'s result: the skin-friction drag decreases and increases when the wave travels to upstream and downstream directions, respectively. A detailed phase analysis reveals the drag reduction mechanism. An analogy between the present control and Stokes' second problem is also found. The mechanism and analogy are confirmed for wider range of parameters.

Direct numerical simulation is performed to investigate the effect of traveling wave in a low Reynolds number turbulent flow. When an upstream traveling wave decreases the skin-friction drag, a negative Reynolds shear stress appears in the region near the wall. The generation mechanism of this negative Reynolds shear stress is revealed by a three component decomposition and a phase analysis: the similar explanation to the laminar flow control applies also for the turbulent flow. The control effect is compared with an opposition control, a suboptimal control and a traveling wave-like wall-normal forcing. Additionally, a numerical scheme for computation of Reynolds stress budget which is consistent with a second order energy conservative finite difference method is also proposed.

The control effect is also investigated in relatively high Reynolds number turbulent flows by means of large eddy simulation with the coherent structure model (Kobayashi, 2005). The effectiveness of skin-drag reduction of the control is found to decrease as increasing the Reynolds number.

Contents

List of Figures

List of Tables

Nomenclature

Roman Symbols

$\mathbf{A}$	system matrix
a	amplitude of traveling wave
c	wavespeed of traveling wave
C_f	skin-friction coefficient
$C_{nm}, P_{nm}, T_{nm}, \Psi_{nm}, \Phi_{nm}, D_{nm}, \varepsilon_{nm}$	convection, production, turbulent diffusion, pressure-strain, pressure-diffusion, viscous diffusion, viscous dissipation terms of transport equation of Reynolds stress, $\overline{u_n' u_n'}$
C_s	Smagorinsky constant
D	skin-friction drag
$\mathbf{D}_1$, $\mathbf{D}_2$	Chebyshev first and second order differential matrices
F_n	body force
G	filter function
$\mathbf{I}$	unit matrix
I	amplitude of wall-normal forcing
i	imaginary unit
k	wavenumber of traveling wave

L_x, L_y, L_z size of computational domain in *x*, *y*, and *z* directions

N_x, N_y, N_z number of grid points in *x*, *y*, and *z*, directions

ν_t eddy viscosity

p pressure

ϕ phase difference between u' and v' in Chap. 2

Q second invariant of strain rate tensor

R drag reduction rate

Re Reynolds number

$\mathrm{Re_b}$ Reynolds number based on bulk velocity

$\mathrm{Re_c}$ Reynolds number based on centerline velocity

Re_τ friction Reynolds number

S net saving rate

S_{ij} strain rate tensor

t time

U base flow

u_b bulk mean velocity

U_c centerline velocity

$\overline{u_i u_j}$ Reynolds stress

u_τ friction velocity

u, v, w Streamwise, wall-normal and spanwise velocities

v_w wall-normal velocity on wall

W_p, W_a Pumping and actuation powers

x, y, z Cartesian Coordinates in streamwise, wall-normal, and spanwise directions

Greek Symbols

α near-wall phase shift

δ channel half-width

Δ grid width in Chap. 4

$\delta_{b/s}$ influence layer thickness

ΔD drag increment from D_{lam}

Δ^+ penetration length in wall units

δ_s Stokes layer thickness

ν kinematic viscosity

Φ base phase difference

Superscripts

$(\cdot)^*$ fixed coordinates in Chap. 2

$\hat{(\cdot)}$ Fourier coefficient

$(\cdot)^+$ wall unit

$(\cdot)'$ disturbance component of velocity and pressure in Chap. 2

$(\cdot)'$ sub-grid scale component in Chap. 4

$(\cdot)''$ random component in Chap. 3

Subscripts

$\langle\cdot\rangle_a$ ensemble averaging

$(\cdot)_{lam}$ laminar value

$(\cdot)_0$ uncontrolled value

Other Symbols

$\overline{(\cdot)}$ grid-scale component in Chap. 4

$\bar{(\cdot)}$ mean component in Chap. 3

$\widetilde{(\cdot)}$ periodic component

Acronyms

CSM Constant Smagorinsky Model

CSSM Coherent Structure Smagorinsky Model

DNS Direct Numerical Simulation

DSM Dynamic Smagorinsky Model

DTW Downstream Traveling Wave

FDM Finite Difference Method

GS Grid Scale

LES Large Eddy Simulation

LHS Left-Hand-Side

QSV Quasi Streamwise Vortex

RANS Reynolds Averaged Navier-Stokes equation

RHS Right-Hand-Side

RNS Reynolds Normal Stress

RS Reynolds Stress

RSS Reynolds Shear Stress

SGS Sub-Grid Scale

TKE Turbulent Kinetic Energy

Chapter 1

Introduction

1.1 Background

Motion of turbulent flow has been on of the central issues in science and engineering for about 500 years. Since its inherent properties (i.e., unsteady, non-linearity, and three dimensional motion) induce strong diffusion, strong mixing, chaotic behavior, etc. , it is difficult to understand, predict, and control turbulent flows (Kasagi, 2009), although these have been remarkably challenging issues in the meantime. These difficulties need to be overcome not only in a scientific fields, but also in industrial fields.

When the fluid motion interacts with a rigid body or its surface, drag force is induced to prevent the flow. Drag force usually consists of contributions from pressure and skin-friction, referred to as pressure drag and skin-friction drag, respectively. Generally speaking, control of flow is required to decrease such drags. For pressure drag, a streamline shape obtained by optimization techniques is well known. Tripping wires or dimples of a golf ball are also able to decrease pressure, through delaying flow separation by inducing turbulent flow.

On the other hand, control to reduce skin-friction drag is also an interesting issue. Gad-el-Hak (1994) indicates the importance of skin-friction drag reduction which contributes energy utilization: the friction drag is e.g., about 50, 90, and 100 % of the total drag in commercial aircrafts, underwater vehicles, and pipelines, respectively. Skin-friction drag is known to significantly increase under the turbulent flow due to a so-called coherent structure. Because the coherent structure is inherent motion of wall-turbulence, a skin-friction drag reduction control should be designed to modify it.

1.2 Numerical simulation of channel flow

In our real world, problems originated from flow motion are quite complex. A basic research for turbulent flow, however, considers canonical geometries in order to simplify the problems. For an incompressible fully developed channel flow, which is one of the canonical flows considered in this thesis, theoretical framework is relatively well established because of the following merits:

- Homogeneous in streamwise and spanwise directions: periodic boundary conditions can be employed in those directions;
- Flow has already been fully developed;
- Wall turbulence appears;
- No pressure drag (if there is no obstacle);
- Internal flow;
- Cartesian coordinates can be used.

The abovementioned advantages allow us to clarify the control effect and the mechanism without being bothered by other effects like a spatial development a boundary layer flow, for example.

Owing to development of the digital computers, direct numerical simulation (DNS) and large eddy simulation (LES) have become handy tools to investigate fundamental turbulent flow behavior. Especially, contribution from DNS is significant since it can provide accurate data without introducing any turbulence models. The first DNS was made by Orszag and Patterson (1972) for a homogeneous isotropic turbulence. The pioneering DNS for a incompressible turbulent channel flow presented by Kim et al. (1987) at $\mathrm{Re}_\tau \approx 180$, where Re_τ is the friction Reynolds number defined as $\mathrm{Re}_\tau = \frac{u_\tau^* \delta^*}{\nu^*}$. u_τ^*, δ^*, and ν^* are the friction velocity, the channel half-width, and the kinematic viscosity, respectively. While this low Reynolds number indicates an initial stage of transition from a laminar to a turbulent flow, the resultant turbulent statistics were in good agreement with experimental data. Mansour et al. (1988) used Kim *et al.*'s data in order to analyze the transport equations of Reynolds stress (RS) and turbulent kinetic energy (TKE) (hereafter referred to as the RS budget and the TKE budget,

respectively). The RS and TKE are fundamental indicators of turbulence. Therefore, this analysis is also useful to quantify of the dynamics of turbulent flow. It used be and still is the central issue of turbulence modeling (Cambon and Scott, 1999; Launder et al., 1975); it is also a fundamental tool to clarify the cause of turbulence modification by active control (Fukagata and Kasagi, 2003; Kasagi et al., 2009b).

While early DNS employed a spectral method, which had been the sole method to stably and accurately simulate turbulent flows without introducing upwinding (which introduces numerical diffusion), flow geometry is limited to some canonical flows. Thus, a stable and non-diffusive (i.e., energy-conservative) finite difference method (FDM) had been explored for a long time. Although the energy-conservative second-order FDM on a uniform grid had been proposed as early as 1960's (Harlow and Welch, 1965; Piacsek and Williams, 1970), we had to wait for 30 years for such FDM to be extended to more practical numerical configurations (such as higher order FDMs, nonuniform grid, etc.). Morinishi et al. (1998) presented a class of energy-conservative FDMs on uniform Cartesian grids including generalization to higher order FDMs. Kajishima (1999a) (also Bewley (1999); Ham et al. (2002)) extended its second-order version to a nonuniform Cartesian grid. To date, energy-conservative FDM has been extended to, e.g., the cylindrical coordinates (Fukagata and Kasagi, 2002; Morinishi et al., 2004), arbitrary orthogonal curvilinear coordinates (Nikitin, 2006) and the low Mach number approximation (Desjardins et al., 2008).

Analysis of the transport equations for the Reynolds stress and the turbulent kinetic energy is useful for the quantification of different dynamical contributions in turbulence (Mansour et al., 1988). For FDM on the staggered grid, however, it is not straightforward to compute each term in RS and TKE budgets. The quantities composing each term are defined at different locations; thus, interpolation is required. In order to perform a reliable analysis, such interpolation should be consistent with the discretized Navier-Stokes equation.

A consistent scheme for computation of RS and TKE budgets in Cartesian coordinates was proposed by Suzuki and Kawamura (1994) and Kawamura (1995). They considered the second-order central FDM on a uniform staggered grid and presented a relevant interpolation scheme for the computation of each term in RS and TKE budgets. Although their scheme had much higher consistency than intuitive interpolation schemes, some issues were left: 1) the turbulent diffusion term was left inconsistent;

2) strictly speaking, their scheme is consistent only on a uniform grid. This is natural because, as introduced above, the general framework of energy-conservative FDM had not been developed by the time Suzuki and Kawamura (1994) proposed this scheme. By now, the energy-conservative FDM has become mature: it is now possible to construct a consistent scheme resolving the abovementioned issues.

1.3 Structure of wall turbulence

Owing to integration of DNS databases and a development of visualization methods, spatial structures of wall turbulence have been revealed. Streaky structures with alternating high- and low-speed flows expand in the streamwise direction. Smith and Metzler (1983) found that the streamwise length of the low-speed streak is about 1000 wall-units and the spanwise spacing between them is about 100 wall-units. Here, the wall-units is defined as

$$x^+ = \frac{u_\tau^* x^*}{\nu^*}, \tag{1.1}$$

$$u^+ = \frac{u^*}{u_\tau^*}. \tag{1.2}$$

Jimenez and Moin (1991) presented a minimum channel unit: the domain size wider than 100 wall units in a spanwise direction sustains turbulence whereas the narrower box cannot sustain it. Hamilton et al. (1994) proposed a regeneration cycle among streaky structures, streamwise-dependent disturbances, and streamwise vortices, in the minimum channel flow. Due to the development of high performance computers, higher Reynolds number turbulent flows are investigated by means of the DNS (reviewed in Smits et al. (2011)): Moser et al. (1999), $\mathrm{Re}_\tau \approx 590$; Abe et al. (2004), $\mathrm{Re}_\tau \approx 1020$; Iwamoto et al. (2004), $\mathrm{Re}_\tau \approx 1160$; Hoyas and Jimenez (2006), $\mathrm{Re}_\tau \approx 2000$; Iwamoto et al. (2005), $\mathrm{Re}_\tau \approx 2320$. A large-scale structure is also clearly observed in such high Reynolds number flows.

The DNS reveals a vortical structure of a flow by using isosurface of the second invariant of velocity deformation tensor, i.e., so-called Q value. Figure 1.1 visualizes in the lower half of the fully developed channel flow, where the mean flow is directed from left to right. A lot of vortices are found in the region near the wall, which are

the so-called quasi streamwise vortices (QSV). The diameter of QSV is $25-30$ wall-units and the streamwise length is $150-300$ wall-units (Kasagi et al., 1995). This QSV exists in the buffer layer, where the peak of TKE production appears (Robinson, 1991).

A QSV is known to increase skin-friction drag dramatically. Figure 1.2 explains the mechanism, where u' and v' denote the fluctuations of the streamwise and wall-normal velocities, respectively. Due to a no-slip condition for the velocity on the wall, a fluid in the far-wall region has a higher momentum than that in the near-wall region. In a turbulent flow, the QSV exists in the region near the wall. Therefore, the downward rush ($v' < 0$) induced by the rotation of the QSV brings the high momentum fluid from the far-wall region to the near-wall region, whereas the upward rash ($v' > 0$) brings the low momentum fluid from the near-wall region into the far-wall region. Namely, the skin-friction drag is sustained at a higher level than that in the laminar flow. Qualitatively, the strength of momentum exchange is evaluated by the Reynolds shear stress ($-\overline{u'v'}$: referred to as RSS), which is a shear component of the Reynolds stress. In fact, Fukagata et al. (2002) derived an identity equation between the RSS and the skin-friction drag, as explained in the next section.

1.4 Identity equation for skin-friction drag

Related to the dynamics of QSV, there is a mathematical relationship between the skin-friction drag and the RSS. Fukagata et al. (2002) (see also Bewley and Aamo, 2004) derived an identity equation between the skin-friction coefficient and the RSS from the Reynolds averaged Navier-Stokes equation (RANS). The skin-friction drag coefficient in a fully developed channel flow under a constant flow rate can be decomposed into the laminar and the turbulent contributions:

$$C_f = \frac{12}{\mathrm{Re_b}} + 12\int_0^2 2\,(1-y)\left(-\overline{u'v'}\right)dy, \tag{1.3}$$

where $\mathrm{Re_b}$ is the Reynolds number defined as

$$\mathrm{Re_b} = \frac{2\mathrm{u_b^*}\delta^*}{\nu^*}. \tag{1.4}$$

Here, u_b^* is a bulk mean velocity. The contribution from the turbulent behavior is the second term of RHS of this equation, which is described as the y-weighted integration

of the RSS. This indicates that the contribution of the near-wall RSS to the skin-friction drag is more significant than that of far-wall RSS. Namely, it is implied that an effective control for the skin-friction drag reduction should be designed to modify the near-wall turbulence. Moreover, this equation implies that the skin-friction drag can be sustained below the laminar level if a negative RSS is created in the region near the wall. Using an idealized body force (Fukagata et al., 2005b) or traveling wave-like blowing/suction (Min et al., 2006), a skin-friction drag below the laminar level is confirmed (discuss later).

In addition, a general form of the identity equation (1.3) in an internal flow is proposed by Sbragaglia and Sugiyama (2007), i.e., the weighted function, $(1-y)$ in Eq. (1.3), corresponds to the velocity gradient of the creeping flow. This identity equation is extend to a boundary layer flow (Fukagata et al., 2002; Iwamoto et al., 2009), and to a compressible flow (Gomez et al., 2009). According to the same derivation process, a turbulent heat transfer can be described by a integration of a turbulent heat flux, $-\overline{v'T'}$ (Fukagata et al., 2005a; Higashi et al., in press; Kasagi et al., 2012).

1.5 Control for skin-friction drag reduction

A turbulent flow control for a reduction of a skin-friction drag has been extensively studied as reviewed in Moin and Bewley (1994),Gad-el-Hak (1996), and Kasagi et al. (2009b).

Figure 1.5 shows a classification of flow control strategies according to Gad-el-Hak (1994). In the following, we overview this classification for a skin-friction drag reduction control in wall turbulence. The first classification is whether the control requires an external energy input for actuation or not: passive controls and active controls. Changing boundary condition is a passive control e.g., riblets (Choi et al., 1993; Walsh, 1983), which are the surface-mounted longitudinal grooves, compliant surfaces (e.g., Endo and Himeno, 2002; Fukagata et al., 2008; Xu et al., 2003), a structured roughness (e.g., Sirovich and Karlsson, 1997), and a superhydrophobic surface (Martell et al., 2009, 2010; Rothstein, 2009). Using additives can also be considered as a passive control[1] e.g., an adding polymer (White and Mungal, 2008), surfactants (Li et al., 2008) and micro bubbles (Oishi et al., 2009). While an advantage of these is that they does not to require the energy for actuation, the disadvantages are that the additives

have an impact to environment and the riblets can decrease the skin-friction drag only few percents.

An active control, however, can reduce a skin-friction drag larger than that by a passive control. It can be substituted into an interactive control and a predetermined control according to whether it requires a sensors or not. A predetermined control, mainly focused in this thesis, is e.g., a traveling wave-like blowing/suction (Min et al., 2006, discussed later), a spatial and temporal wall oscillation (Quadrio et al., 2007), using a buoyancy force (Yoon et al., 2006). The major drawback of this predetermined control is that it requires much energy for actuation than the other control strategies.

An interactive control, which requires any sensors, is subdivided into a feedforward and a feedback strategies. The most famous feedback control is the so-called opposition control presented by Choi et al. (1994): a transpiration is added from a wall to cancel a QSV based on information detected at a sensing plane. The performance of this control is further investigated numerically (Chang et al., 2002; Chung and Talha, 2011; Fukagata and Kasagi, 2003; Hammond et al., 1998; Iwamoto et al., 2002; Le Dauphin and Fukagata, 2011) and experimentally (Rebbeck and Choi, 2006). This control strategy is extend for using wall deformation (Endo et al., 2000; Kang and Choi, 2000). The opposition control strategy, however, is difficult to use in practice because a sensor should be as small as the QSV and put into a flow. Furthermore, the opposition control strategy is extended by using the modern control theory (Abergel and Temam, 1990) as reviewed in Kim (2011), i.e., an adaptive control, using a neural network (Lee et al. (1997)), and an optimal (Bewley et al. (2001)) and a suboptimal controls (Fukagata and Kasagi, 2004; Lee et al., 1998; Takada, 2010). As an experimental study, Yoshino et al. (2008) proposed an experimental feedback control system, which induces wall-deformation to decrease the QSV.

1.5.1 Control effect at high Reynolds number flow

Control effect at a high Reynolds number flow is also an interesting issue. While DNS of a high Reynolds number turbulent channel flow has been investigated, a high performance computer resource is required to resolve turbulent behavior. Thus, LES

[1]This is sometimes classified as an active predetermined control because it requires energy to supply additives.

has been a handy tool to simulate such a higher Reynolds number flow. Smagorinsky (1963) pioneered LES, which used an eddy viscosity model (called as Constant Smagorinsky model: CSM). This model is extended to a dynamical model proposed by Germano et al. (1991) and Lilly (1992) (called as Dynamic Smagorinsky model: DSM).

As an attempt to investigate an ordinary control effect at a high Reynolds number flow, Collis et al. (2000) studied the Reynolds number dependency of the feedback control, namely opposition and optimal controls, by DSM-LES at $100 < \mathrm{Re}_\tau < 590$. Wider range of the Reynolds number, $80 < \mathrm{Re}_\tau < 720$, for the opposition control is studied by Chang et al. (2002). Iwamoto et al. (2002) reveals the control effect by the opposition control at $\mathrm{Re}_\tau = 110 - 650$ by means of the DNS. These results reported that the effectiveness of this feedback control decreases with increasing the Reynolds number.

While DSM is attractive because it is possible to capture the laminar flow behavior contained in a turbulent flow and a special treatment for the near-wall behavior, i.e., dumping function, is not required. The computational cost, however, increases due to the use of a test filtering procedure in order to determine the Smagorinsky constant. Recently, Kobayashi (2005) presented a new model for LES based on the coherent structure (i.e., the coherent structure Smagorinsky model, referred as CSSM). This model has been validated in canonical flow geometries. Because this model determines the Smagorinsky constant instantaneously and locally, it is expected to be suitable for computation of a controlled flow at a high Reynolds number.

1.6 Traveling wave-like blowing/suction control

Min et al. (2006) proposed a novel predetermined control in an incompressible fully developed channel flow: a traveling wave-like blowing/suction control. The channel flow, driven by the pressure gradient when the flow rate is kept constant, is subject to blowing/suction from wall surface in the form of a traveling wave. The schematic of this control is shown in Fig. 1.5 and the wall-normal velocity on the surface of the wall is given as

$$v_{w\pm} = \mp a\cos\left(k(x-ct)\right), \tag{1.5}$$

where x and t denote the streamwise coordinate and a time, respectively. The parameters, a, k, and c, represent the amplitude, wavenumber, and wavespeed of the traveling wave. The skin-friction drag reduction effect is investigated in a laminar flow by means of a linear analysis: the solution of the linearized Navier-Stokes equation and the identity equation (1.3). They revealed that the upstream traveling wave (viz., the wave travels to the opposite direction to the base flow) can sustain the drag below the laminar level, while the upstream traveling wave increases the skin-friction drag. The resultant drag reduction effect by the downstream traveling wave-like blowing/suction is confirmed in a two dimensional flow geometry. Furthermore, they performed DNS in a three dimensional geometry in order to investigate the control effect in the turbulent channel flow.

While a major drawback of the feedback control lie in difficulty in realizing the sensors which needs to be small and detect high frequency when Reynolds number increases (Kasagi et al., 2009b), a predetermined control does not require such sensors. Thus, Min et al. (2006) gave a great impact for a community of turbulent flow control because this control advantages:

- is a predetermined control,
- has a large drag reduction effect (sublaminar drag),
- obtained positive efficiency,
- is a counter-evidence for Bewley's conjecture (discuss later).

Major contributions inspired by Min et al. (2006) are illustrated in Fig. 1.4.

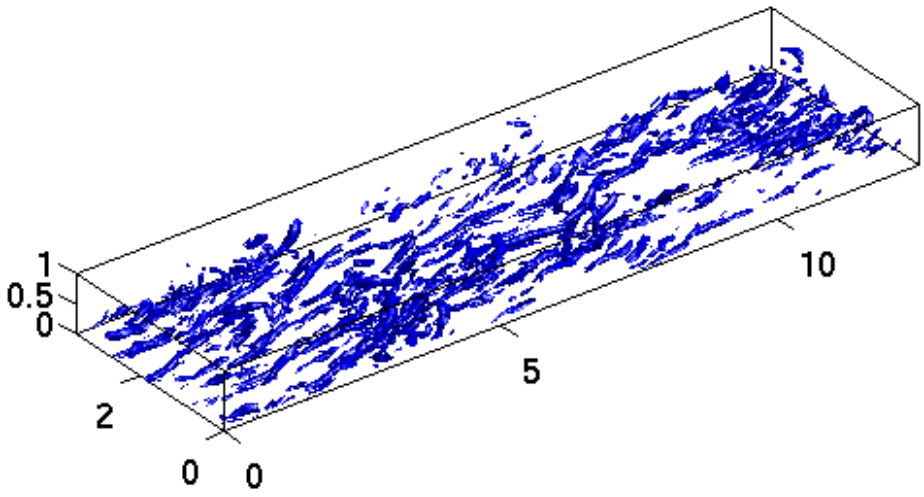

Figure 1.1: Visualization of vortical structure of channel flow at lower-half region without any controls at $\mathrm{Re}_\tau \approx 180$. An isosurface of $Q^+ = -0.03$ is demonstrated.

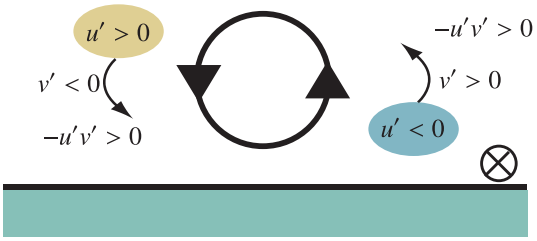

Figure 1.2: Schematic of the mechanism of increasing RSS due to rotation of a QSV in the near-wall region.

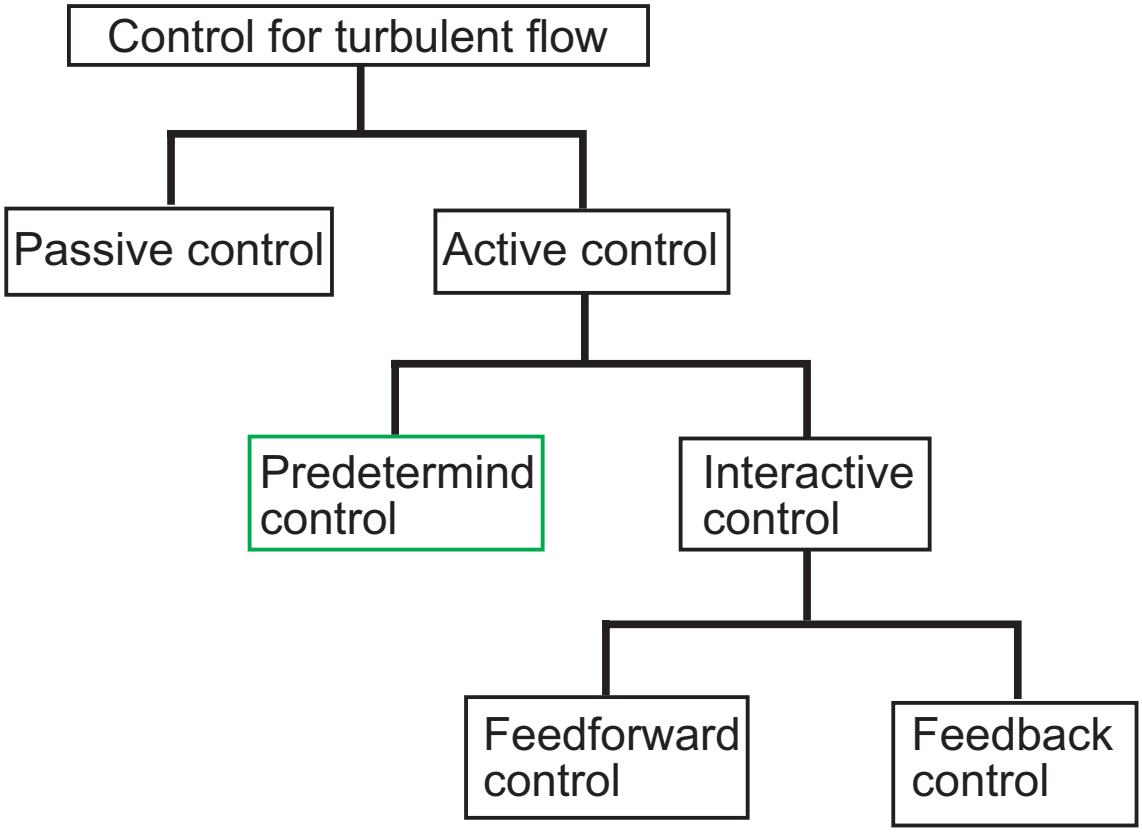

Figure 1.3: Classification of flow control strategies (Gad-el-Hak, 1994).

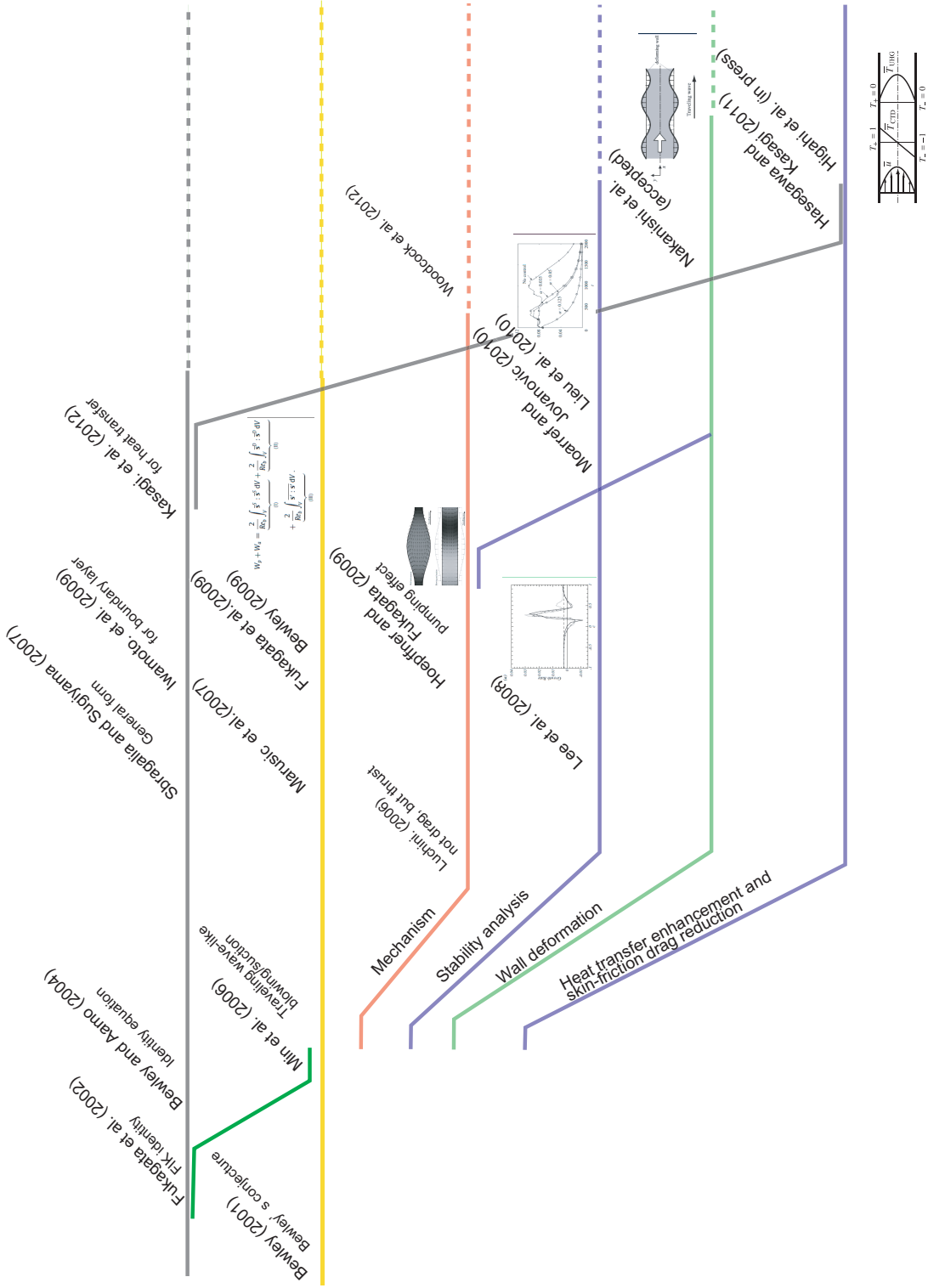

Figure 1.4: The history of the previous studied related to the traveling wave-like control (Min et al., 2006).

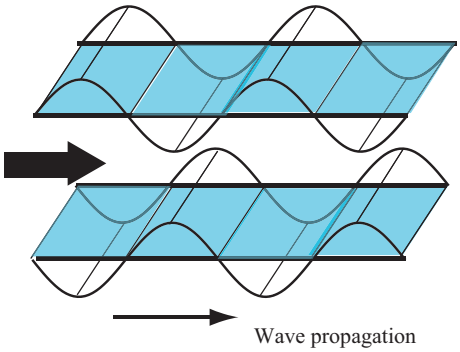

Figure 1.5: The traveling wave-like blowing/suction control.

1.6.1 Conjecture and theorem for limitation

Min et al. (2006) showed that the upstream traveling wave on a turbulent channel flow at $\mathrm{Re}_c = 2000$ (based on the laminar centerline velocity) sustained the skin-friction drag below the laminar level (i.e., sublaminar drag). It is because the negative RSS is generated in the region near the wall, which contributes to decrease the skin-friction drag according to Eq. (1.3). This sublaminar drag had been conjectured to be impossible by Bewley (2001) (referred as Bewley's conjecture, hereafter):

> the lowest sustainable drag of an incompressible constant mass-flux channel flow, in either 2D or 3D, when controlled via a distribution of zero-net mass-flux blowing/suction over the channel walls, is exactly that of the laminar flow.

The first contribution of Min *et al.*'s work produced an evidence against this conjecture. Not only the drag reduction effect, but also the obtained efficiency is positive. Another counter-evidence is given by Fukagata et al. (2005b), who assumed a feedback body force so as to make a negative RSS.

Fukagata et al. (2009) (see also Bewley, 2009) gave a mathematical theorem for the limitation of the power balance instead of the skin-friction drag in the fully developed duct flow:

> the lowest net power required to drive an incompressible constant mass-flux flow in a periodic duct having arbitrary constant-shape cross-section,

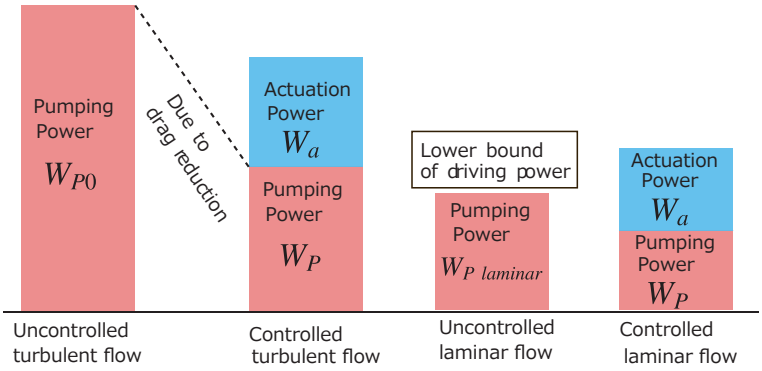

Figure 1.6: The power balance and its limitation for the channel flow.

when controlled via a distribution of zero-net mass-flux blowing/suction over the no-slip channel walls or via any body forces, is exactly that of the Stokes flow.

Figure 1.6 shows the schematic of the limitation of the power balance in a fully developed channel flow under constant flow rate according to this theorem. We denote the pumping energy under uncontrolled turbulent channel flow as W_{p0}. Due to the drag reduction control, the pumping power, W_p, decreases while the actuation power input appears as W_a. If the efficiency is positive, $W_p + W_a < W_{p0}$. However, the abovementioned theorem tells that the limitation of the total energy input equals to the pumping power for driving the laminar flow under the same flow rate. Therefore, it is impossible that the total power input achieves below $W_{p,laminar}$. Furthermore, it is worth nothing to control the laminar flow to reduce the skin-friction drag because the total power input cannot be below the uncontrolled level (i.e., $W_{p,laminar}$) even if the drag reduction can be obtained.

1.6.2 Mechanism of drag reduction

The mechanism of the drag reduction by the traveling wave-like blowing/suction control is an interesting issue. Min et al. (2006), themselves, discussed the mechanism in a two-dimensional simulation of a channel flow under zero mean pressure gradient. It was found that the net mass flux in the streamwise direction was induced by the upstream traveling wave, which is, as pointed out by Marusic et al. (2007), equivalent to

the skin-friction drag reduction in the channel flow under a constant mass flow rate. This net mass flux was reported to be induced by the RSS caused by the positive phase shift of streamwise velocity disturbance: the phase of streamwise velocity disturbance induced by the traveling wave is found to shift from that by the standing wave, while the phase of wall-normal velocity disturbance remains unchanged.

Luchini (2008) found that a drag reduction can be induced by an upstream traveling wave because an actuation pumps a mean flow to a downstream direction. He concluded "*not drag, but thrust*" and pointed out a relation with a well-known streaming phenomena (Lighthill, 1978; Riley, 2001). This thrust appeared as "a pumping effect" in a two dimensional channel flow without imposing a mean pressure gradient presented by Hoepffner and Fukagata (2009), who revealed that a traveling wave-like blowing/suction pumps in a backward direction, while the similar deformation (i.e., peristalsis) pumps in a forward direction. Very recently, Woodcock et al. (2012) derived an asymptotic behavior of an induced bulk flow by a traveling wave-like blowing/suction.

A mechanism of the skin-friction drag reduction is explored in a two dimensional channel flow by means of linear analysis in Chap. 2 of this thesis. A linear analysis perfectly reproduced Min et al. (2006)'s result and a wider range of parameters for not only a varicose mode but also a sinuous mode is studied: the varicose and sinuous modes mean the wave-like wall transpiration on the bottom and top walls in the opposite and the same sign, respectively. The detailed phase analysis reveals how a negative RSS is generated in the region near the wall in laminar Poiseuille flow, while Min et al. (2006) revealed it in a zero mean pressure gradient channel flow. In order to determine the phase shift of the streamwise velocity disturbance induced by the traveling wave, Min et al. (2006) defined its origin as that induced by the standing wave under zero mean pressure gradient. On the other hand, in this thesis we define the origin as the phase of an inviscid velocity disturbance.

Additionally, Quadrio et al. (2007), although not inspired by Min et al. (2006), showed that a standing wave with a sinuous mode decrease skin-friction drag when the wavelength is shorter than 300 wall units and an amplitude is 0.7 wall units.

1.6.3 Stability of the flow

The major drawback of Min et al. (2006)'s control may be a smaller gain (i.e., more expensive control cost) than that of the existing feedback control schemes (Kasagi et al., 2009a; Luchini, 2008). Under a constant flow rate condition, the gain of upstream traveling wave control is on the order of $1-10$, while that of an existing feedback control schemes is on the order of $100-1000$. According to a recent study, the gain of the upstream traveling wave control can be even smaller under a constant pressure gradient condition instead of constant flow rate. A plausible reason for the small gain is that the upstream traveling wave does not stabilize the flow.

Lee et al. (2008) performed a stability analysis for Min *et al.*'s control: the upstream and downstream traveling waves destabilize and stabilize the flow, while the skin-friction drag decreases and increases, respectively. However, the downstream traveling wave, when the wave speed is 40 % of the bulk velocity, induces the flow unstable dramatically, which is due to a critical layer effect as pointed out by Hoepffner and Fukagata (2009).

The traveling wave-like blowing/suction control is used to prevent to an onset of a turbulent flow from a laminar flow, as demonstrated by DNS of Moarref and Jovanovic (2010) and the receptivity analysis of Lieu et al. (2010). They revealed that the positive net gain was obtained when the wave travels to the downstream direction. Furthermore, this wave could relaminarize the turbulent flow in a fixed pressure gradient channel flow.

1.6.4 Related studies

A traveling wave-like control is investigated from some different points of view. Due to a similarity between the transport equations of velocity and temperature i.e., a so-called "Reynolds analogy" (White, 2006), it is known to be difficult to achieve a skin-friction drag reduction and a heat transfer enhancement simultaneously. Hasegawa and Kasagi (2011) derived a suboptimal control law designed to achieve drag reduction and heat transfer enhancement simultaneously under a constant flow rate and an uniform heat generation, which achieved heat enhancement with suppression of skin-friction drag increase. Moreover, the resultant control input of the suboptimal control law was found to be similar to a downstream traveling wave-like blowing/suction. Higashi et al.

(in press) performed a linear analysis and DNS of a channel flow with a predetermined traveling wave-like blowing/suction. They found that the upstream traveling wave-like blowing/suction breaks the similarities under constant temperature difference between walls or uniform heat generation when the flow rate is kept constant.

Instead of using the traveling wave-like blowing/suction, a wall deformation can be expected to induce a similar drag reduction effect. Taneda and Tomonari (1973) pioneered to experimentally investigate effect of the traveling wave-like wall deformation inspired by the swimming motion of fish, and revealed that the motion of the flexible wall decreases the velocity fluctuations. In the last decade, Shen et al. (2003) and Yang and Shen (2009) explored a turbulent channel flow over a smooth wavy wall with transverse motion in the form of a streamwise travelling wave. They considered a channel flow geometry with a lower and an upper walls of wavy form and slip-velocity, respectively. Again, Hoepffner and Fukagata (2009) considered a zero mean pressure gradient channel flow under a wavy surface for upper and lower walls in the varicose mode. As an extension of Hoepffner and Fukagata (2009), Nakanishi et al. (accepted) studied the traveling wave-like wall deformation in a fully developed turbulent channel flow. When the drag is reduced by the downstream traveling wave (which is an opposite direction to that of the blowing/suction case), they confirmed three states: ordinary drag reduction, re-laminarization, and a periodic cycle between high and low drags.

Drag reduction effect of flow over an oscillating wall is well-known (Karniadakis and Choi, 2003). Quadrio et al. (2009) imposed a spanwise wall velocity which travels to a downstream or an upstream direction. Whether the drag increases or decreases depends on the wavespeed, which is confirmed by an experimental investigation presented by Auteri et al. (2010). The oscillation of the spanwise Lorenz force is also known to reduce the skin-friction drag as presented by Du and Karniadakis (2000) and Du et al. (2002).

Effect of Lorenz force is studied by means of a DNS by Berger et al. (2000), who studied both a closed-loop and a open-loop controls. As a possibility for realization of such a body force, use of a plasma actuator (Cattafesta III and Sheplak, 2011; Corke et al., 2009; Fukagata et al., 2010) is proposed. Murai and Fukagata (2011) performed DNS to study the control effect an opposed-plasma actuator which induces blowing from the wall in a fully developed channel flow. They assumed a simple model pre-

sented by Shyy et al. (2002): a plasma exists only a triangle area where the body force is induced, while the real behavior of ionized particle motion is quite complex.

1.7 Motivation and objective

The traveling wave-like blowing/suction control is still attractive for realization of active turbulent drag reduction: large amount of drag reduction (i.e., sublaminar drag), positive efficiency, simple control strategy, etc. Additionally, the control does not require massive micro-sensors (Fukagata, 2011; Kasagi et al., 2009b), which is one of the biggest hurdles for a feedback control to be applied in reality. The main objective of this thesis is to investigate the control effect by the traveling wave-like blowing/suction and to discuss its mechanism. This control is not realized straightforwardly since the existing device hardly induces such a traveling wave. However, consideration of the control effect and the mechanism of the drag reduction is expected to be a first step and to design such a flow control device.

In the following, motivation and targets in each chapter are listed.

- Chap. 2, control of laminar flow
  - Min *et al.*'s linear analysis is extended for a wider range of parameter: wavenumber, wavespeed, and varicose or sinuous modes. An unified scaling will be shown according to Stokes' second problem. Detailed phase analysis is employed to explore the mechanism of generation of a skin-friction drag increment.
- Chap. 3, control of low Reynolds number turbulent flow
  - An interpolation scheme is proposed to use for the computation of the Reynolds stress budget, which holds consistency with the employed second-order energy conservative FDM.
  - Direct numerical simulation is performed to investigate the control effect by a traveling wave-like blowing/suction. It is validated whether the mechanism discussed in Chap. 2 can explain the effect in turbulent channel flow or not. As a comparison, the control effect induced by the traveling wave-like wall-normal forcing, i.e., idealized Lorenz force, is considered.

- Chap. 4, control of higher Reynolds number turbulent flow
  - Large eddy simulation with the Coherent Structure model (Kobayashi, 2005) is performed at $\mathrm{Re}_{\tau 0} \approx 177$, 395, and 595. After validation and verification of an uncontrolled flow, a control effect of the opposition control (Choi et al., 1994) is investigated in order to confirm the usefulness of this model. Finally, the control effect by a traveling wave-like blowing/suction at such Reynolds numbers is demonstrated.
- Chap. 5, the achievement of this thesis is summarized and a direction of future research is indicated.

Chapter 2

Laminar flow

The control effect by the traveling wave-like control in a two-dimensional laminar Poiseuille flow are considered. The investigation is done by solving the linearized Navier-Stokes equation and by using the identity equation (1.3). The phase relationship between the streamwise and the wall-normal velocity disturbances is mainly focused. It has been known that a traveling wave creates a non-quadrature between the velocity disturbances and generates the positive phase shift of the streamwise velocity disturbance in the case of a skin-friction drag reduction. The present analysis further reveals that this non-quadrature consists of an inviscid base phase relationship and a near-wall phase shift induced by the viscosity. The analogy between the present control and Stokes' second problem is also discussed. The thickness of the near-wall region in which the viscous phase shift takes place is found to be scaled similarly to the Stokes' second problem.

2.1 Motivation

Here, we will discuss the mechanism of a drag reduction when the base flow is a laminar-Poiseuille profile by means of a linear analysis and coupling the identity equation (1.3). This analysis for laminar flow is an extension of the studies of Min et al. (2006) and Hoepffner and Fukagata (2009). In order to obtain a unified explanation on the drag reduction effect by the traveling wave-like blowing/suction in a laminar channel flow, wide ranges of control parameters (Reynolds number, wavenumber, and

wavespeed) are examined and analyzed through a detailed phase analysis. As will be shown later, these effects can be scaled similarly to the Stokes' second problem. In order to demonstrate the validity of this scaling in a different control mode, we also consider the sinuous mode in addition to the varicose mode which has been considered by Min et al. (2006) and Hoepffner and Fukagata (2009).

It is also worth noting that drag reduction control of a laminar channel flow does not make sense from the practical viewpoint. Bewley (2009) and Fukagata et al. (2009) mathematically proved that under a constant flow rate the lower bound of driving power (i.e. sum of pumping and actuation powers) is the pumping power of the laminar channel flow. Namely, the total power can never be saved when control is applied to a laminar channel flow even if a sublaminar drag is achieved. Nevertheless, we study the mechanism of Min et al. (2006)'s control using a laminar flow as an important step toward the comprehensive understanding of control effects in turbulent flows. The use of laminar flow may be justified by the following reasons: (1) the primary effect of control, i.e., production of the "negative" Reynolds shear stress (or, in other words, pumping from the walls (Hoepffner and Fukagata (2009))), is considered common to laminar and turbulent flows; and of course, (2) it is simpler than a turbulent flow.

2.2 Numerical procedure

A two-dimensional channel flow is considered. The governing equations are two-dimensional and incompressible continuity and Navier-Stokes equations. Figure 2.1 shows the flow geometry, the coordinate systems, and the control input. All quantities are made dimensionless by using the centerline velocity, U_c, and the channel half-height, δ. The velocity components in the x^* (streamwise) and y^* (wall-normal) directions are denoted as u and v, respectively. The pressure is denoted as p. The asterisk denotes the fixed coordinates in contrast to the moving coordinates introduced later. The base flow, U, is set to be the laminar Poiseuille profile, i.e., $U = 1 - y^{*2}$.

According to these reference variables, the identity equation (1.3) for the skin-friction coefficient relating to the RSS are rewritten as

$$D = \underbrace{2}_{D_{lam}} + \underbrace{\frac{3}{2}\mathrm{Re}\int_{-1}^{1}(-y)\left(-\overline{u'v'}\right)dy}_{\Delta D}, \tag{2.1}$$

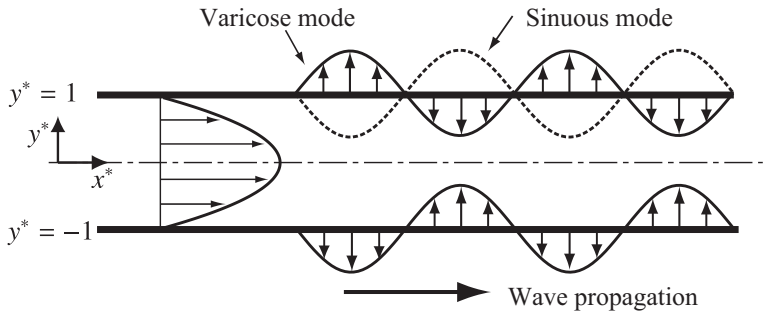

Figure 2.1: Flow geometry and schematic of control input.

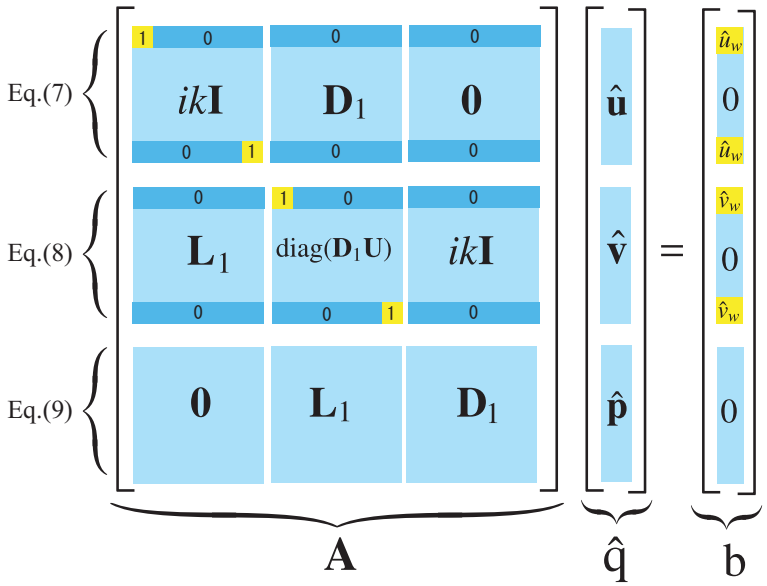

Figure 2.2: Schematic of the system matrix equation with the boundary conditions. The blocks correspond to the discretized version of Eqs. (2.7)-(2.9).

The LHS on this equation, D, means the dimensionless skin-friction drag defined as

$$D = \frac{1}{2}\left(\left.\frac{\partial U}{\partial y}\right|_{y=-1} - \left.\frac{\partial U}{\partial y}\right|_{y=1} \right) \tag{2.2}$$

Here, the Reynolds number is $\mathrm{Re} = U_c \delta / \nu$, On the RHS, the laminar contribution and the drag increment are $D_{lam} = 2$ and ΔD, respectively.

The periodic boundary condition is employed in the streamwise direction. The no-

slip condition is imposed for the streamwise velocity at the wall. As a control input, the wall-normal velocity at the wall is given as a traveling wave-like blowing/suction. Two wave modes are considered for the traveling wave: the varicose mode and the sinuous mode. The varicose mode corresponds to two solid lines in Fig. 2.1, which reads (Min et al., 2006)

$$v_{w\pm} = \mp a\cos\left(k\left(x^* - ct^*\right)\right), \tag{2.3}$$

where v_{w+} and v_{w-} are the wall-normal velocity at the upper and the lower walls, respectively. Namely, the surface wall-normal velocities are in phase with opposite sign. In contrast, the sinuous mode is the combination of the solid line at the lower wall and the dotted line at the upper wall in Fig. 2.1, which reads

$$v_{w\pm} = \pm a\cos\left(k\left(x^* - ct^*\right)\right). \tag{2.4}$$

The surface wall-normal velocities are in phase.

The problem can be reduced into a steady problem by introducing a coordinate transformation from the fixed coordinates to the coordinates traveling with the wave, i.e., $x := x^* - ct^*, y := y^*, t := t^*$ (Javanovic et al., 2006). The boundary conditions (Eqs. (2.3) and (2.4)) in the moving coordinates read

$$v_{w\pm} = \begin{cases} \mp a\cos(kx) & \text{Varicose mode,} \\ \pm a\cos(kx) & \text{Sinuous mode.} \end{cases} \tag{2.5}$$

The unsteady term of incompressible Navier-Stokes equation is transformed as

$$\frac{\partial}{\partial t^*} = \frac{\partial}{\partial t} - c\frac{\partial}{\partial x}. \tag{2.6}$$

Because the flow is steady due to the steady boundary condition, the first term in the right hand side of Eq. (2.6) vanishes.

The governing equations are linearized: $u = U + u'$, $v = v'$ and $p = P + p'$ are substituted into the governing equations and the high order terms of disturbance are neglected. Here, U and P denote the velocity and pressure of the base flow, respectively, and the prime denotes the disturbance component. The linearized disturbance

equations read

$$\frac{\partial u'}{\partial x}+\frac{\partial v'}{\partial y} = 0, \tag{2.7}$$

$$-c\frac{\partial u'}{\partial x}+U\frac{\partial u'}{\partial x}+v'\frac{\partial U}{\partial y} = -\frac{\partial p'}{\partial x}+\frac{1}{\mathrm{Re}}\nabla^2 u', \tag{2.8}$$

$$-c\frac{\partial v'}{\partial x}+U\frac{\partial v'}{\partial x} = -\frac{\partial p'}{\partial y}+\frac{1}{\mathrm{Re}}\nabla^2 v'. \tag{2.9}$$

Equation (2.7)-(2.9) are discretized by using the Fourier transformation in the streamwise direction and the Chebyshev collocation method in the wall-normal direction. These equations can be expressed as a system matrix equation; thus, the solution can easily be obtained.

Due to the periodic boundary condition assumed in the streamwise direction, the Fourier transformation can be applied for the state variable vector, $\mathbf{q}' = (\mathbf{u}', \mathbf{v}', \mathbf{p}')^T$, as

$$\mathbf{q}' = \mathrm{Real}\left(\hat{\mathbf{q}}(y)\exp(ikx)\right). \tag{2.10}$$

In the wall-normal direction, the Fourier coefficients are discretized by using the Chebyshev collocation point method: the Chebyshev differentiation matrix of a MATLAB function, chebdif.m provided by Weidman and Reddy (2000), is applied for the y-derivative operators to obtain the discretized state vector,

$$\hat{\mathbf{q}} = (\hat{\mathbf{u}}, \hat{\mathbf{v}}, \hat{\mathbf{p}})^T. \tag{2.11}$$

As a result of these transformations, Eqs. (2.7)-(2.9) are expressed as a system matrix equation,

$$\mathbf{A}\hat{\mathbf{q}} = \mathbf{b}, \tag{2.12}$$

of which concrete form is graphically shown in Fig. 2.2, where the operator $\mathbf{L}_1$ reads

$$\mathbf{L}_1 = ik(\mathbf{U}-c\mathbf{I}) - \frac{1}{\mathrm{Re}}(\mathbf{D}_2 - k^2\mathbf{I}), \tag{2.13}$$

and $\mathbf{D}_1$ and $\mathbf{D}_2$ are the Chebyshev first and second order differentiation matrices, respectively, and $\mathbf{I}$ is the unit matrix. The boundary conditions read

$$\hat{v}_{w\pm} = \begin{cases} \mp a & \text{Varicose mode,} \\ \pm a & \text{Sinuous mode.} \end{cases} \tag{2.14}$$

The boundary conditions are included in the system matrix, **A**, and the right hand side, **b**, as shown in Fig. 2.2. Thus, the solution of the matrix equation can be simply obtained by

$$\hat{\mathbf{q}} = \mathbf{A}^{-1}\mathbf{b}, \tag{2.15}$$

and spatial distributions of u', v', and p' are computed by the inversed Fourier transform to the solution. Finally, ΔD is computed by using Eq. (2.1).

According to the amplitude expansion of flow quantities, the drag effect appears as the second order solution that can equivalently be expressed as the product of two first order solution, u' and v' (see, e.g., Eq. (A2) of Hoepffner and Fukagata (2009)). Therefore, when the flow response is well described by the linear solution, we can predict the drag by substituting the first order solution in to Eq. (2.1). Namely, we can predict the drag increment, ΔD, (which is essentially the nonlinear effect) from the linear solution. The results obtained by these calculations are linear solutions so that the disturbance components are scaled by the wave amplitude, a.

While the Orr-Sommerfeld (OS) operator formulation used by Min et al. (2006) is usually preferred to study this kind of problem (Drazin and Reid (1981) and Schmid and Hennningson (2000)), here we use the alternative formulation based on the primitive variables. Although these two formulations are mathematically equivalent, the present formulation has an advantage that it can be easily extended to include control inputs other than blowing and suction, e.g., body forces due to local heating and cooling (Yoon et al. (2006) and Mamori et al. (2009)), MHD (Du and Karniadakis (2000)), or plasma actuators (e.g., Shyy et al. (2002)), which may be more realistic control input than blowing/suction. All we have to do is to add the terms of these effects, we do not need to play with algebra beforehand. The result obtained with the same number of nodes should be more accurate than that with the OS formulation because the OS has a fourth order derivative whereas the derivative in the presented formulation is at highest second order. Increase of computational cost is subtle with the current computer power.

Figure 2.3 shows the dependency of the computed amount of drag reduction on the number of Chebyshev nodes. The difference between the values obtained with 128 nodes (used throughout the present study) and 512 nodes was less than 10^{-12} for both cases presented in Fig. 2.3.

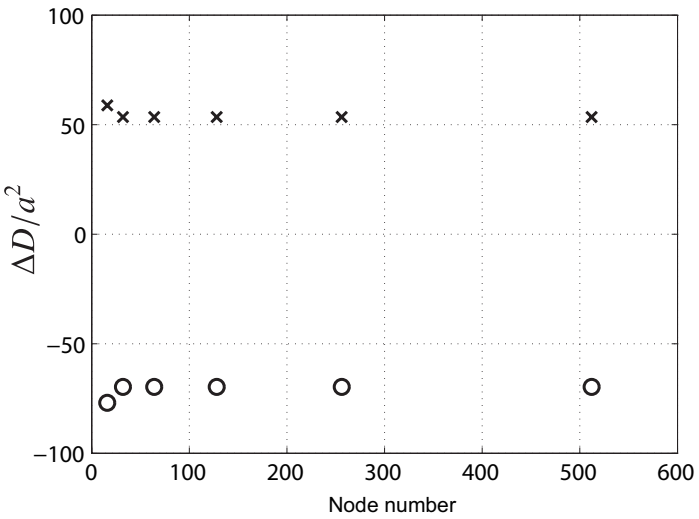

Figure 2.3: Node number dependency of $\Delta D/a^2$ for $k = 0.5$, $c = -2$, and Re $= 2000$: circle, varicose mode; cross, sinuous mode.

2.3 Result and discussion

2.3.1 Varicose mode

Figure 2.4 shows the drag increment, ΔD, as a function of the wavespeed of the traveling wave, c, computed at Re $= 2000$ under different wavenumbers, $k = 0.5$, 1.0, 1.5, and 2.0. It confirms that the present method perfectly reproduces the results of Min et al. (2006). For the upstream traveling wave as shown in Fig. 2.4(a), the drag decreases ($\Delta D < 0$) by the faster traveling wave (i.e., the case of larger $|c|$). The amount of drag reduction is larger for smaller wavenumbers. For the downstream traveling wave as shown in Fig. 2.4(b), ΔD is found to be positive. The drag is nearly unchanged in the range of $c > 1$, whereas ΔD becomes extremely large in the range of $0 < c < 1$.

Figure 2.5 shows ΔD as a function of c for $k = 0.5$ under different Reynolds numbers, Re $= 20$, 200, 2000, and 10000. At all Reynolds numbers, the drag is decreased by the faster upstream traveling wave. As increasing the Reynolds number, the effect of control becomes larger.

Two explanations can be made for the extremely large value of ΔD observed around $c = 0.4$. One is the existence of a critical layer Hoepffner and Fukagata (2009), which

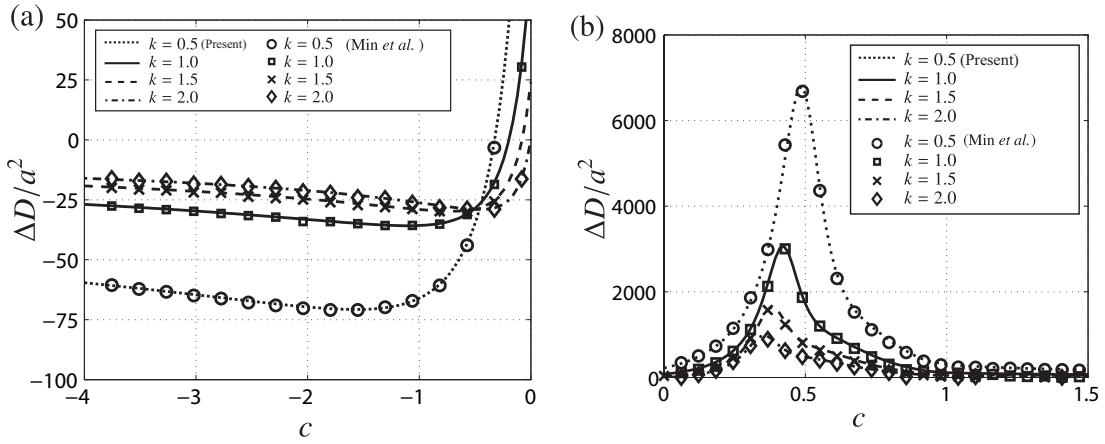

Figure 2.4: Normalized drag increment, $\Delta D/a^2$, as a function of the wavespeed, c, under different k (Re $= 2000$, varicose mode): (a) upstream traveling waves, $c < 0$; (b) downstream traveling waves, $c > 0$.

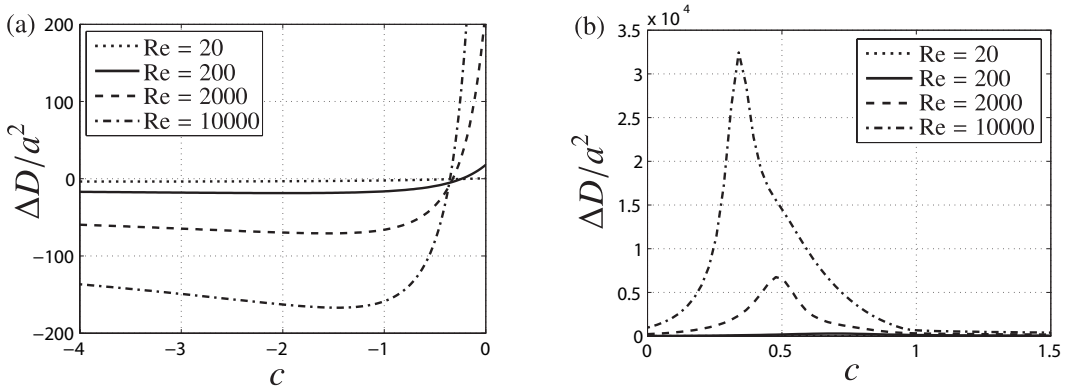

Figure 2.5: Normalized drag increment, $\Delta D/a^2$, as a function of c at different Re ($k = 0.5$, varicose mode): (a) upstream traveling waves $c < 0$; (b) downstream traveling waves, $c > 0$.

moves at the same speed of the wavespeed of traveling wave as illustrated in Fig. 2.6. This layer is a singular point in the inviscid limit and the singular-like behavior still remains also in the viscous flow; thus, the velocity fluctuations, u' and v', are strongly amplified. Another is the quasi-resonance between the forcing at the wall and the least stable mode of the governing equations. As has been shown by Lee et al. (2008), the growth rate of the least stable mode takes the maximum around $c = 0.4$.

Figure 2.7(a) shows the RSS distributions for $c = -1.5$ and Re $= 2000$, under dif-

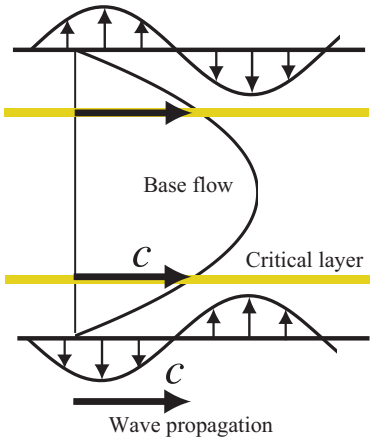

Figure 2.6: Schematic of a critical layer.

ferent wavenumbers, $k = 0.5$, 1.0, 1.5, and 2.0. It is clearly observed that the negative and positive RSSs are produced in the region near the lower and upper walls, respectively. According to Eq. (2.1), the skin-friction drag is the y-weighted integration of the RSS: the drag reduction, $\Delta D < 0$, observed above is due to the negative RSS induced in the region near the walls. Moreover, the zoom-up of the near wall region in Fig. 2.7(a) shows that the peak of the RSS decreases as increasing the wavenumber. In this figure, we define an influence layer thickness of the traveling wave-like blowing/suction, $\delta_{b/s}$, which is the height from the lower wall to the point of maximum $|-\overline{u'v'}|$. This influence layer thickness, $\delta_{b/s}$, is also found to decrease as increasing the wavenumber.

Figure 2.7(b) shows the RSS distributions for $c = -1.5$ and $k = 0.5$ under different Reynolds numbers, Re $= 20$, 200, 2000, and 10000. As increasing the Reynolds number, increase of maximum RSS and decrease of $\delta_{b/s}$ are observed.

These results imply that there is a relationship among the influence layer thickness, the wavenumber, and the Reynolds numbers. From the similarity of the problems, it may be natural to assume an analogy between the present flow and the Stokes' second problem. The Stokes' second problem is the steady oscillation of the wall under stationary fluid. The Stokes' layer thickness, δ_s, scales as

$$\delta_s \sqrt{\omega \mathrm{Re}} \simeq \text{const.}, \tag{2.16}$$

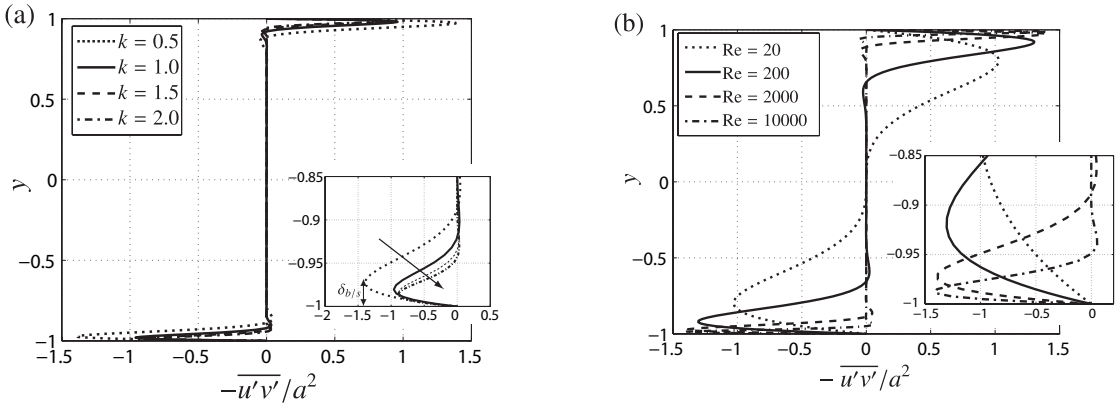

Figure 2.7: Profile of the RSS induced by the varicose mode and the upstream ($c = -1.5$) traveling wave: (a) for different k, (Re $= 2000$); (b) for different Re ($k = 0.5$).

where, ω is the angular frequency of the wall oscillation. We apply Eq. (2.16) to the case of traveling wave-like blowing/suction, i.e., by substituting $\omega = |c|k$,

$$\delta_{b/s}\sqrt{|c|k\mathrm{Re}} \simeq \text{const.}, \tag{2.17}$$

where the left hand side of this equation (2.17) is referred hereafter as the scaled influence layer thickness.

This scaling is similar to that used for the analysis of skin-friction drag reduction induced by spanwise wall oscillations (e.g., Karniadakis and Choi (2003)), although the detailed mechanism is somewhat different: in the spanwise oscillation the existing RSS is suppressed in the Stokes layer through the disruption of near-wall turbulence-production cycle (Choi et al., 2002; Ricco and Quadrio, 2008); while in the present case the RSS is actively produced in this layer.

Figure 2.8(a) shows the scaled influence layer thickness as functions of c for different wavenumbers, k. The scaled influence layer thickness is found to be unchanged in the range of $c < -0.4$ and $c > 1.0$, whereas it deviates from the constant value in the range where the critical layer effect is significant. The sub-figure shows scaled influence layer thickness in wider range of the vertical axis.

Figure 2.8(b) shows the scaled influence layer thickness at different Reynolds numbers. For the cases of Re $= 200$, 2000, and 10000, the scaled influence layer thickness is kept constant except for $|c| < 1$. The value for Re $= 20$ are slightly lower than that for the other cases.

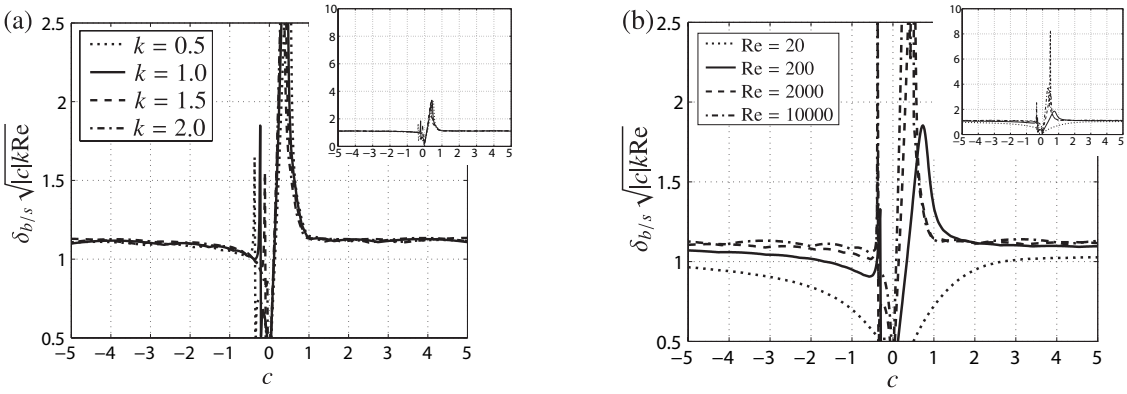

Figure 2.8: The scaled influence layer thickness, $\delta_{b/s}\sqrt{|c|k\mathrm{Re}}$, as a function of c (varicose mode): (a) for different k (Re $= 2000$); (b) for different Re ($k = 0.5$).

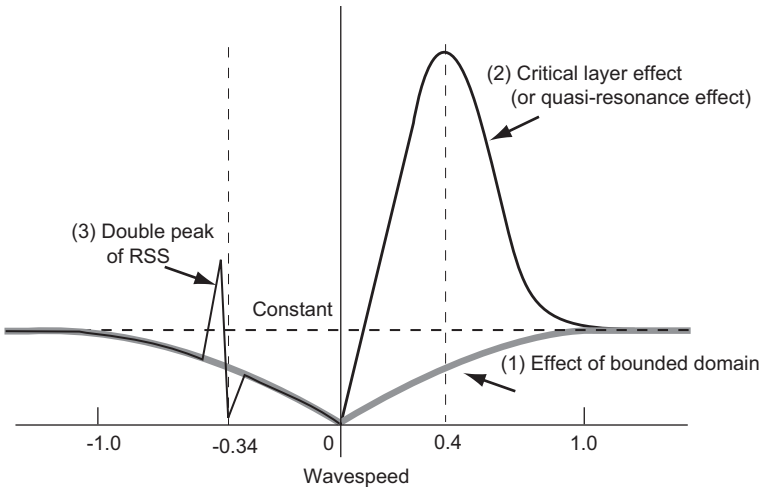

Figure 2.9: Schematic of the scaled influence layer thickness: thick gray line, effect of bounded domain only; thin black line, actual behavior.

A schematic of the behavior of scaled influence layer thickness is shown in Fig. 2.9. The main reason for more peculiar behavior around $c = 0$, where Stokes' analogy is not valid, may be threefold: (1) where $|c|$ approaches zero, $\delta_{b/s}$ does not infinitely increase due to the bounded domain; (2) in the range of $0 < c < 1$ the effect of critical layer (or quasi-resonance) appears; (3) around $c \approx -0.34$ the meaning of the defined influence layer thickness becomes ambiguous, where the RSS profile has double peaks (positive and negative) as exemplified in Fig. 2.10.

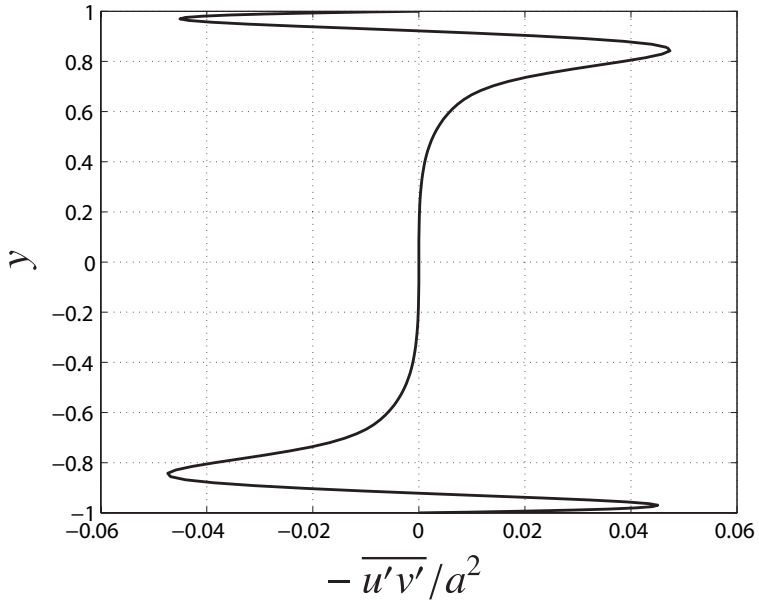

Figure 2.10: Profile of the RSS when $\Delta D \approx 0$ induced by the varicose mode traveling wave. ($c = -0.34$, $k = 0.5$, and $\mathrm{Re} = 2000$).

In the followings, a phase analysis is made to discuss the mechanism of the drag reduction in the range of c where the above analogy holds. The RSS can be expressed as the product of the absolute value of the Fourier coefficients and the phase difference, i.e.,

$$-\overline{u'v'} = -\frac{1}{2}|\hat{u}||\hat{v}|\sin(\phi), \tag{2.18}$$

where ϕ is the phase difference between u' and v',

$$\phi = \arg\hat{u} - \arg\hat{v} + \frac{\pi}{2}. \tag{2.19}$$

According to Eq. (2.18), non-zero RSS is created when u' and v' depart from the quadrature ($\phi = 0$ or $\phi = \pm\pi$).

The sign of ΔD is determined by ϕ. Namely the drag decreases when

$$\begin{array}{ll} 0 < \phi < \pi & (-1 < y < 0), \\ -\pi < \phi < 0 & (0 < y < 1), \end{array} \tag{2.20}$$

and the drag increases when

$$\begin{array}{ll} -\pi < \phi < 0 & (-1 < y < 0), \\ 0 < \phi < \pi & (0 < y < 1). \end{array} \tag{2.21}$$

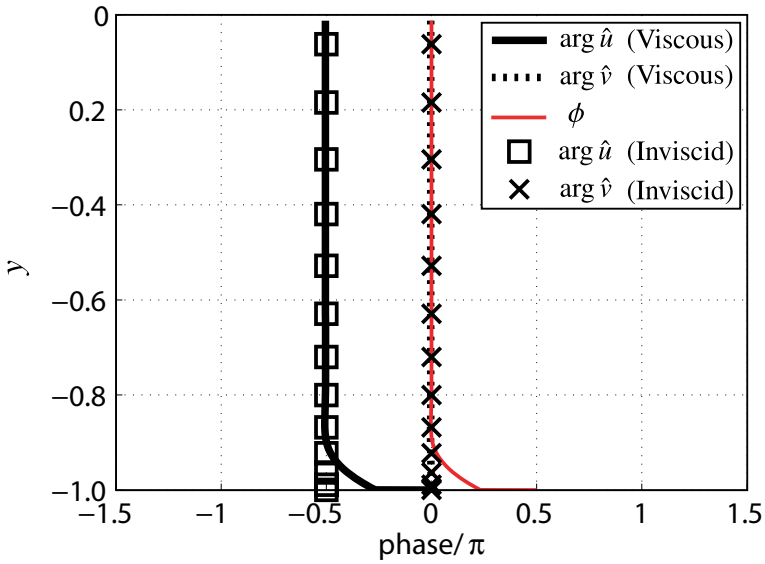

Figure 2.11: Profiles of phases of the Fourier coefficients for viscous and inviscid disturbances in drag reducing case by the upstream traveling wave ($k = 0.5$, $c = -1.5$, $\mathrm{Re} = 2000$, and varicose mode).

Again, this near-wall phase shift produces the RSS according to Eqs. (2.18)-(2.21).

Figure 2.11 shows the phase relationship between $\hat{u}$ and $\hat{v}$ in the lower half of the channel at the case of the maximum drag reduction. Hereafter, the ordinary phase relationship is defined as "viscous" phase relationship. The phase difference, ϕ, is found to be in the regions near the walls, and contributes the drag reduction according to Eq. (2.20). This non-quadrature is generated by the positive phase shift of $\hat{u}$, i.e., $\arg\hat{v} = 0$ but $\arg\hat{u} \neq -\pi/2$ in the region near the wall, as was pointed out by Min et al. (2006).

Figure 2.11 also shows the phases computed from the inviscid linear equations (Schmid and Hennningson, 2000), i.e., Eqs. (2.8)-(2.9) without the viscosity term, defined as "inviscid" phases. The inviscid phase relationship is found to be in quadrature. The viscous and inviscid phase relationships are similar except for the near-wall regions (hereafter which is defined as the "base phase relationship.") In the region near the wall, $\arg\hat{u}$ (viscous) is found to lead $\arg\hat{u}$ (inviscid), defined as the "near-wall phase shift". This viscous and inviscid comparison clearly shows that the near-wall phase shift is caused by the viscosity effect in the region near the wall. This region is

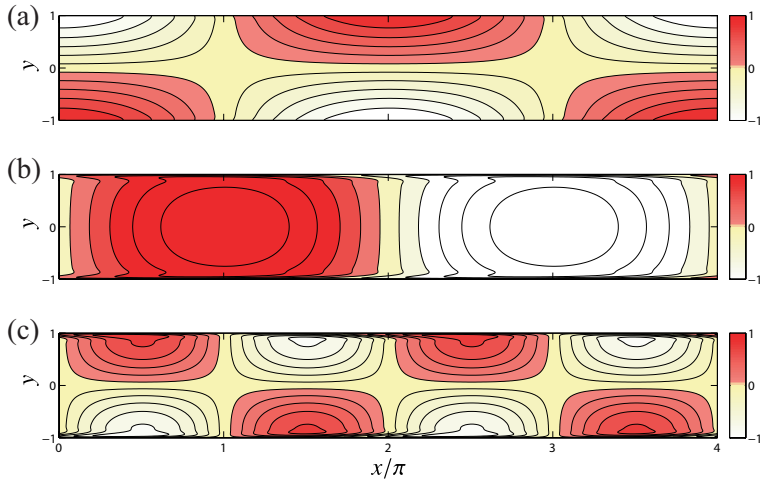

Figure 2.12: Disturbance fields: (a) v'/a, (b) u'/a, (c) $-u'v'/a^2$. The same condition as Fig. 2.11.

the influence layer which is affected by the blowing/suction.

Figure 2.12 shows the disturbance fields of wall-normal velocity, v', streamwise velocity, u', and their product, $-u'v'$, respectively, at $k = 0.5$, $c = -1.5$, and $\mathrm{Re} = 2000$. As shown in Fig. 2.12(a), the wall-normal velocity, v', induced by the traveling wave-like blowing/suction is antisymmetric due to the varicose control input. Figure 2.12(b) shows symmetric u' generated as a response of the system. Due to the subtle phase shift of u' near the wall, u' and v' become non-quadrature and non-zero values of $-\overline{u'v'}$ are created in the region near the wall as shown in Fig. 2.12(c). This $-u'v'$ is antisymmetric: negative and positive values appear more frequently near the lower and upper walls, respectively.

For comparison, the inviscid disturbance fields (computed by the inversed Fourier transformation of the solution of the inviscid linear equations) are depicted in Fig. 2.13. Again, the inviscid disturbance fields are found to be identical to the viscous disturbance fields except the region near the wall. Figure 2.14 shows the zoom-up view of u' in the region near the wall. The near-wall phase shift of viscous u' is clearly observed in the region near the wall. These results indicate that the base phase relationship is determined by the inviscid solution, whereas the near-wall phase shift, positive or negative, of streamwise velocity disturbance is induced by the viscosity in the region near

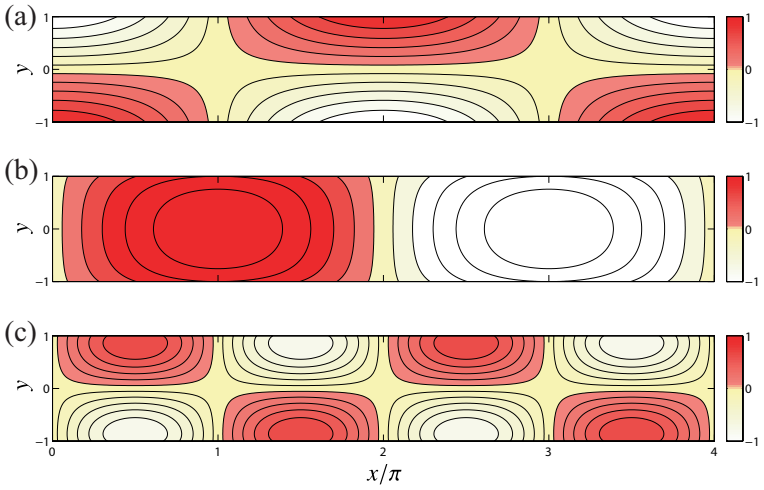

Figure 2.13: Disturbance fields computed from the inviscid equation: (a) v'/a, (b) u'/a, (c) $-u'v'/a^2$. The same condition as Fig. 2.11.

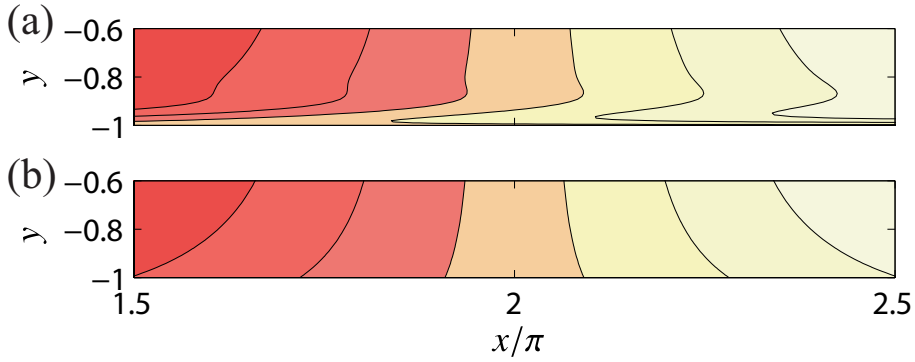

Figure 2.14: Zoom-up view of u' in the region near the wall: (a) viscous case (Fig. 2.12(b)), (b) inviscid case (Fig. 2.13(b)).

the wall and generates the non-quadrature between u' and v'.

The effect of the downstream traveling wave is also investigated. Figure 2.15 shows the RSS profile under $c = 1.5$ and $\mathrm{Re} = 2000$ for different k. The RSS profile is found to be positive and negative in the region near the lower and upper walls, respectively, which produces the drag increase, $\Delta D > 0$, according to Eq. (2.1).

Figure 2.16 shows the viscous and inviscid phase relationships of the drag increase case ($k = 0.5$, $c = 1.5$, and $\mathrm{Re} = 2000$). It is clear that the drag increase can be ex-

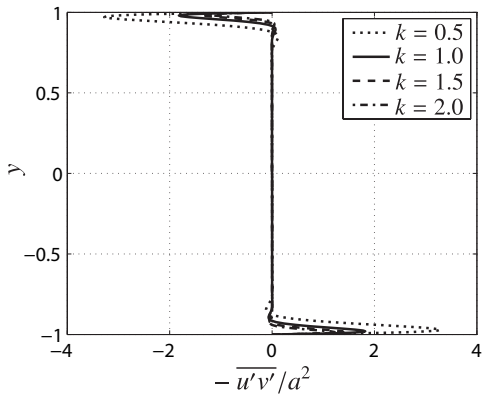

Figure 2.15: Profile of the RSS induced by downstream ($c = 1.5$) traveling wave for different k (Re $= 2000$ and varicose mode).

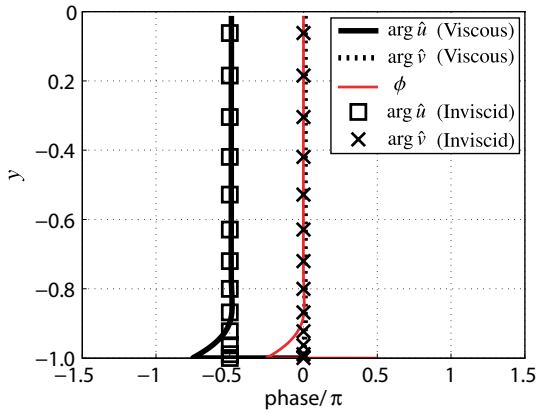

Figure 2.16: Profiles of phases of the Fourier coefficients for viscous and inviscid disturbances in drag increasing case by the downstream traveling wave ($k = 0.5$, $c = 1.5$, Re $= 2000$, and varicose mode).

plained by exactly the same argument (but with the opposite sign) as that made for drag reduction.

2.3.2 Sinuous Mode

Figure 2.17 shows the drag increment, ΔD, as a function of c, for the sinuous mode traveling wave. We obtain drag reduction ($\Delta D < 0$) by the upstream traveling wave

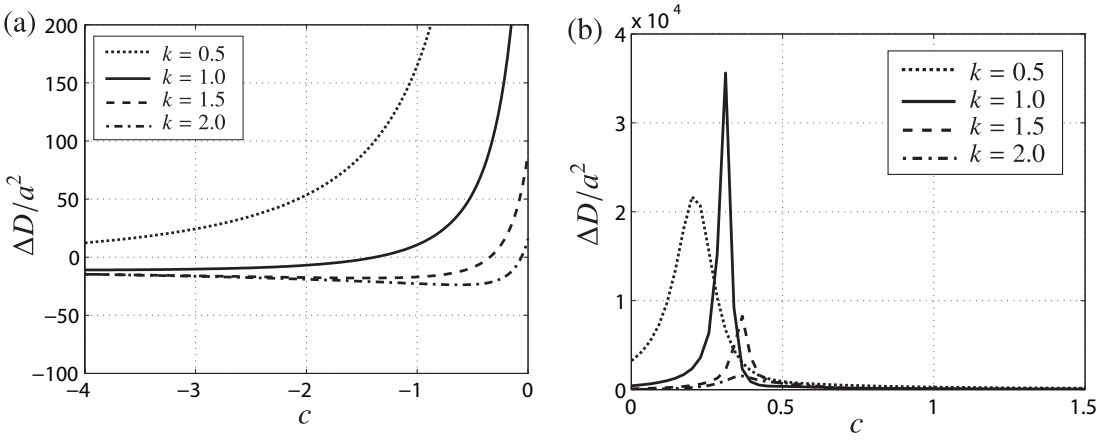

Figure 2.17: Normalized drag increment, $\Delta D/a^2$ as a function of c under different k (Re $= 2000$, sinuous mode): (a) upstream traveling waves $(c < 0)$, (b) downstream traveling waves $(c > 0)$.

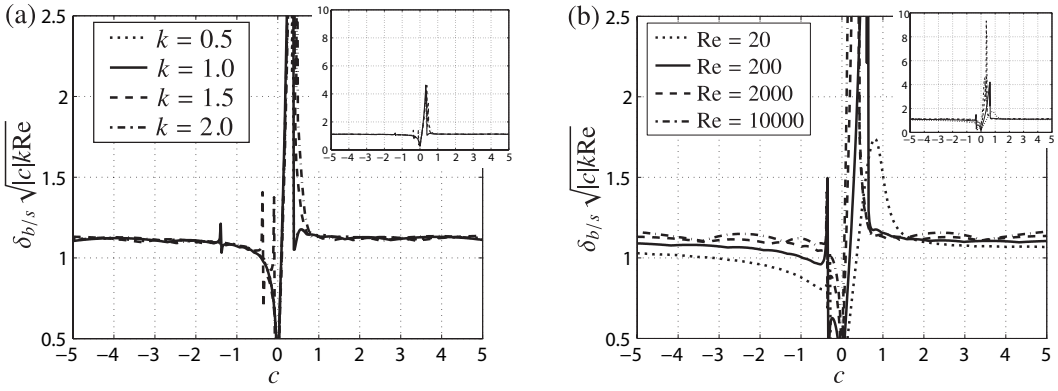

Figure 2.18: The scaled influence layer thickness, $\delta_{b/s}\sqrt{|c|k\mathrm{Re}}$, as a function of wavespeed, c (sinuous mode): (a) for different k $(\mathrm{Re} = 2000)$; (b) for different Re $(k = 1.5)$.

for $k = 1.0$, 1.5, and 2.0. However, ΔD is found to be positive in the case of $k = 0.5$. Similarly to the varicose mode, ΔD is found to be positive by the downstream traveling wave. A large drag increase is observed in the range of $0 < c < 0.5$ due to the critical layer and the flow instability. For the faster traveling wave, $c > 0.5$, ΔD is found to approach zero.

Figure 2.18 shows that the scaled influence layer thickness, $\delta_{b/s}\sqrt{|c|k\mathrm{Re}}$, is kept constant in the range of $|c| > 1$ regardless of k. The case of the Re $= 20$ gives slightly

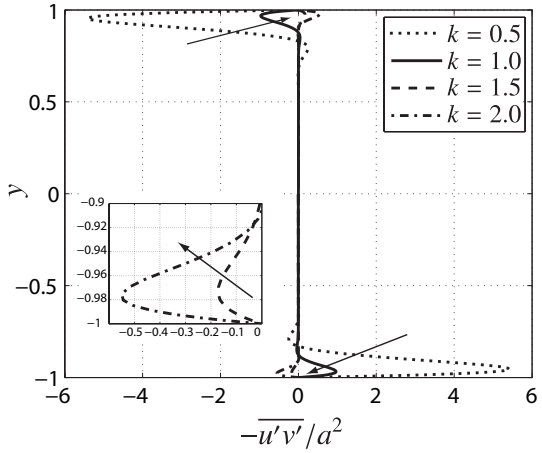

Figure 2.19: Profile of the RSS induced by the sinuous mode traveling wave for different k ($c = -0.5$ and $\mathrm{Re} = 2000$).

lower values than the other cases of $\mathrm{Re} \geq 200$. This trend is common to the varicose mode.

Figure 2.19 shows the RSS profile under different k at $c = -0.5$ and $\mathrm{Re} = 2000$. The RSS for $k = 0.5$ and $k = 1.0$ is found to be negative and positive in the region near the upper and lower walls, respectively, which corresponds to the drag increase. As increasing the wavenumber, the peak of the RSS is found to decrease and becomes negative which leads to the drag reduction.

The phase relationships in the lower half of channel for $k = 0.5$ and $k = 2.0$ are shown in Fig. 2.20(a) and (b), respectively. In both cases, non-quadrature appears in the region near the wall due to the positive phase shift of $\arg \hat{u}$ (viscous). Whereas the non-quadrature in $k = 2.0$ results in drag reduction similar to that in the varicose mode, that for $k = 0.5$ leads to the drag increase. This is due to the difference of the base phase relationship, i.e., $\hat{u} = -\pi/2$ for $k = 2.0$ (similarly to the varicose mode), $\arg \hat{u} = \pi/2$ for $k = 0.5$ (opposite to the varicose mode). This difference can better be understood by the streamlines, as shown in Fig. 2.21. Whereas the blowing from both walls (i.e., varicose mode) accelerate the bulk flow similarly to a contraction, blowing and suction from each wall (i.e., the sinuous mode) laterally displaces the fluid to result in deceleration (acceleration) of the bulk flow on the blowing (suction) side.

The distributions of velocity disturbances and their products for $k = 0.5$ are shown

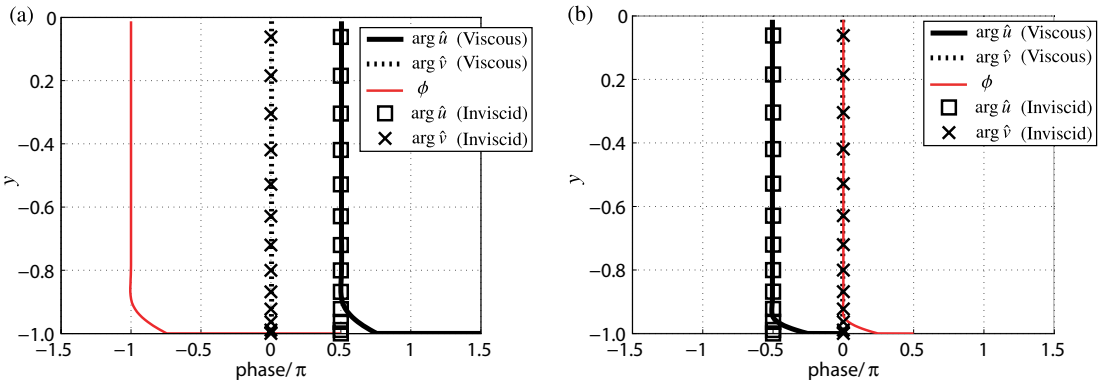

Figure 2.20: Profile of the phase of the Fourier coefficients for viscous and inviscid disturbance induced by the sinuous mode traveling wave ($c = -1.5$ and $\mathrm{Re} = 2000$): (a) $k = 0.5$; (b) $k = 2.0$.

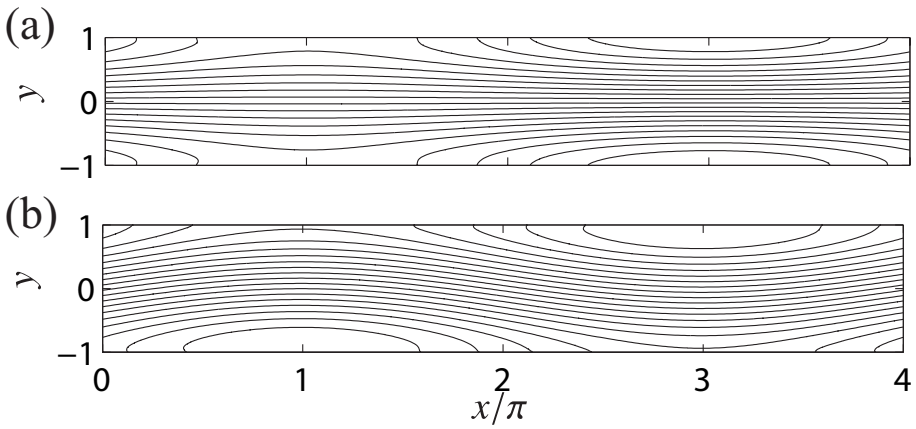

Figure 2.21: Streamline by the wave of (a) varicose mode, (b) sinuous mode ($k = 0.5$, $c = -1.5$, and $\mathrm{Re} = 2000$).

in Fig. 2.22. Large v' appears in the center region of the channel as shown in Fig. 2.22(a) because the wall-normal velocity blown from the lower (upper) directly penetrates into the upper (suction) region due to the small wavenumber, $k = 0.5$ (i.e., long wavelength). The vertical fluid motion induces u' as shown in Fig. 2.22(b). Unlike the cases of varicose mode (Figs. 2.12 and 2.13) and the cases of sinuous mode at higher wave numbers (Fig. 2.23), the base phase of u' delays and leads $\pi/2$ from that of v' in the upper and lower half region, respectively. Although, the near-wall phase shift of u' in the region near the wall is induced in exactly the same manner as that for the varicose

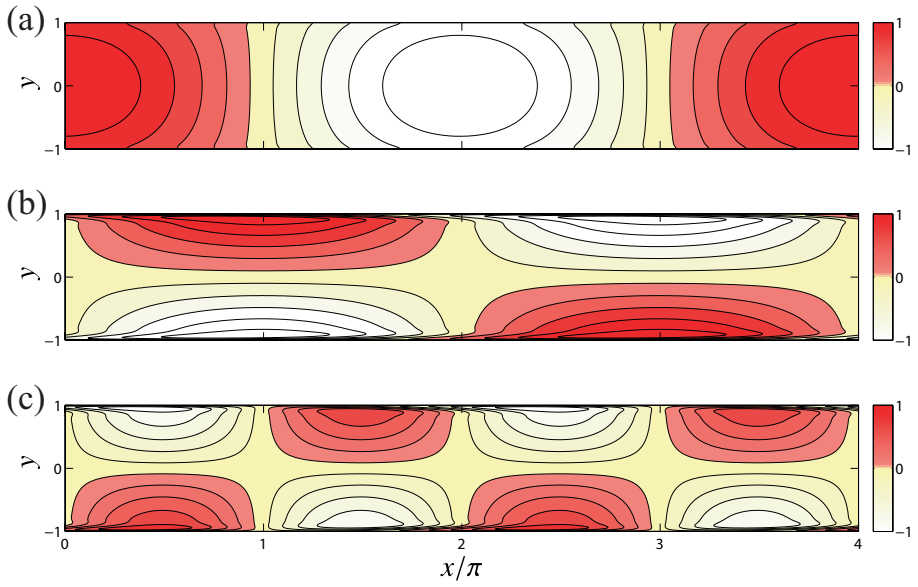

Figure 2.22: Disturbance fields at $k = 0.5$ (sinuous mode, $c = -1.5$, and Re $= 2000$): (a) v'/a; (b) u'/a; (c) $-u'v'/a^2$.

mode, the difference in the base phase relationship results in the dominance of positive $-u'v'$ (Fig. 2.22(c)) and the drag increase.

2.3.3 Parametric study

The scaled influence layer thickness and the phase relationship are computed for wider range of parameters. We compute about 500,000 cases for the varicose and the sinuous modes, in the range of $0.01 < k < 5$ and $-5 < c < 5$. The intervals of k and c are set to be 0.01.

Figures 2.24(a) and (b) show the maps of the scaled influence layer thickness by the varicose and sinuous mode traveling waves, respectively. The scaled influence layer thickness is found to be constant, except for the region near $c \simeq 0$, which confirms that the analogy between present control and Stokes' second problem holds in wider ranges of parameters.

In the previous subsections, the phase analysis explains the mechanism: the non-quadrature between velocity disturbances creates the RSS which generates ΔD. The

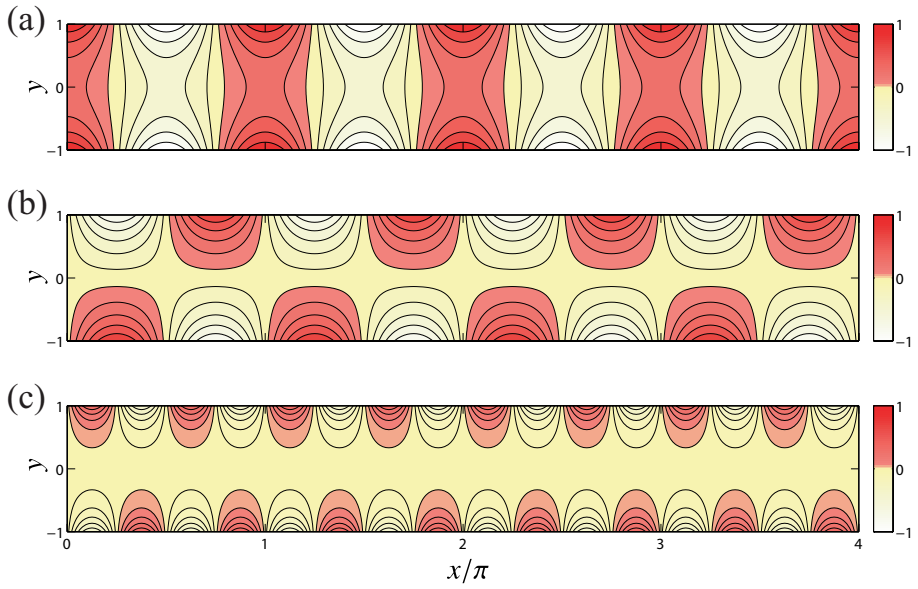

Figure 2.23: Disturbance fields at $k = 2.0$ (sinuous mode, $c = -1.5$, and $\mathrm{Re} = 2000$): (a) v'/a; (b) u'/a; (c) $-u'v'/a^2$.

non-quadrature appears as the phase difference, ϕ. In order to make a unified explanation for all cases studied, we propose the following decomposition of ϕ:

$$\phi = \Phi + \alpha. \tag{2.22}$$

Here, Φ is the base phase difference defined as the departure from quadrature determined by the inviscid disturbance, i.e.,

$$\Phi = \arg\hat{u}\ (\text{inviscid}) - \arg\hat{v}\ (\text{inviscid}) + \frac{\pi}{2}, \tag{2.23}$$

and α is the near-wall phase shift, which is defined as the difference between the $\arg\hat{u}$ (viscous) and the $\arg\hat{u}$ (inviscid), i.e.,

$$\alpha = \arg\hat{u}\ (\text{viscous}) - \arg\hat{u}\ (\text{inviscid}). \tag{2.24}$$

This decomposition enables us to easily overview the effect of the base and the near-wall phase relationship on the drag for different parameter sets of c and k. For convenience, the base phase difference, Φ, and the near-wall phase shift, α, are computed where $|-\overline{u'v'}|$ takes maximum value in the lower half of the channel.

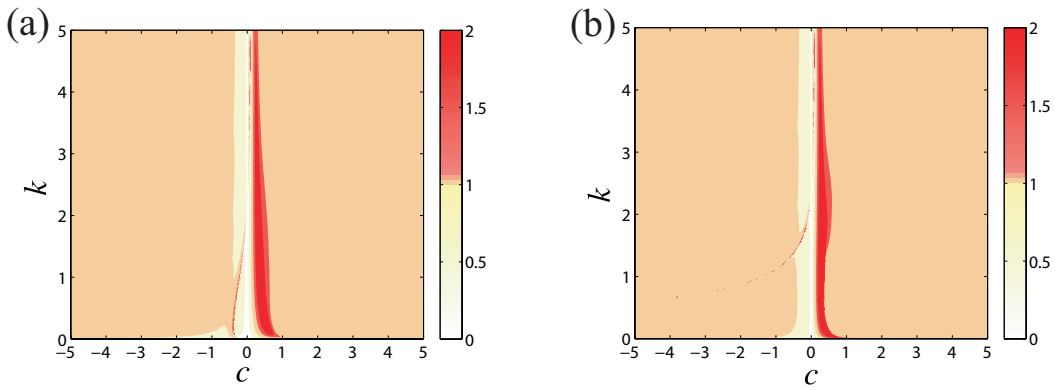

Figure 2.24: Map of the scaled influence layer thickness (Re = 2000): (a) varicose mode; (b) sinuous mode.

Figure 2.25 shows the distributions of Φ, α, and ΔD by the varicose and sinuous modes traveling wave at Re = 2000. The left column on this figure shows the results by the varicose mode. The phase and ΔD are normalized by π and a^2, respectively. Figure 2.25 shows that Φ is zero in the most region in accordance with Fig. 2.11.

Figure 2.25(middle, left) shows the distribution of the near-wall phase shift, α/π: the upstream traveling wave ($c < 0$) creates the positive phase shift of streamwise velocity as visualized in Fig. 2.12 and the downstream traveling wave ($c > 0$) induces negative phase shift. The sign of α/π does not depend on k. The phase difference, ϕ, which consists of Φ and α, results in

$$0 < \phi < \pi \ (c < 0)\,, \tag{2.25}$$

$$-\pi < \phi < 0 \ (c > 0)\,, \tag{2.26}$$

in the lower half region of the channel. According to Eqs. (2.20)-(2.21), the drag reduction and increase are obtained by the upstream and the downstream traveling waves, respectively, as confirmed by Fig. 2.25(bottom, left).

The phase relationship and ΔD in the case of sinuous mode traveling wave are shown in Fig. 2.25 (right column). Although the phase relationships, Φ and α, are basically similar to those of the varicose mode, a region of $\Phi/\pi = 1$ is found for small k and $c < 0$. This is due to the penetration of wall-normal velocity as observed in

Fig. 2.22. Accordingly, the phase difference, ϕ, becomes

$$0 < \phi < \pi \ (c < 0, \text{small } k), \tag{2.27}$$

$$-\pi < \phi < 0 \ (\text{otherwise}), \tag{2.28}$$

in the lower half region of the channel. These ϕ lead the drag reduction and increase as shown in Fig. 2.25 (bottom, right), respectively.

2.4 Summary

The skin-friction drag reduction mechanism by the traveling wave-like blowing/suction control of Min et al. (2006) is investigated in the two-dimensional laminar Poiseuille flow. The velocity disturbances are computed by the linear analysis with the Chebyshev collocation points method. The drag increment by the control input is predicted by using the identity equation between the skin-friction drag increment and the Reynolds shear stress (Bewley and Aamo, 2004; Fukagata et al., 2002).

It is confirmed that the analogy between the present control and the Stokes' second problem holds. The scaled influence layer thickness is found to be constant, for different parameters, k, c, and Re, and the wavemodes (the varicose and the sinuous modes). This scaling is similar to that used for the analysis of drag reduction by spanwise wall oscillation.

The phase analysis shows the mechanism of the drag reduction and increase. The Reynolds shear stress, which contributes to the drag increment from the laminar level, is induced by the non-quadrature between velocity disturbances. This non-quadrature is decomposed to the base phase relationship and near-wall phase shift. The base phase relationship agrees with that by the solution of the inviscid disturbance equations. For the case of the varicose mode, the base phase relationship is found to be independent of wavenumber, i.e., v' leads $\pi/2$ from u' in the lower half region of the channel. For the sinuous mode, the phase reversal of u' is observed at the small wavenumbers (i.e., long wavelength). In the region near the walls, the viscosity induces the near-wall phase shift. The upstream and downstream traveling waves induce the negative and positive phase shift of streamwise velocity, respectively, for the both wavemodes.

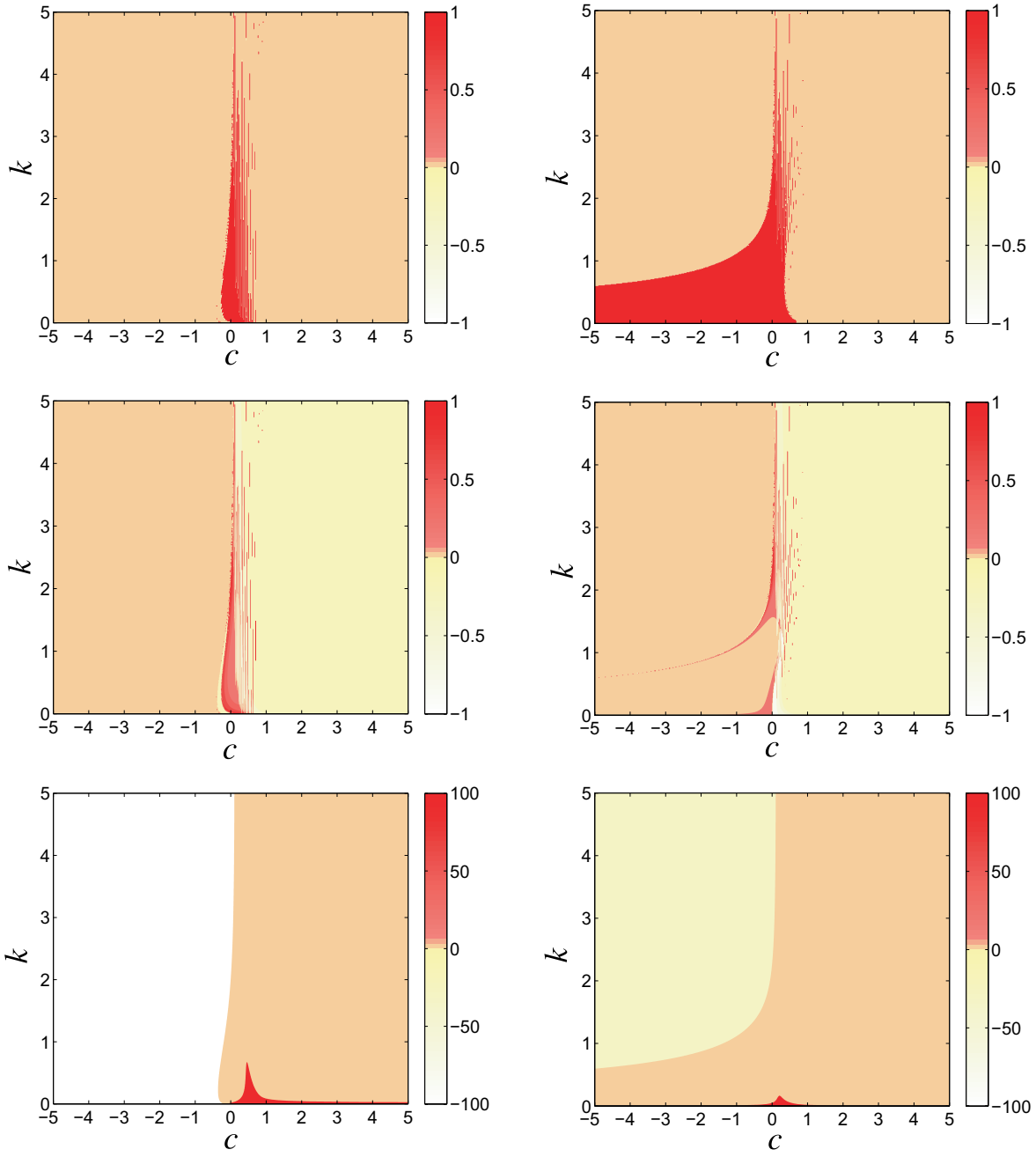

Figure 2.25: Left and right column are varicose and sinuous modes, respectively, (Re = 2000). Top, the base phase difference, Φ/π; middle, the near-wall phase shift, α/π; bottom, the drag increment, $\Delta D/a^2$.

Chapter 3

Low Reynolds number turbulent flow

The control effect in a fully developed channel flow under the traveling wave-like blowing/suction control is studied by means of a direct numerical simulation at $\mathrm{Re}_\tau \approx 180$. The control performance, i.e., drag reduction and net saving rates, is investigated. The mechanism of the drag reduction is revealed by using three component decomposition and a phase analysis. Traveling wave-like wall-normal forcing is also considered to compare to the blowing/suction control.

3.1 Direct numerical simulation

A DNS is the simulation without using any turbulence model; namely, the mesh size should be set as small as the Kolmogorov scale. The governing equations are the continuity and Navier-Stokes equations, which read for an incompressible flow, respectively,

$$\frac{\partial u_n}{\partial x_n} = 0, \tag{3.1}$$

$$\frac{\partial u_n}{\partial t} + u_m \frac{\partial u_n}{\partial x_m} = -\frac{\partial p}{\partial x_n} + \frac{1}{\mathrm{Re_b}} \frac{\partial^2 u_n}{\partial x_k \partial x_k} + F_n, \tag{3.2}$$

where F_n denotes a body force (considered in Chap. 3.3). The reference length and velocity are the channel half-width, δ^*, and the twice bulk-mean velocity, $2u_b^*$, respectively. The bulk Reynolds number is defined as $\mathrm{Re_b} = 2u_b^*\delta^*/\nu^*$, where the kinematic viscosity is ν^*. The asterisk denotes the dimensional variable.

Table 3.1: Specification of the DNS code for the channel flow.

Time integration	Low storage 3rd order RK scheme
Advection term	Energy conservative second order finite difference method
Diffusion term	Second order Crank-Nicolson method
Poisson solver for pressure	homogeneous directions: fast Fourier transform
	wall-normal direction: tridiagonal matrix solver
Coupling method for velocity and pressure	SMAC method

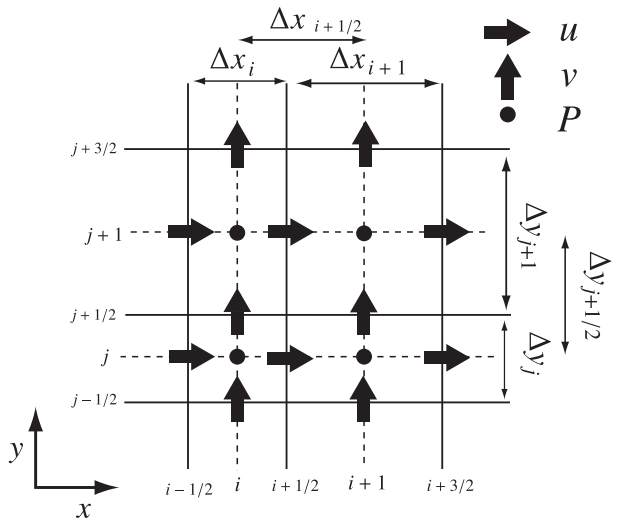

Figure 3.1: Nonuniform staggered grid system (two-dimensional view).

The employed DNS code is based on the energy conservative FDM. The original code was developed for a pipe flow (Fukagata and Kasagi, 2002) and modified for the channel flow (Fukagata et al., 2006). The specification of this code is tabulated in Table 3.1.

Figure 3.1 shows the schematic of the nonuniform staggered grid system (two-dimensional view, for simplicity). The velocities and the pressure are defined at the cell surface and the cell center, respectively. The first and second derivatives are dis-

cretized, e.g., as

$$\left[\frac{\delta v}{\delta y}\right]_{i,j,k} = \frac{v_{i,j+1/2,k} - v_{i,j-1/2,k}}{\Delta y_j}, \tag{3.3}$$

$$\left[\frac{\delta^2 v}{\delta y \delta y}\right]_{i,j+1/2,k} = \frac{1}{\Delta y_{j+1/2}}\left(\frac{v_{i,j+3/2,k} - v_{i,j+1/2,k}}{\Delta y_{j+1}} - \frac{v_{i,j+1/2,k} - v_{i,j-1/2,k}}{\Delta y_j}\right), \tag{3.4}$$

where the subscripts i, j, and k denote the stencils in x, y, and z directions, respectively.

Equations (3.1) and (3.2) discretized by using the second-order energy-conservative FDM (Bewley, 1999; Ham et al., 2002; Kajishima, 1999a) then read

$$\frac{\delta u_n}{\delta x_n} = 0, \tag{3.5}$$

$$\frac{\delta u_n}{\delta t} = -\frac{\delta \{u_k\}^{x_n} \overline{u_n}^{x_k}}{\delta x_k} - \frac{\delta p}{\delta x_n} + \frac{1}{\mathrm{Re}} \frac{\delta^2 u_n}{\delta x_k \delta x_k}. \tag{3.6}$$

Here, the overbar and $\{\cdot\}$ denote the arithmetic and volume-flux averages (Fukagata and Kasagi, 2002), respectively. These are defined, e.g., as

$$\overline{u}^y_{i+1/2,j+1/2,k} = \frac{u_{i+1/2,j+1,k} + u_{i+1/2,j,k}}{2}, \tag{3.7}$$

and

$$\begin{cases} \{u\}^x_{i+1,j,k} = \dfrac{u_{i+1/2,j,k} + u_{i-1/2,j,k}}{2}, \\ \{u\}^y_{i+1/2,j+1/2,k} = \dfrac{\Delta y_{j+1} u_{i+1/2,j+1,k} + \Delta y_j u_{i+1/2,j,k}}{\Delta y_{j+1} + \Delta y_j}, \end{cases} \tag{3.8}$$

where the superscripts (x, y, and z) denote the direction of interpolation.

The discretized advection term has been verified (Bewley, 1999; Ham et al., 2002; Kajishima, 1999a) to be momentum- and energy-conservative (strictly speaking, squared-value-conservative) given that the discretized continuity equation is satisfied. Thus, the discretized equations (3.5) and (3.6) conserve not only the mass and momentum but also the total kinetic energy in the inviscid limit.

Figure 3.2 shows the flow configuration. The computational domain is $L_x \times L_y \times L_z$. The mean flow is driven by the mean pressure gradient to keep a constant flow rate. All simulations are run at $\mathrm{Re_b} = 5600$, which corresponds to $\mathrm{Re}_\tau \approx 180$, and they started from the velocity field of the uncontrolled fully developed channel flow. As a

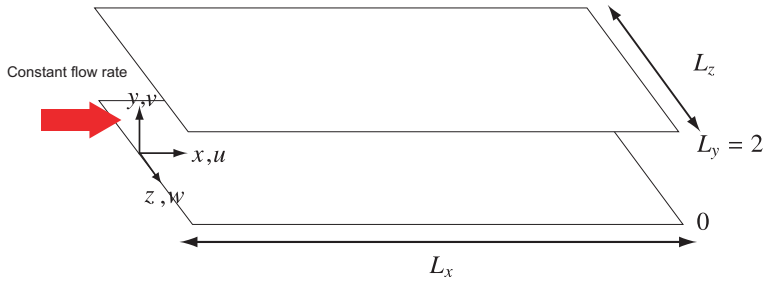

Figure 3.2: Flow configuration and coordinate system of the channel flow.

Table 3.2: Grid dependency of the uncontrolled channel flow at $\mathrm{Re}_b = 5600$

	$L_x \times L_y \times L_z$	$N_x \times N_y \times N_z$	Δx^+, $\Delta y^+_{\mathrm{min}}$, Δz^+	D
Case 1	$2\pi \times 2 \times 3.5$	$128 \times 96 \times 128$	8.69, 0.096, 2.42	7.55 ± 0.21
Case 1W	$4\pi \times 2 \times 3.5$	$256 \times 96 \times 128$	8.69, 0.096, 2.42	7.43 ± 0.56
Case 2	$2\pi \times 2 \times 3.5$	$256 \times 96 \times 128$	4.24, 0.096, 2.42	7.44 ± 0.76
Case 3	$2\pi \times 2 \times 3.5$	$128 \times 96 \times 256$	8.69, 0.096, 1.21	7.50 ± 0.30
Case 4	$2\pi \times 2 \times 3.5$	$256 \times 96 \times 256$	4.24, 0.096, 1.21	7.35 ± 0.30
Case 5	$2\pi \times 2 \times 3.5$	$128 \times 192 \times 128$	8.69, 0.024, 2.42	7.51 ± 0.10

verification of this computational code, the skin-friction drag for the different number of grid points and the computational domain is tabulated in Table 3.2, where major dependency on the grid or the domain size is not found. As a validation of this code, the statistics of Case 1W are presented in Fig 3.3, which shows an excellent agreement with the spectral DNS data of Moser et al. (1999).

Figure 3.4 visualizes the instantaneous field in $z-y$ plane in the region near the wall. The streamwise vortical structure can be identified by the low pressure fluctuation and the negative Q value: the core of vortex exists at $z^+ \approx 320$ and $y^+ \approx 20$. Due to the counter rotating motion of this vortex, the low speed fluid ($u' < 0$) is ejected upward and the high speed fluid ($u' > 0$) is swept downward to the wall region, therefore the RSS is generated around of this vortex. The Q value is the second invariant of the strain rate tensor:

$$Q = \frac{1}{2}\left(W_{ij}W_{ij} - S_{ij}S_{ij}\right) \tag{3.9}$$

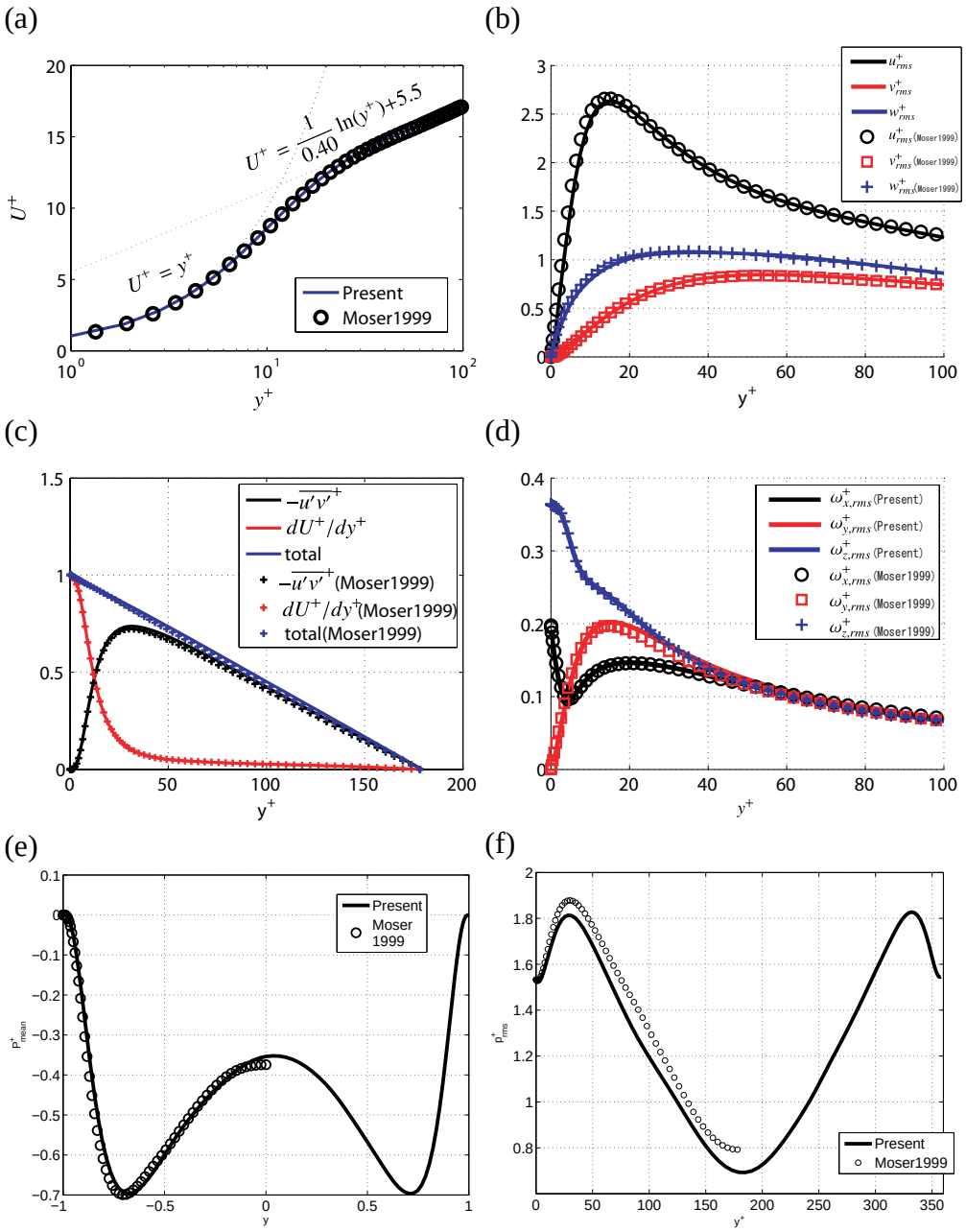

Figure 3.3: Comparison between the present DNS and the result of Moser et al. (1999): (a) mean velocity; (b) rms value of velocity fluctuations; (c) RSS and velocity gradient; (b) rms of vorticity fluctuations; (e) mean pressure; (f) rms of pressure fluctuation.

where S_{ij} and W_{ij} are

$$S_{ij} = \frac{1}{2}\left(\frac{\partial u_i}{\partial x_j} + \frac{\partial u_j}{\partial x_i}\right), \tag{3.10}$$

$$W_{ij} = \frac{1}{2}\left(\frac{\partial u_i}{\partial x_j} - \frac{\partial u_j}{\partial x_i}\right). \tag{3.11}$$

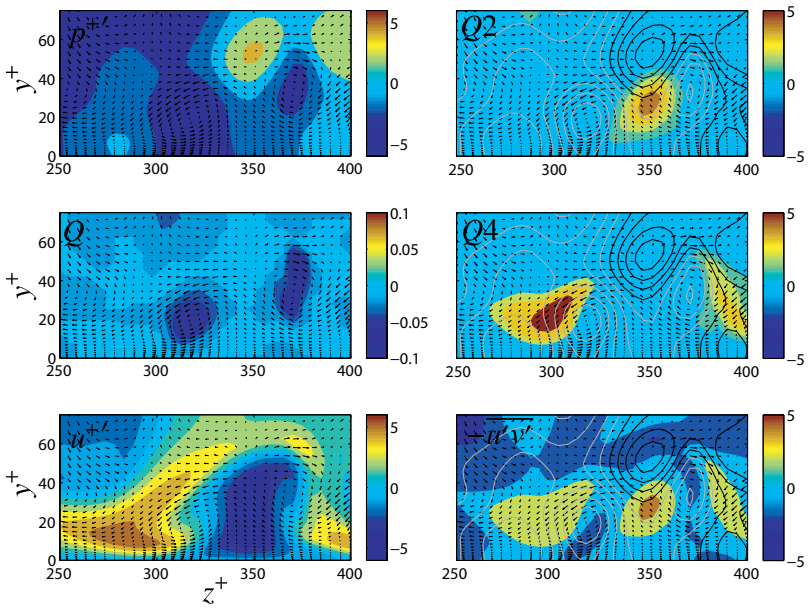

Figure 3.4: Instantaneous view of the cross section ($z-y$ plane) in the region near the wall. The color are pressure fluctuation (left, top), Q value (middle), u' (bottom), $Q2$ event of the RSS ($u'<0$ and $v'>0$) (right, top); $Q4$ event ($u'>0$ and $v'<0$) (middle); the RSS (bottom). The line indicates pressure fluctuation: black, $p'>0$; white, $p'<0$.

3.2 Transport equation of Reynolds Stress and turbulent kinetic energy

The second moment of the velocity fluctuations is called the Reynolds stress, $u_i u_j$, (referred to as RS, hereafter) which is an indicator of turbulent flow behavior (Mansour et al., 1988). The derivation process of the transport equation of the RS budget in the continuous space can be summarized as follows: 1) apply the Reynolds decomposition to the velocity and pressure, i.e., $u_n = U_n + u'_n$ and $p = P + p'$ (where the capital letter denotes the mean value) and substitute them into Eq. (3.2); 2) subtract the transport equation for mean velocities; 3) multiply $2u'$; and 4) take the ensemble average.

The transport equation of the RS is expressed as

$$\frac{\partial \langle u'_n u'_m \rangle_a}{\partial t} + C_{nm} = P_{nm} + T_{nm} + \Psi_{nm} + \Phi_{nm} + D_{nm} + \varepsilon_{nm}, \tag{3.12}$$

where the angle bracket with subscript a denotes the ensemble average. The first and second terms in the left-hand-side (LHS) are the unsteady term and the mean convection term (C_{nm}), respectively. The right-hand-side (RHS) terms are the production (P_{nm}), turbulent diffusion (T_{nm}), pressure diffusion (Ψ_{nm}), pressure strain (Φ_{nm}), viscous diffusion (D_{nm}), and viscous dissipation (ε_{nm}), i.e.,

$$C_{nm} = U_k \frac{\partial \langle u'_n u'_m \rangle_a}{\partial x_k}, \tag{3.13}$$

$$P_{nm} = -\langle u'_m u'_k \rangle_a \frac{\partial U_n}{\partial x_k} - \langle u'_n u'_k \rangle_a \frac{\partial U_m}{\partial x_k}, \tag{3.14}$$

$$T_{nm} = -\frac{\partial \langle u'_k u'_m u'_n \rangle_a}{\partial x_k}, \tag{3.15}$$

$$\Psi_{nm} = -\frac{\partial \langle u'_m p' \rangle_a}{\partial x_n} - \frac{\partial \langle u'_n p' \rangle_a}{\partial x_m}, \tag{3.16}$$

$$\Phi_{nm} = \left\langle p' \frac{\partial u'_n}{\partial x_m} \right\rangle_a + \left\langle p' \frac{\partial u'_m}{\partial x_n} \right\rangle_a, \tag{3.17}$$

$$D_{nm} = \frac{1}{\mathrm{Re}} \frac{\partial^2 \langle u'_n u'_m \rangle_a}{\partial x_k \partial x_k}, \tag{3.18}$$

$$\varepsilon_{nm} = -\frac{2}{\mathrm{Re}} \left\langle \frac{\partial u'_n}{\partial x_m} \frac{\partial u'_m}{\partial x_n} \right\rangle_a, \tag{3.19}$$

where Einstein's summation convention holds for the dummy index k.

The TKE is a sum of Reynolds normal stresses, i.e.,

$$K = \frac{1}{2}\left(\langle u_1' u_1' \rangle_a + \langle u_2' u_2' \rangle_a + \langle u_3' u_3' \rangle_a\right), \tag{3.20}$$

and the TKE budget reads

$$\frac{\partial K}{\partial t} + C_K = P_K + T_K + \Psi_K + \Phi_K + D_K + \varepsilon_K. \tag{3.21}$$

Each term in RHS is a half of the summation of the three normal components of the corresponding term in the RS budget, e.g., $P_K = \frac{1}{2}\sum_{n=1}^{3} P_{nn}$.

3.2.1 Discretization of Reynolds stress and turbulent kinetic energy budget

We define the Reynolds normal stress component ($\langle u_n' u_n' \rangle$, $n = 1...3$) on each cell surface where the velocity component u_n is defined. Hereafter, we omit the angle bracket of the ensemble average for notational simplicity.

The discretized terms composing the RS budget can be derived in the same manner as we derived the RS budget in the continuous space. First, u_n' is multiplied to the discretized x_n-momentum equation. The u_n-multiplied terms are then divided and/or merged to have the similar mathematical forms as those in the continuous space. At this step, the relevant interpolation schemes are used so that unwanted terms properly vanishes under the discretized continuity.

We show the detailed derivation process of the present consistent scheme. For brevity, we take the production and turbulent diffusion terms in RS budget for example. We also assume two-dimensional flow in $x-y$ plane for notational simplicity. Extension to three dimensional case is straightforward and the other terms can be derived in the similar manner. The Reynolds decomposition, ($u = U + u'$, $v = v'$) is applied to the convective term of Eq. (3.6). By multiplying the twice fluctuation of streamwise velocity, $2u'_{i+1/2,j}$, reads

$$\left[-2u'\frac{\delta\{v\}^x\overline{u}^y}{\delta y}\right]_{i+1/2,j} = \left[-2u'\frac{\delta\{v'\}^x\overline{U}^y}{\delta y}\right]_{i+1/2,j} + \left[-2u'\frac{\delta\{v'\}^x\overline{u'}^y}{\delta y}\right]_{i+1/2,j}, \tag{3.22}$$

where the index for stencil (k) is omitted.

First, the production term is considered. The first term of RHS of Eq. (3.22) becomes

$$\begin{aligned}
\left[-2u'\frac{\delta\{v'\}^x\overline{U}^y}{\delta y}\right]_{i+1/2,j} &= -2u'_{i+1/2,j}\frac{1}{\Delta y_j}\left(\left[\{v'\}^x\overline{U}^y\right]_{i+1/2,j+1/2}-\left[\{v'\}^x\overline{U}^y\right]_{i+1/2,j-1/2}\right), \\
&= -\frac{2u'_{i+1/2,j}}{\Delta y_j}\left(\overline{\{v'\}^x}^y_{i+1/2,j}\overline{U}^y_{i+1/2,j+1/2}-\overline{\{v'\}^x}^y_{i+1/2,j}\overline{U}^y_{i+1/2,j-1/2}\right) \\
&\quad -\frac{2u'_{i+1/2,j}}{\Delta y_j}\left(\frac{1}{2}\left(\{v'\}^x_{i+1/2,j+1/2}-\{v'\}^x_{i+1/2,j-1/2}\right)\overline{U}^y_{i+1/2,j+1/2}\right. \\
&\quad \left.+\frac{1}{2}\left(\{v'\}^x_{i+1/2,j+1/2}-\{v'\}^x_{i+1/2,j-1/2}\right)\overline{U}^y_{i+1/2,j-1/2}\right), \\
&= \left[-2u'\overline{\{v'\}^x}^y\frac{\delta\overline{U}^y}{\delta y}\right]_{i+1/2,j}+\left[-2u'\overline{\overline{U}^y}^y\frac{\delta\{v'\}^x}{\delta y}\right]_{i+1/2,j}, \\
&= \left[-2u'\overline{\{v'\}^x}^y\frac{\delta\overline{U}^y}{\delta y}\right]_{i+1/2,j}+\left[-2u'U\frac{\delta\{v'\}^x}{\delta y}\right]_{i+1/2,j} \\
&\quad +\mathcal{O}(\Delta y^2), \qquad (3.23)
\end{aligned}$$

where the identity equations, e.g.,

$$\{v'\}^x_{i+1/2,j+1/2} = \overline{\{v'\}^x}^y_{i+1/2,j}+\frac{1}{2}\left(\{v'\}^x_{i+1/2,j+1/2}-\{v'\}^x_{i+1/2,j-1/2}\right), \quad (3.24)$$

$$\{v'\}^x_{i+1/2,j-1/2} = \overline{\{v'\}^x}^y_{i+1/2,j}+\frac{1}{2}\left(\{v'\}^x_{i+1/2,j-1/2}-\{v'\}^x_{i+1/2,j+1/2}\right). \quad (3.25)$$

have been used. The first term of Eq. (3.23) is the production term. The second term vanishes due to the continuity in two cells sandwiching $i+1/2, j$ because a similar term (i.e., $[-2u'U\delta\{u'\}^y/\delta x]_{i+1/2,j}$) is derived from the x-derivative component of the advection term.

Second, the turbulent diffusion term is considered. The second term of RHS of

Eq. (3.22) becomes

$$\begin{aligned}
\left[-2u'\frac{\delta\{v'\}^x\overline{u'}^y}{\delta y}\right]_{i+1/2,j} &= -2u'_{i+1/2,j}\frac{1}{\Delta y_j}\left(\left[\{v'\}^x\overline{u'}^y\right]_{i+1/2,j+1/2}-\left[\{v'\}^x\overline{u'}^y\right]_{i+1/2,j-1/2}\right),\\
&= -\frac{2}{\Delta y_j}\left(u'_{i+1/2,j}\{v'\}^x_{i+1/2,j+1/2}\left(\frac{u'_{i+1/2,j+1}+u'_{i+1/2,j}}{2}\right)\right.\\
&\quad \left.-u'_{i+1/2,j}\{v'\}^x_{i+1/2,j-1/2}\left(\frac{u'_{i+1/2,j}+u'_{i+1/2,j-1}}{2}\right)\right),\\
&= -\frac{1}{\Delta y_j}(\{v'\}^x_{i+1/2,j+1/2}\underbrace{u'_{i+1/2,j+1}u'_{i+1/2,j}}_{\widetilde{u'u'}^y_{i+1/2,j+1/2}}\\
&\quad -\{v'\}^x_{i+1/2,j-1/2}\underbrace{u'_{i+1/2,j}u'_{i+1/2,j-1}}_{\widetilde{u'u'}^y_{i+1/2,j-1/2}})\\
&\quad -\frac{1}{\Delta y_j}u'^2_{i+1/2,j}\left(\{v'\}^x_{i+1/2,j+1/2}-\{v'\}^x_{i+1/2,j-1/2}\right),\\
&= \left[-\frac{\delta\{v'\}^x\widetilde{u'u'}^y}{\delta y}\right]_{i+1/2,j}+\left[-u'^2\frac{\delta\{v'\}^x}{\delta y}\right]_{i+1/2,j}. \qquad (3.26)
\end{aligned}$$

The first term of RHS is the turbulent diffusion term; the second term vanishes due to the continuity similarly to above.

As the result, the consistent discretization of RS budget can be expressed as

$$C_{nn} = \overline{\{U\}^{x_n}_k}^{x_k}\frac{\delta\widetilde{u'_nu'_n}^{x_k}}{\delta x_k}, \qquad (3.27)$$

$$P_{nn} = -2u'_n\overline{\{u'_k\}^{x_n}}^{x_k}\frac{\delta\overline{U_n}^{x_k}}{\delta x_k}, \qquad (3.28)$$

$$T_{nn} = -\frac{\delta}{\delta x_k}\{u'_k\}^{x_n}\widetilde{u'_nu'_n}^{x_k}, \qquad (3.29)$$

$$\Psi_{nn} = -2\frac{\delta}{\delta x_n}\overline{u'_n}^{x_n}p', \qquad (3.30)$$

$$\Phi_{nn} = 2p'\widehat{\frac{\delta u'_n}{\delta x_n}}^{x_n}, \qquad (3.31)$$

$$D_{nn} = \frac{1}{\mathrm{Re}}\frac{\delta^2u'^2_n}{\delta x_k\delta x_k}, \qquad (3.32)$$

$$\varepsilon_{nn} = -\frac{2}{\mathrm{Re}}\widehat{\frac{\delta u'_n}{\delta x_k}\frac{\delta u'_n}{\delta x_k}}^{x_k}, \qquad (3.33)$$

where the tilde and the hat denote the squared value and volume weighted average defined, e.g., as[4]

$$\left.\frac{\delta}{\delta y}\widetilde{f'g'}^{y}\right|_{i+1/2,j,k} = \frac{1}{\Delta y_j}\left(f'_{i+1/2,j+1,k}g'_{i+1/2,j,k} - f'_{i+1/2,j-1,k}g'_{i+1/2,j,k}\right), \quad (3.34)$$

and

$$\begin{cases} \widehat{u}^{x}_{i,j,k} &= \dfrac{\Delta x_{i+1/2}u_{i+1/2,j,k} + \Delta x_{i-1/2}u_{i-1/2,j,k}}{\Delta x_{i+1/2} + \Delta x_{i-1/2}}, \\ \widehat{u}^{y}_{i+1/2,j+1/2,k} &= \dfrac{\Delta y_{j+1}u_{i+1/2,j+1,k} + \Delta y_j u_{i+1/2,j,k}}{\Delta y_{j+1} + \Delta y_j}. \end{cases} \quad (3.35)$$

The f' and g' are arbitrary values. It should be noted that the volume weighted average (3.35) is different from the volume-flux average (3.8): the former uses the weight of volume regardless of the directions of velocity and interpolation, while the latter does not. Note that the viscous diffusion and dissipation terms, Eqs. (3.32) and (3.33), are identical to those presented by Kajishima (1999b).

The discretized TKE has conventionally (Ham et al., 2002; Morinishi et al., 1998) been defined by the arithmetic average at the center of the cell, i.e.,

$$K = \frac{1}{2}\overline{u'_n u'_n}^{x_n}, \quad (3.36)$$

where the summation convention holds for the dummy index n.

We define the Reynolds shear stress (RSS, $n \neq m$) on the center of the cell. The discretized time derivative term is expressed as

$$\left.\frac{\delta u'_n u'_m}{\delta t}\right|_{i,j} = \widehat{u'_m}^{x_m}\left.\widehat{\frac{\delta u'_n}{\delta t}}^{x_n}\right|_{i,j} + \widehat{u'_n}^{x_n}\left.\widehat{\frac{\delta u'_m}{\delta t}}^{x_m}\right|_{i,j}. \quad (3.37)$$

Here, the first and second terms in RHS represents the contributions from u'_n- and u'_m-momentum equations, respectively. The discretized RSS budget based on Eq. (3.37) can be expressed as

$$C_{nm} = \frac{1}{2}\left(\overline{\{U_k\}^{x_n}}^{x_k}\widehat{\frac{\delta}{\delta x_k}u'_n}\widetilde{\widehat{u'_m}^{x_m}}^{x_k x_k x_n} + \overline{\{U_k\}^{x_m}}^{x_k}\widehat{\frac{\delta}{\delta x_k}u'_m}\widetilde{\widehat{u'_n}^{x_n}}^{x_k x_k x_m}\right), \quad (3.38)$$

$$P_{nm} = -\widehat{u'_m}^{x_m}\left(\overline{\{u'_k\}^{x_n}}^{x_k}\widehat{\frac{\delta \overline{U_n}^{x_k}}{\delta x_k}}\right)^{x_n} - \widehat{u'_n}^{x_n}\left(\overline{\{u'_k\}^{x_m}}^{x_k}\widehat{\frac{\delta \overline{U_m}^{x_k}}{\delta x_k}}\right)^{x_m}, \quad (3.39)$$

$$T_{nm} = -\frac{1}{2}\left(\frac{\delta}{\delta x_k}\{\{u'_k\}^{x_n}\overline{u'_n}^{x_k}\}^{x_n}\overline{\widehat{u'_m}^{x_m}}^{x_k} + \frac{\delta}{\delta x_k}\{\{u'_k\}^{x_m}\overline{u'_m}^{x_k}\}^{x_m}\overline{\widehat{u'_n}^{x_n}}^{x_k}\right), \quad (3.40)$$

$$\Psi_{nm} = -\frac{\delta}{\delta x_n}\overline{\widehat{u'_m}^{x_m}}^{x_n}\overline{p'}^{x_n} - \frac{\delta}{\delta x_m}\overline{\widehat{u'_n}^{x_n}}^{x_m}\overline{p'}^{x_m}, \quad (3.41)$$

$$\Phi_{nm} = \left(\overline{p'}^{x_n}\widehat{\frac{\delta u'_m}{\delta x_n}}^{x_m}\right)^{x_n} + \left(\overline{p'}^{x_m}\widehat{\frac{\delta u'_n}{\delta x_m}}^{x_n}\right)^{x_m}, \quad (3.42)$$

$$D_{nm} = \frac{1}{\mathrm{Re}}\left(\frac{\delta^2}{\delta x_k \delta x_k}\widehat{u'_n}^{x_n}\widehat{u'_m}^{x_m}\right), \quad (3.43)$$

$$\varepsilon_{nm} = -\frac{1}{\mathrm{Re}}\left(\left(\widehat{\frac{\delta u'_n}{\delta x_k}}^{x_n}\widehat{\frac{\delta u'_m}{\delta x_k}}^{x_m}\right)^{x_k} + \left(\widehat{\frac{\delta u'_m}{\delta x_k}}^{x_m}\widehat{\frac{\delta u'_n}{\delta x_k}}^{x_n}\right)^{x_k}\right). \quad (3.44)$$

Because the energy-conservative FDM ensures the conservation of the TKE (i.e., K) but not of RSS commutation errors remain in convective, the turbulent diffusion, the viscous diffusion, and the viscous dissipation terms. While the different definitions of the RSS can be considered due to the staggered grid system, we found that with the other definitions induce the residual which is larger than that by the presented scheme.

3.2.2 Existing schemes

The consistent scheme proposed by Suzuki and Kawamura scheme (Suzuki and Kawamura, 1994) reads

$$P_{nn} = -2u'_n\overline{\overline{u'_k}^{x_n}\frac{\delta U_n}{\delta x_k}}^{x_k}, \tag{3.45}$$

$$T_{nn} = \frac{\delta\overline{u'_n}^{x_n}\overline{u'_n}^{x_n}\overline{u'_k}^{x_k}}{\delta x_k}, \tag{3.46}$$

$$\Psi_{nn} = -2\frac{\delta\overline{u'_n}^{x_n}p'}{\delta x_n}, \tag{3.47}$$

$$\Phi_{nn} = -2\overline{p'\frac{\delta u'_n}{\delta x_n}}^{x_n}, \tag{3.48}$$

$$D_{nn} = \frac{1}{\mathrm{Re}}\frac{\delta^2\left(u'_nu'_n\right)}{\delta x_k\delta x_k}, \tag{3.49}$$

$$\varepsilon_{nn} = -\frac{2}{\mathrm{Re}}\overline{\frac{\delta u'_n}{\delta x_k}\frac{\delta u'_n}{\delta x_k}}^{x_k}, \tag{3.50}$$

where the RS is defined on the cell surface. Note that the turbulent diffusion term, Eq. (3.46), does not hold a consistency even on the uniform mesh. The TKE is computed by using arithmetic average at the center of the cell similarly to Eq. (3.36).

They also proposed the consistent scheme for RSS defined at the cell center reads

$$P_{nm} = -\overline{u'_m}^{x_m}\overline{\overline{u'_k}^{x_n}\frac{\delta U_n}{\delta x_k}}^{x_k}{}^{x_n} - \overline{u'_n}^{x_n}\overline{\overline{u'_k}^{x_m}\frac{\delta U_m}{\delta x_k}}^{x_k}{}^{x_m}, \tag{3.51}$$

$$T_{nm} = -\frac{\delta u'_k\overline{\overline{u'_n}^{x_n}}^{x_k}\overline{\overline{u'_m}^{x_m}}^{x_k}}{\delta x_k}, \tag{3.52}$$

$$\Psi_{nm} = -\frac{\delta\overline{\overline{u'_n}^{x_n}}^{x_m}\overline{p'}^{x_m}}{\delta x_m} - \frac{\delta\overline{\overline{u'_m}^{x_m}}^{x_n}\overline{p'}^{x_n}}{\delta x_n}, \tag{3.53}$$

$$\Phi_{nm} = \overline{\overline{p'}^{x_m}\frac{\delta\overline{u'_n}^{x_n}}{\delta x_m}}^{x_m} + \overline{\overline{p'}^{x_n}\frac{\delta\overline{u'_m}^{x_m}}{\delta x_m}}^{x_n}, \tag{3.54}$$

$$D_{nm} = \frac{1}{\mathrm{Re}}\frac{\delta^2\left(\overline{u'_n}^{x_n}\overline{u'_m}^{x_m}\right)}{\delta x_k\delta x_k}, \tag{3.55}$$

$$\varepsilon_{nm} = -\frac{2}{\mathrm{Re}}\overline{\frac{\delta\overline{u'_n}^{x_n}}{\delta x_k}\frac{\delta\overline{u'_m}^{x_m}}{\delta x_k}}^{x_k}. \tag{3.56}$$

The intuitive scheme (Suzuki and Kawamura, 1994) reads

$$P_{nm} = -\overline{u'_n}^{x_n}\overline{u'_k}^{x_k}\overline{\frac{\delta U_m}{\delta x_k}}^{x_k} - \overline{u'_m}^{x_m}\overline{u'_k}^{x_k}\overline{\frac{\delta U_n}{\delta x_k}}^{x_k}, \tag{3.57}$$

$$T_{nm} = \overline{\frac{\delta \overline{u'_n}^{x_n}\overline{u'_m}^{x_m}\overline{u'_k}^{x_k}}{\delta x_k}}^{x_k}, \tag{3.58}$$

$$\Pi_{nm} = -\overline{u'_n}^{x_n}\frac{\Delta p'}{\Delta x_n} - \overline{u'_m}^{x_m}\frac{\Delta p'}{\Delta x_n}, \tag{3.59}$$

$$D_{nm} = \frac{1}{\mathrm{Re}}\frac{\delta^2\left(\overline{u'_n}^{x_n}\overline{u'_m}^{x_m}\right)}{\delta x_k \delta x_k}, \tag{3.60}$$

$$\varepsilon_{nm} = -\frac{2}{\mathrm{Re}}\left(\overline{\frac{\Delta u'_n}{\Delta x_k}}^{x_n}\overline{\frac{\Delta u'_m}{\Delta x_k}}^{x_m}\right), \tag{3.61}$$

where the differential operator is defined, e.g., as

$$\left[\frac{\Delta p'}{\Delta x}\right]_{i,j,k} = \frac{p'_{i+1,j,k} - p'_{i-1,j,k}}{2\Delta x_i}, \tag{3.62}$$

and the RS is defined at the cell center. Because they presented the pressure-oriented terms altogether as the velocity-pressure gradient term, Π_{nn}, we instead used Eq. (3.30) and (3.31) for computation of the pressure diffusion and the pressure strain terms of Fig. 3.5. The TKE is simply defined as the summation of Reynolds normal stresses defined at the center of the cell.

3.2.3 Numerical test

Validity of the proposed scheme is examined in a fully development turbulent channel flow under a constant mass flow rate simulated by using the DNS code of Fukagata et al. (2006). The temporal average is taken in the period of $t^+ = 0$ to $t^+ \approx 4000$ (about 4000 samples), where the subscript of $+$ denotes the wall unit.

Figure 3.5 shows the profiles of different terms in the RS and TKE budgets computed by using the present scheme (top), Suzuki and Kawamura (SK) scheme (Suzuki and Kawamura, 1994) (middle), and the intuitive scheme (Suzuki and Kawamura, 1994) (bottom). SK scheme is the consistent scheme on the uniform and staggered grid system. The intuitive scheme is a scheme with “intuitive” discretization. The symbol represents the budgets computed using the spectral DNS data (Moser et al.,

1999). Due to this flow geometry, the convective term and the gradient of homogeneous directions in Eqs. (3.27)-(3.33) vanish. As is clear from the figure, the budgets computed by the present scheme agrees well with those of the spectral method. The intuitive scheme results in non-negligible residual due to the inconsistency. The residual of the present and the SK schemes are found to be negligibly small in the Reynolds normal stress and the TKE budget (Figs.3.5(a)-(d)). Because the mesh expansion rate in the wall-normal direction used in the present DNS is small, the difference between these two results are small. Figure 3.5(e) shows the RSS budget. The budget computed by the present scheme are in reasonable agreement with that computed by the spectral method. The residual found to be slightly smaller than that by the SK and the intuitive schemes.

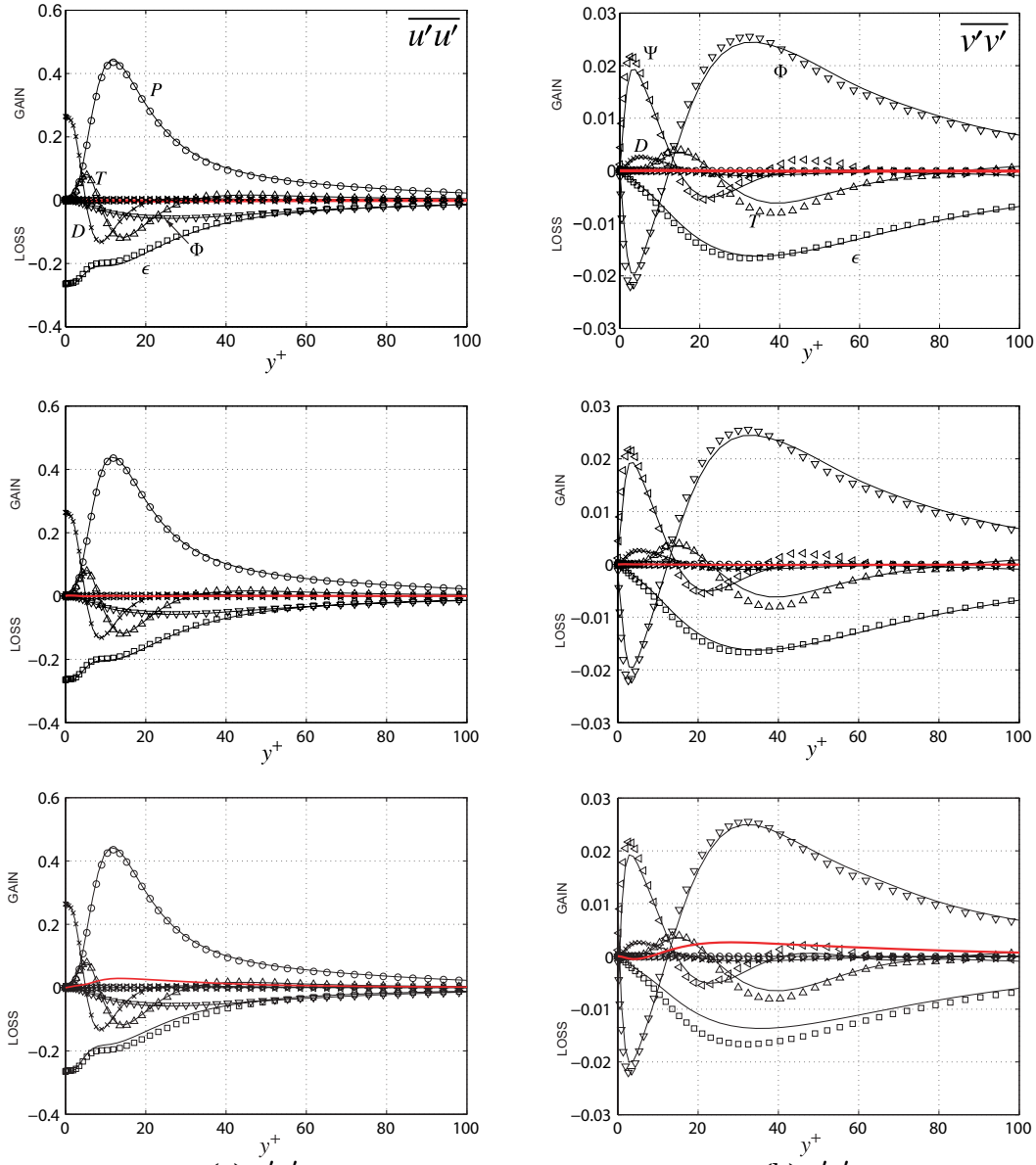

(a) $u'u'$ (b) $v'v'$

Figure 3.5: RS and TKE budgets in fully developed channel flow at $\mathrm{Re}_\tau \approx 180$: P, production; T, turbulent diffusion; Ψ, pressure diffusion; Φ, pressure strain; D, viscous diffusion; ε, viscous dissipation. The solid lines represent: (top) the present scheme; (middle) Suzuki and Kawamura scheme; and (bottom) the intuitive scheme. The symbols represent the results by the spectral method (Moser et al., 1999). The red thick lines and ▷ are the residuals computed by these schemes and the spectral method, respectively.

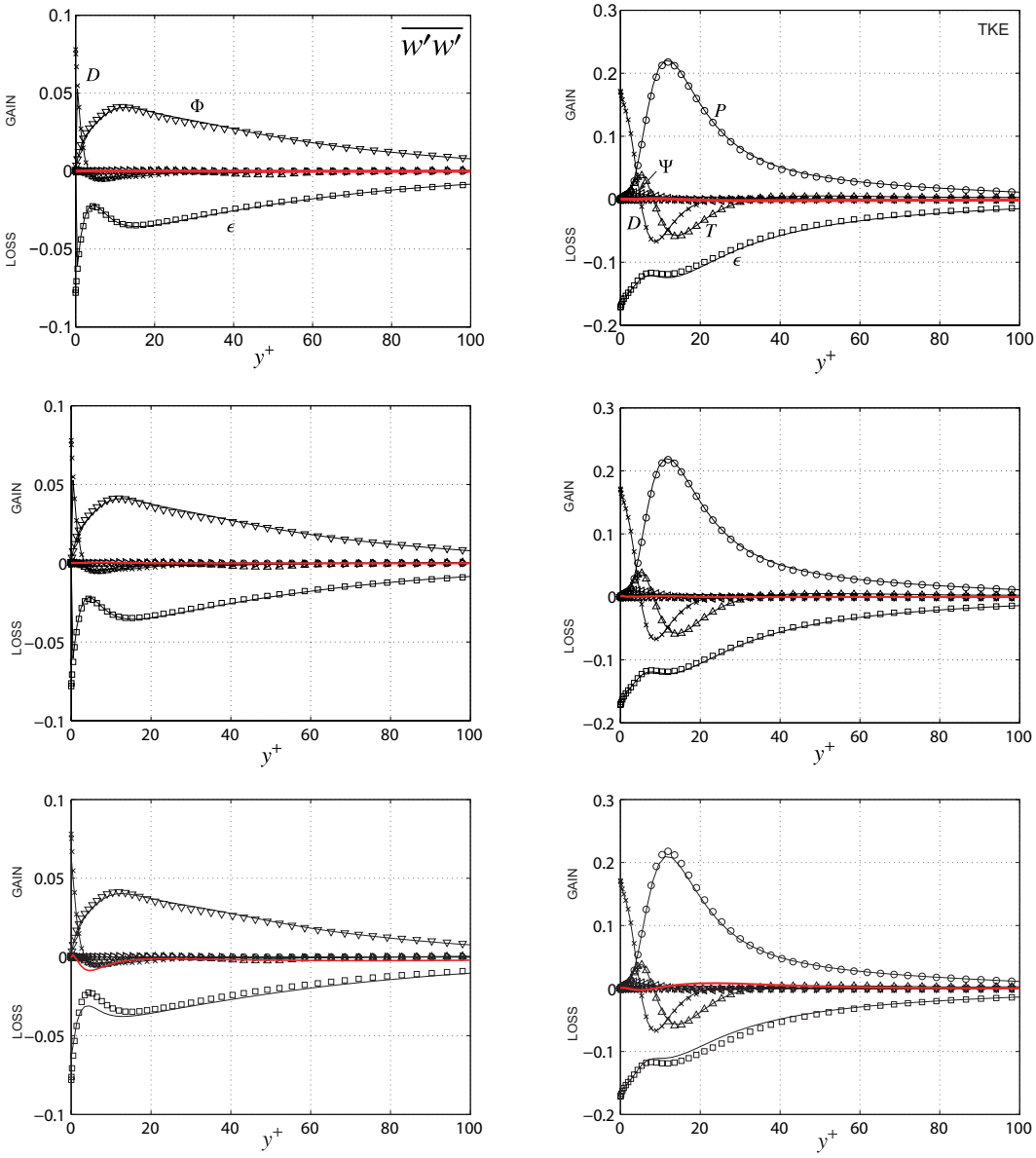

(c) $w'w'$. (d) TKE.

Figure 3.5: Continued.

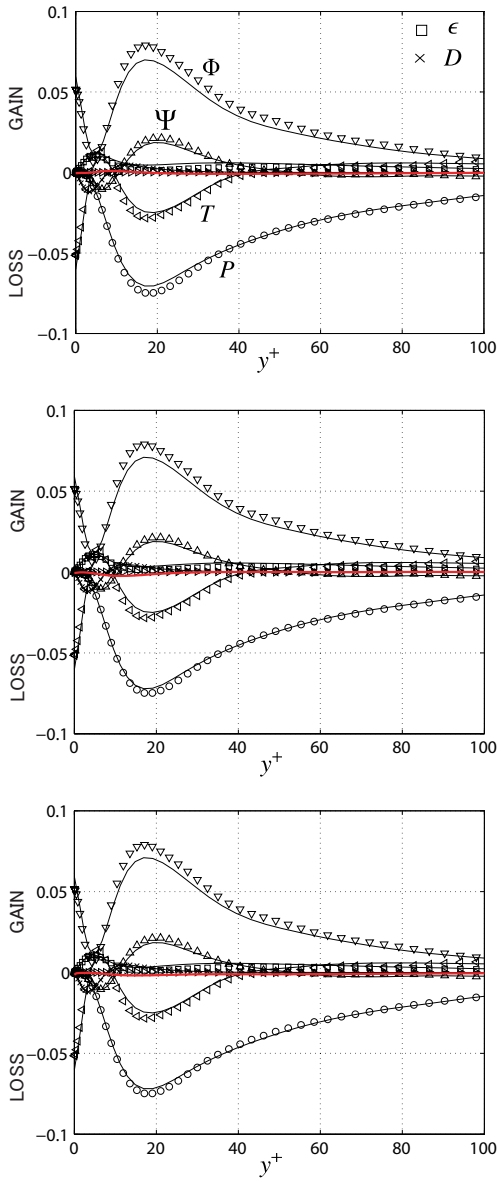

(e) $u'v'$.

Figure 3.5: Continued.

3.2.4 Energy transport in channel flow

Figure 3.6 illustrates the transport RS. The number in red is the percentage of the amount of RS normalized by that of $u'u'$. The numbers in blue and green are also percentages of the each term of the budget of the RS equations for normal and shear components normalized by the production term of $\langle u'u' \rangle_V$ and $\langle -u'v' \rangle_V$, respectively. The budget of RS is computed by using consistent scheme.

The source of energy is the pumping work by the mean pressure gradient, which is fed into the mean streamwise component. Most of the energy of the mean component is converted to the streamwise fluctuating component, $u'u'$, through the production term of $u'u'$ and slightly dissipated. Generally speaking, the magnitude relation of the amount of the Reynolds normal stress (RNS) is $u'_{\mathrm{rms}} > w'_{\mathrm{rms}} > v'_{\mathrm{rms}}$ since the streamwise component only has a production term while the other components are re-distributed from it through the pressure-strain term. Additionally, the wall-normal velocity is strongly damped due to the walls. On the right hand side, the transport of RSS is also shown. The RSS is generated through the production term, which includes $v'v'$. It is disrupted by the pressure-strain term more than the dissipation term. This mechanism is explained by Kasagi et al. (1995) who reveals that the RSS is generated around the QSV. It is disrupted at the high pressure fluctuation region, which is induced by the ejection and sweep motion due to the rotation of QSV. The amount of RSS is related to the production term of $u'u'$. Moreover, it is also connected to the mean pressure gradient through the identity equation for the skin-friction coefficient of Eq. (1.3). Note that the production term and the sum of the pressure-strain and dissipation terms are not perfectly balanced for the RSS because the discretization is not perfectly consistent.

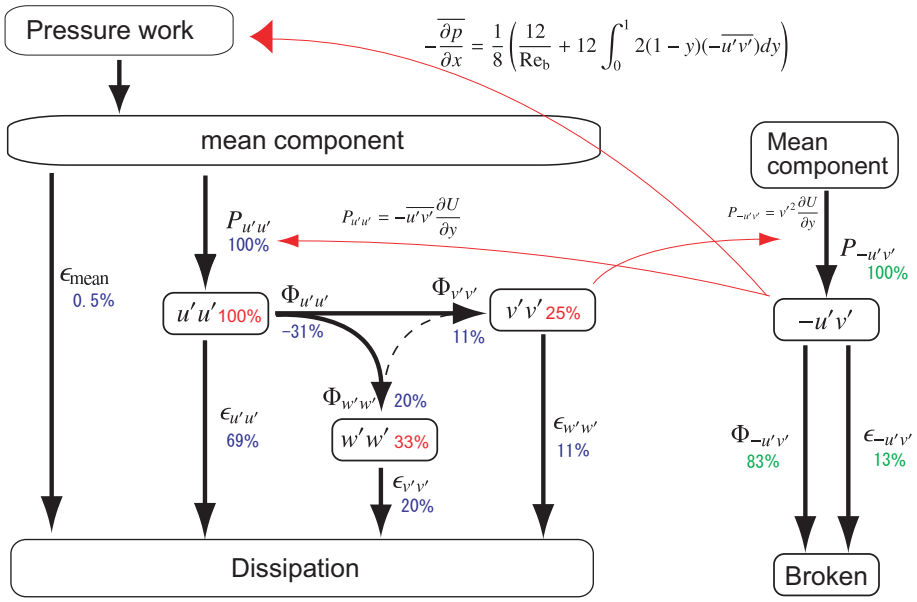

Figure 3.6: Transport of Reynolds Stress in turbulent channel flow at $\mathrm{Re}_\tau \approx 177$. Note that there is no redistribution between $v'v'$ and $w'w'$ components for uncontrolled flow (broken arrow). Red arrows indicate relationships between the Reynolds stress and production term or mean pressure work.

3.3 Traveling wave-like blowing/suction control

Here, we consider the control effect obtained by the traveling wave-like surface blowing/suction in a fully developed channel flow. The form of this control input, the transpiration from the walls distributed sinusoidally, is defined as

$$v(x,0,z,t) = a\sin\left(k(x-ct)\right), \tag{3.63}$$

$$v(x,2,z,t) = -a\sin\left(k(x-ct)\right) \tag{3.64}$$

The wavespeed, c, indicates the wave direction; namely the wave travels to the upstream direction (i.e., opposite direction of the bulk flow) or the downstream directions (i.e., same direction of the bulk flow) when $c<0$ and $c>0$, respectively. The parameters k and a denote the wavenumber and the amplitude of the wave. The amplitude is fixed at $a=0.1$ and only the varicose mode is investigated.

3.3.1 Control performance

The indices of control performance are defined according to Kasagi et al. (2009a): the drag reduction rate, R, is

$$R = \frac{W_{p0}-W_p}{W_{p0}}, \tag{3.65}$$

where the pumping powers and W_p, is defined as

$$W_p = u_b(-\frac{\partial P}{\partial x}) = u_b\frac{C_f}{8}. \tag{3.66}$$

The subscript of "0" denotes the uncontrolled value. The uncontrolled pumping power corresponds to the total dissipation under the constant flow rate. Positive R indicates skin-friction drag reduction rate. The net saving rate (i.e., energy efficiency), S, reads

$$S = \frac{W_{p0}-(W_p+W_a)}{W_{p0}}, \tag{3.67}$$

where W_a is the actuation power calculated by

$$W_a = \frac{1}{L_xL_z}\int_0^{L_x}\int_0^{L_z}\left(\frac{1}{2}v_w^3+p_wv_w\right)dxdz. \tag{3.68}$$

Table 3.3: Grid and domain dependency of the drag reduction rate and the net saving rate under control by the traveling wave-like blowing/suction at $\mathrm{Re}_b = 5600$

$L_x \times L_y \times L_z$	$N_x \times N_y \times N_z$	a	c	k	R	S
$2\pi \times 2 \times 3.5$	$128 \times 96 \times 128$	0.1	-5	1	0.26	0.12
$2\pi \times 2 \times 3.5$	$256 \times 96 \times 128$	0.1	-5	1	0.26	0.14
$2\pi \times 2 \times 3.5$	$128 \times 96 \times 256$	0.1	-5	1	0.25	0.10
$2\pi \times 2 \times 3.5$	$256 \times 96 \times 256$	0.1	-5	1	0.26	0.12
$2\pi \times 2 \times 3.5$	$128 \times 192 \times 128$	0.1	-5	1	0.25	0.12
$4\pi \times 2 \times 3.5$	$256 \times 96 \times 128$	0.1	-5	1	0.26	0.19
$2\pi \times 2 \times 3.5$	$128 \times 96 \times 128$	0.1	4	1	-0.49	-0.84
$2\pi \times 2 \times 3.5$	$256 \times 96 \times 128$	0.1	4	1	-0.49	-0.80
$2\pi \times 2 \times 3.5$	$128 \times 96 \times 256$	0.1	4	1	-0.47	-0.82
$2\pi \times 2 \times 3.5$	$256 \times 96 \times 256$	0.1	4	1	-0.51	-0.83
$2\pi \times 2 \times 3.5$	$128 \times 192 \times 128$	0.1	4	1	-0.47	-0.80
$4\pi \times 2 \times 3.5$	$256 \times 96 \times 128$	0.1	4	1	-0.50	-0.70
$2\pi \times 2 \times 3.5$	$128 \times 96 \times 128$	0.1	-5	4	0.14	-0.22
$2\pi \times 2 \times 3.5$	$256 \times 96 \times 128$	0.1	-5	4	0.12	-0.24
$2\pi \times 2 \times 3.5$	$128 \times 96 \times 128$	0.1	-5	8	0.07	-0.51
$2\pi \times 2 \times 3.5$	$256 \times 96 \times 128$	0.1	-5	8	0.03	-0.56
$2\pi \times 2 \times 3.5$	$128 \times 96 \times 128$	0.1	-5	16	0.02	-0.88
$2\pi \times 2 \times 3.5$	$256 \times 96 \times 128$	0.1	-5	16	0.05	-0.81

Positive efficiency is obtained when $S > 0$. This definition allows $W_a < 0$ if $v_w < 0$ or $p_w v_w < 0$, which means the control actuator can recover the power while a realized actuator can not.

Verification is made by changing the domain size and the number of grids, as tabulated in Table 3.3: the number of grid is doubled in each direction and the streamwise length is also doubled. For $c = -5$ or $c = 4$ at $k = 1$, major dependency on them is not found. As increasing wavenumber at $c = -5$, a slight difference is found in R and S, while it is tiny value compared to that of $k = 1.0$.

Figure 3.7 shows the time trace of skin-friction drag, D, for different wavespeeds

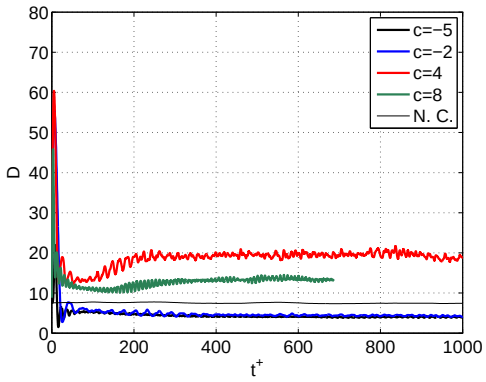

Figure 3.7: Time trace of skin-friction at $k = 0.5$ and $a = 0.1$ for different wavespeeds.

at $k = 0.5$ and $a = 0.1$, where D is defined as

$$D = \frac{4}{3\mathrm{Re_b}} \left(-\frac{dP}{dx} \right). \tag{3.69}$$

According this definition, the laminar value is $D_{lam} = 2$. At $t^+ < 30$, the skin-friction drag rapidly increases for all wavespeeds. It is because the large scale control input, i.e., traveling wave-like blowing/suction, breaks the coherent structure and the energy are more dissipated. For the upstream traveling wave, the skin-friction achieves the steady state at $t^+ > 600$. For the downstream traveling wave, the skin-friction drag gradually decreases after the initial large peak and it achieves the steady state at $t^+ > 300$.

Figure 3.8 shows the drag reduction and net saving rates as a function of the wavespeed for different wavenumbers ($k = 0.5$ and $k = 1.0$) at $a = 0.1$. Drag reduction (i.e., $R > 0$) is obtained when the wave travels to the upstream direction (i.e., $c < 0$): R for $k = 0.5$ is larger than that for $k = 1.0$. While the downstream traveling wave increases the drag, the drag increment is similar for the larger wavespeed. Positive net saving rate (i.e., $S > 0$) is also obtained by the upstream traveling wave. The optimal wavespeed is $c = -2$ in this figure. The positive net saving rate is found at $c = 0$ and $k = 0.5$ while $R < 0$, because of $W_a < 0$.

Figure 3.9 shows the RSS profile for the upstream and downstream traveling wave at $k = 0.5$. Decrease of the RSS, which is lower than that of uncontrolled case, is observed at $c < 0$. Moreover, the negative RSS is found in the region near the wall

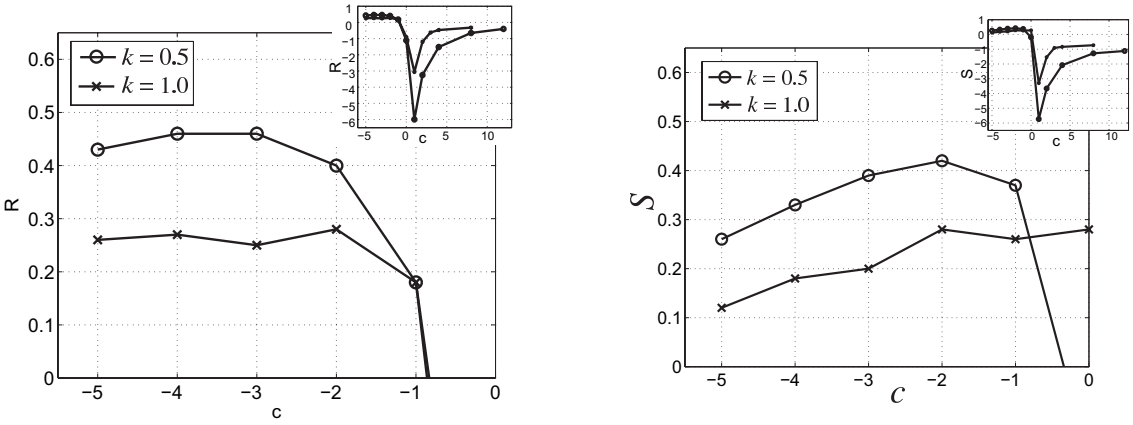

Figure 3.8: Drag reduction rate (R, left) and net saving rate (S, right) as a function of wavespeed at $a = 0.1$ and $\mathrm{Re}_{\tau 0} \approx 177$.

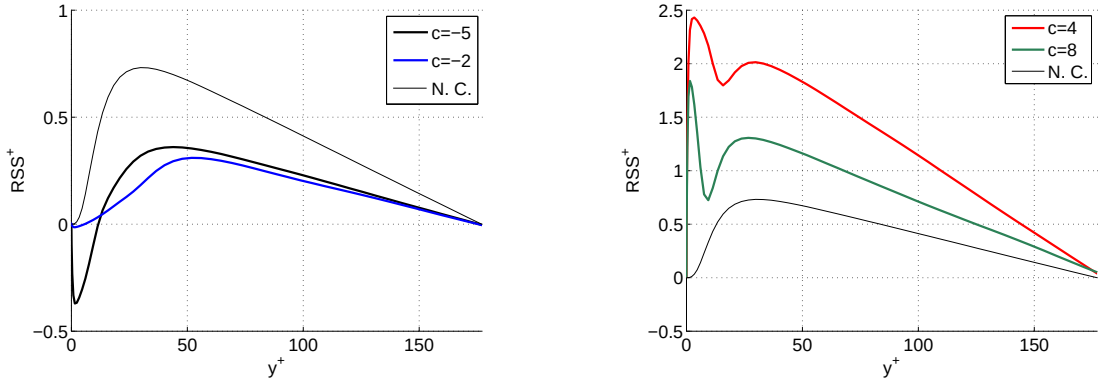

Figure 3.9: RSS profile for the upstream (left) and downstream (right) traveling wave at $a = 0.1$ and $k = 0.5$.

at $c = -5$. On the other hand, for the downstream traveling wave, the RSS increases significantly, which leads to the drag increase. The double peaks are observed in very near wall-region and $y^+ \approx 25$

Figure 3.10 visualizes the vortical structure at $a = 0.1$, $c = -5$, and $k = 0.5$. The top figure shows the isosurface of $Q^+ = -0.03$, which is the same value of that of the uncontrolled flow as shown in Fig. 1.1. The QSV is found to disappear. The bottom figure displays the isosurface of $Q^+ = -0.01$, which visualizes QSV more clearly than $Q^+ = -0.03$. This figure implies that the QSV is sucked into the suction part of the wave and moved from the wall above the blowing part. Hence, the region where the

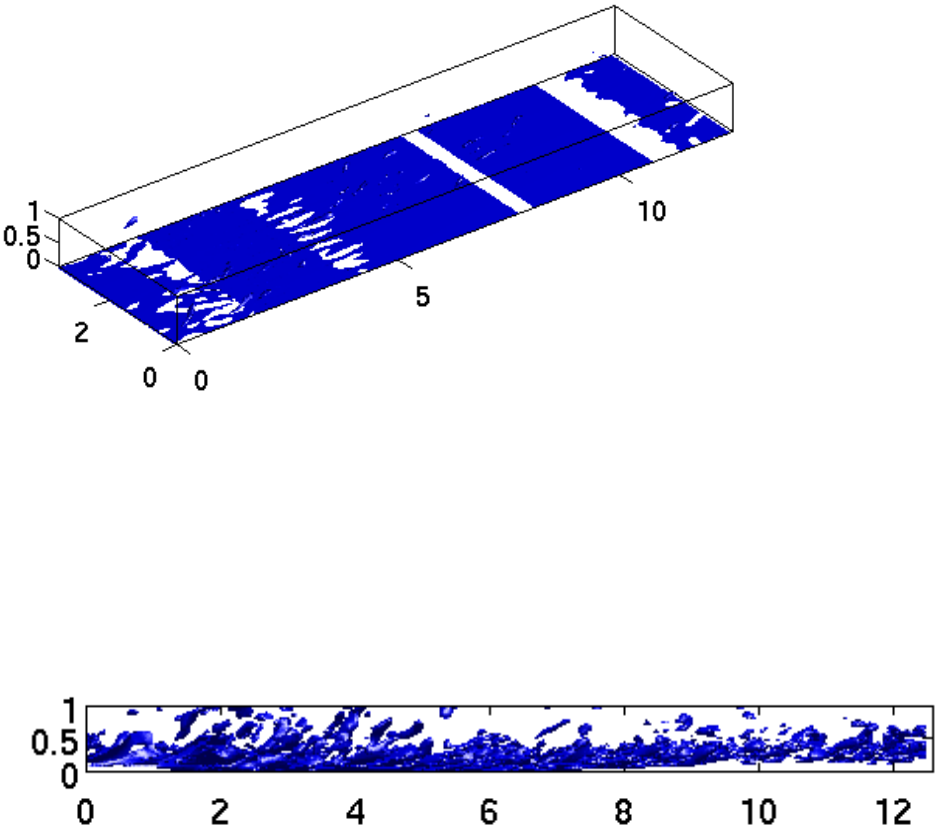

Figure 3.10: Visualization of vortical structure at $c = -5$ and $k = 0.5$ (top, $Q^+ = -0.03$; bottom, $Q^+ = -0.01$).

QSV disappears is observed.

Figure 3.11 shows the instantaneous distribution of the RSS in $x-y$ planes at $z =$

$L_z/2$ for $c=-2$, $k=0.5$, and $a=0.1$. In order to exclude the periodic component of the velocity, the velocity fluctuation is defined as

$$f'''(x,y,z,t) = f(x,y,z,t) - \frac{1}{L_z}\int_0^{L_z} f(x,y,z,t)dz. \tag{3.70}$$

This figure shows the distribution of $-u'''v'''$ with a velocity vector for different time. As the time advances, decrease of the RSS is observed. In addition, the streamwise velocity is found to be accelerated above the blowing part of the wave, which indicates the so-called pumping effect (Hoepffner and Fukagata, 2009).

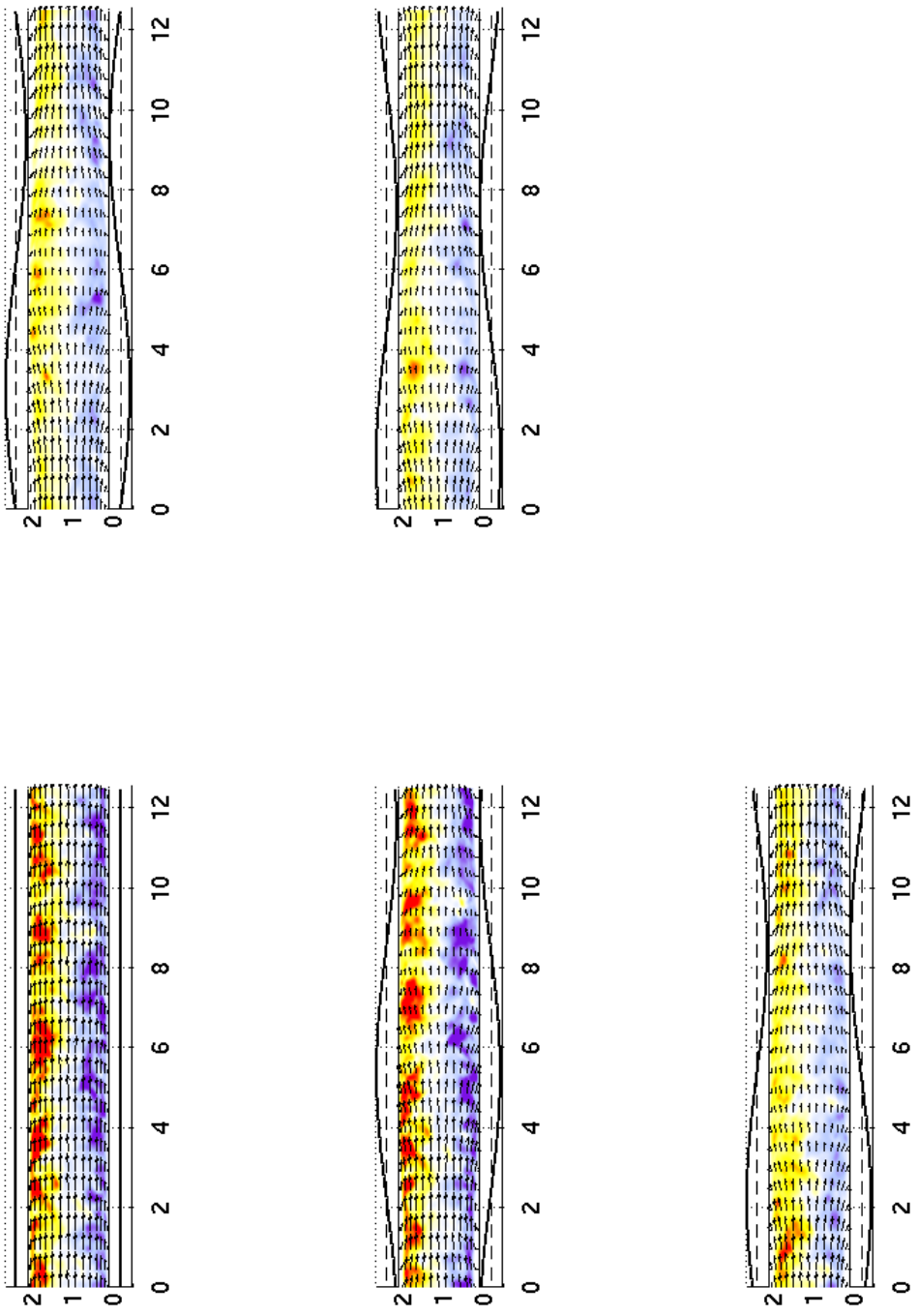

Figure 3.11: Instantaneous filed of $-u'''v'''$ controlled by the upstream traveling wave ($c = -2$, $k = 0.5$). In the left column: top, $t^+ \approx 0$; middle, $t^+ \approx 10$; bottom, $t^+ \approx 195$. In the right column: top, $t^+ \approx 615$; middle, $t^+ \approx 1000$.

3.3.2 Comparison with existing control

In order to confirm the advantage of the present control, the control effect by different control scheme is shown together: the opposition control (Choi et al., 1994) and the suboptimal control (Lee et al., 1998). Concepts of these control schemes are sketched in Fig. 3.12: a QSV is canceled by a transpiration from the wall, which is determined based on the detected velocity. The *v*-control, a.k.a. the opposition control, proposed by Choi et al. (1994) is a typical and most simple feedback control for the skin-friction drag reduction. Namely, the wall-normal velocity on the wall is input to cancel the downward and upward rushes that are generated by the rotation of the QSV. The wall-normal velocity is detected at a sensing location, y_d^+; thus, the mathematical form of the *v*-control reads

$$v_w = -v(y^+ = y_d^+). \tag{3.71}$$

The optimal sensing location is known to be $y_d^+ \approx 15$ at $\mathrm{Re}_{\tau 0} \approx 177$ (Hammond et al., 1998).

On the other hand, the concept of the suboptimal control is illustrated in Fig. 3.12. Lee et al. (1998) determined the control law for the wall transpiration, which minimizes the wall-normal velocity gradient of the spanwise velocity that is enhanced by the QSV. Thus, a cost function, J, is set as

$$J = \frac{1}{2S\Delta t}\int_S\int_{\Delta t}^{y+\Delta t} (v_w)^2\, dtdS - \frac{1}{2S\Delta t}\int_S\int_{\Delta t}^{y+\Delta t} \left(\left.\frac{\partial w}{\partial y}\right|_w\right)^2 dtdS, \tag{3.72}$$

where S denotes the surface of a channel and Δt is a short time duration. The first term of the RHS of abovementioned equation represents a cost of control input and the second term represents the spanwise wall shear stress. With this cost function , the wall-normal velocity as a control input is mathematically derived in the form of the Fourier coefficient, $\widehat{v}_w$, as (Lee et al., 1998)

$$\widehat{v}_w = C\frac{ik_z}{k}\left.\widehat{\frac{\partial w}{\partial y}}\right|_w, \tag{3.73}$$

where k_x and k_z are the wavenumbers in the streamwise and spanwise directions, respectively, and $k = \sqrt{k_x^2 + k_z^2}$. The sole parameter, C , is set to $C = 0.01$. This control law indicates that the control input is determined based on the spanwise wall shear

stress which is the measurable data. Since the major drawback of the opposition control is the need of sensors in the flow, the suboptimal control input is more practical than the opposition control in that sense.

Figure 3.13 shows the time history of the normalized skin-friction coefficient under the upstream traveling wave-like blowing/suction, the *v*-control, and the suboptimal control at $\mathrm{Re}_{\tau 0} \approx 177$. The parameters of these control are: the traveling wave, $a = 0.1$, $c = -5$, and $k = 0.5$; the *v*-control, $y_d^+ \approx 15$; the suboptimal control, $C = 0.01$. The skin-friction coefficient is found to be modified at $0 < t^+ < 1000$, we call this sequence as "transitional stage". In this transitional stage for the upstream traveling wave-like control, the skin-friction drag rapidly and significantly increases. It is because the traveling wave-like control breaks the coherent structure and the turbulent kinetic energy is dissipated significantly. The skin-friction drag, however, subsequently decreases to approach the steady state. While the skin-friction slightly increases at the early transitional stage for the *v*-control, it gradually decreases after that. For the suboptimal control, the skin-friction is found to gradually decreases in this transition stage. When the drag reaches to the steady state, the maximum drag reduction is obtained by the upstream traveling wave.

Figure 3.13 also shows that the RSS for these control schemes. Only for the traveling wave control, the RSS is found to be negative in the region near the wall, which induces the significant drag reduction. It is also found to be sustained below the uncontrolled RSS in the far-wall region. For the *v*-control and the suboptimal control, however, despite the decrease of the RSS, it is sustained to be positive. In these controls, the virtual wall appears at $y^+ \approx 8$, where the exchange of momentum between the near-wall region and the far-wall region is prevented, as pointed out by Hammond et al. (1998).

Figure 3.12: Schematics of control schemes: left, *v*-control (Choi et al., 1994); right, suboptimal control (Lee et al., 1998).

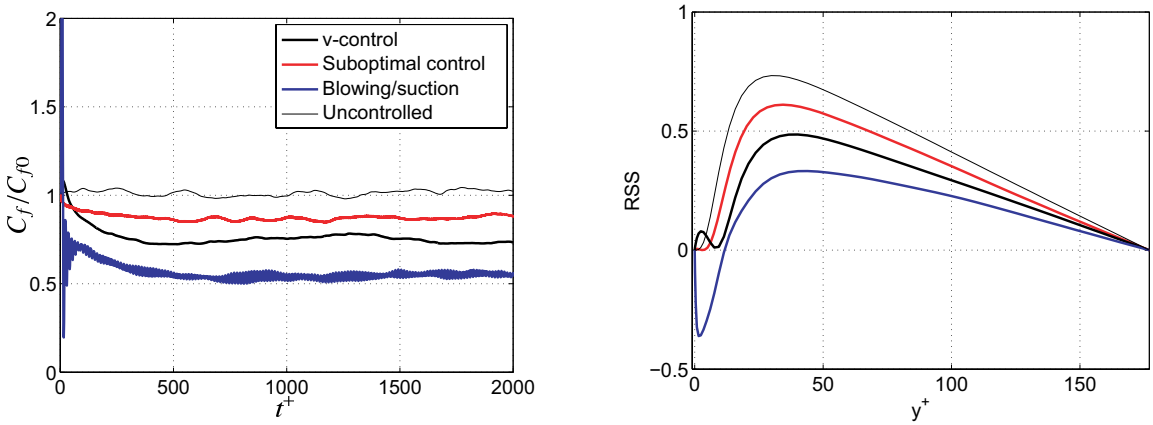

Figure 3.13: Left, time history of the skin-friction coefficient normalized by the uncontrolled value at $\mathrm{Re}_{\tau 0} \approx 177$. Right, RSS profile in wall units. Color indicates different control schemes: blue line, traveling wave-like blowing/suction control ($a = 0.1$, $c = -5$, and $k = 0.5$); black line, *v*-control ($y_d^+ \approx 15$); red line, suboptimal control ($C = 0.01$); thin line, uncontrolled flow.

3.3.3 Drag reduction mechanism

Due to the traveling wave-like control input, the flow is expected to have the scale that depends on that of the traveling wave. Linear analysis presented in Chap. 2 shows that the periodic velocity induces the negative-RSS which sustains the sub-laminar skin-friction drag. Therefore the periodic component is focused in also this turbulent flow. Here, three component decomposition (Hussain and Reynolds, 1970) is employed in order to distinguish the contributions from this periodic component. The definition of this three component decomposition is

$$f = \overline{f} + \widetilde{f} + f'', \tag{3.74}$$

where the bar, the tilde, and the double-prime denote the mean, spatially periodic in the streamwise direction, and random components, respectively. The sum of $\widetilde{f}$ and f'' is equivalent to f'. The averaging procedures are expressed as

$$\langle f \rangle (\phi_x, y) = \frac{1}{L_z T} \int_0^{L_z} \int_0^T \left(\lim_{N\to\infty} \frac{1}{N} \sum_{n=0}^{N} f(\phi_x + 2\pi n, y, z, t) \right) dt dz, \tag{3.75}$$

$$\overline{f}(y) = \frac{1}{2\pi} \int_0^{2\pi} \langle f \rangle \, d\phi_x, \tag{3.76}$$

$$\widetilde{f}(\phi_x, y) = \langle f \rangle - \overline{f}, \tag{3.77}$$

where ϕ_x is the phase of the wave in the streamwise direction, defined in $0 < \phi_x < 2\pi$. In the following, the spatially periodic component is referred as a "periodic " component for simplicity.

According to the abovementioned decomposition, the RNS can be decomposed as

$$\overline{u'u'} = \overline{\widetilde{u}\widetilde{u}} + \overline{u''u''}. \tag{3.78}$$

The RSS can be also decomposed as

$$-\overline{u'v'} = -\overline{\widetilde{u}\widetilde{v}} - \overline{u''v''}. \tag{3.79}$$

The first and second terms at the RHS are labeled as "periodic-RSS" and "random-RSS", respectively. Here, the correlation between the periodic and random components

are supposed to be zero, i.e., $\overline{\widetilde{f}\widetilde{g}''} = 0$. By substituting Eq. (3.79) into Eq. (1.3), the skin-friction coefficient can be rewritten as (Yakeno et al., 2010)

$$C_f = \frac{12}{\mathrm{Re}_b} + \underbrace{12\int_0^1 2(1-y)\left(-\overline{\widetilde{u}\widetilde{v}}\right)dy}_{C_{f,\ \mathrm{periodic}}} + \underbrace{12\int_0^1 2(1-y)\left(-\overline{u''v''}\right)dy}_{C_{f,\ \mathrm{random}}}. \tag{3.80}$$

Namely, the turbulent contribution can be divided into those from the periodic-RSS and the random-RSS.

Figure 3.14 depicts the profile of the rms value of the random velocity component, u''_{rms} (labeled as "random-rms value") and the RSS profile at $c = -5$ and $k = 0.5$, which decreases the skin-friction by 40% compared to the uncontrolled case. As shown in Fig. 3.14(a), all the random-rms values are found to decrease compared to "total-rms value" of the uncontrolled flow (viz., u'_{rms}), which indicates decrease of the turbulent kinetic energy. As seen before, the total-RSS under this control is negative in the region near the wall and decreases far from the wall. According to three component decomposition, this total-RSS profile consists of the negative periodic-RSS and the decreased random-RSS as shown in Fig. 3.14. The periodic-RSS is negative in the region near the wall and zero far from the wall, which is similar trend to that obtained by the linear analysis in the previous chapter; so this profile is expected to be explained by the phase relationship (discussed later). The random-RSS is found to be positive in whole channel because this component reflects the motion of the QSV, which always works to make the RSS positive.

Once the skin-friction drag is reduced by the negative periodic-RSS, the mean pressure gradient is also reduced due to the constraint of constant flow rate. Accordingly, the energy supply from the pressure work decreases and the random-RSS decreases due to reduced production of random velocity components. We refer this mechanism as "indirect effect".

Figure 3.15 illustrates the distribution of the periodic- and the random-velocities. For the periodic component, the cellular structures akin to those observed in laminar flow shown in Fig. 2.12 are found. Especially, the zoom-up view of the distribution of the near-wall $\widetilde{u}\widetilde{v}$ reveals that the non-zero $\widetilde{u}\widetilde{v}$ is found due to the subtle phase shift of $\widetilde{u}$. For the random components, the fluctuationless region is found to appear in the region near the wall.

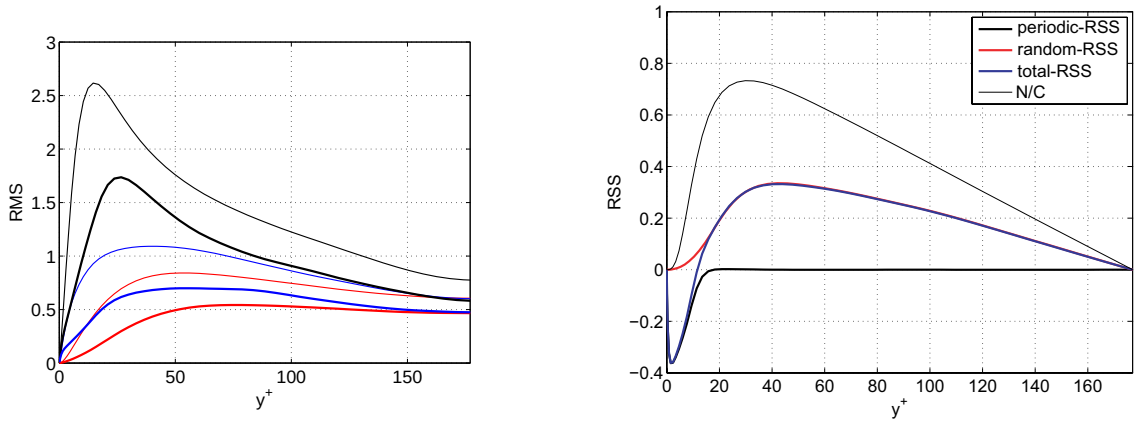

Figure 3.14: Left, the rms value of the random components of the velocities; right, the profile of the RSS at $a = 0.1$, $c = -5$, and $k = 0.5$.

The streamlines of the mean and periodic velocities are shown in Fig. 3.16. The blue line indicates the streamline of the mean velocity. Due to the blowing/suction from the wall, the mean flow is induced in the region from the blowing to the suction parts of the wave, whereas it is expanded in the region from the suction to the blowing. On the other hand, the black line denotes the injected and sucked flow motion by the blowing/suction from the wall. The reason of the existing a fluctuationless region (i.e., no random-velocity component area) confirmed in Fig. 3.15 is that the laminar flow is injected from the blowing part of the wave.

The quadrant analysis of RSS is known to provide the detailed information of the contribution to the RSS (Kim et al., 1987). This analysis is applied for the periodic-RSS, i.e.,

$$Q1 \quad : \quad \widetilde{u} > 0, \widetilde{v} > 0, \tag{3.81}$$

$$Q2 \quad : \quad \widetilde{u} < 0, \widetilde{v} > 0, \tag{3.82}$$

$$Q3 \quad : \quad \widetilde{u} < 0, \widetilde{v} < 0, \tag{3.83}$$

$$Q4 \quad : \quad \widetilde{u} > 0, \widetilde{v} < 0. \tag{3.84}$$

$Q2$ and $Q4$ contribute to the increase of RSS, whereas $Q1$ and $Q3$ contribute to the decrease of that. Generally, in the quadrant analysis for the random-components; $Q2$ and $Q4$ events indicate so-called ejection and sweep motions, respectively. Figure 3.17

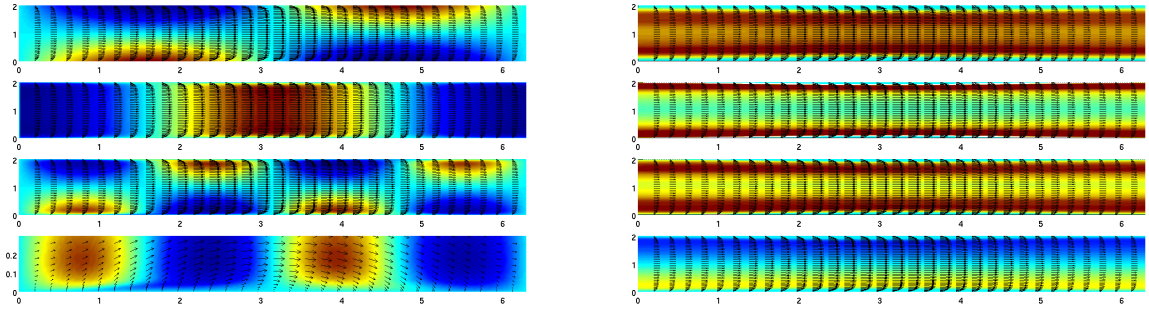

Figure 3.15: Distributions of the periodic and the random-velocities at $c = -5$, $k = 0.5$, and $a = 0.1$. Left column shows the periodic components: top, $\widetilde{v}$; second, $\widetilde{u}$; third, $-\widetilde{u}\widetilde{v}$; bottom, the zoom-up view of $-\widetilde{u}\widetilde{v}$. Right column shows the random components: top, $u''u''$; second, $v''v''$; third, $w''w''$; bottom, $-u''v''$.

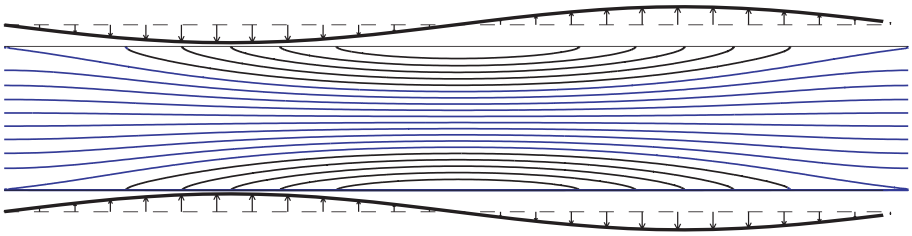

Figure 3.16: Streamlines of mean and periodic velocities at $c = -5$ and $k = 0.5$: the blue and the black lines indicate the streamline due to the mean and the blowing/suction.

shows that the sum of the periodic-$Q1$ and $Q3$ almost balances to that of the periodic-$Q2$ and $Q4$. However, the negative contribution is slightly larger than the positive one in the region near the wall.

According to the phase analysis by Chap. 2, the RSS in a laminar flow is generated by a non-quadrature between the streamwise and wall-normal velocities fluctuations. In order to apply this analysis for the turbulent flow, the Fourier transform is employed,

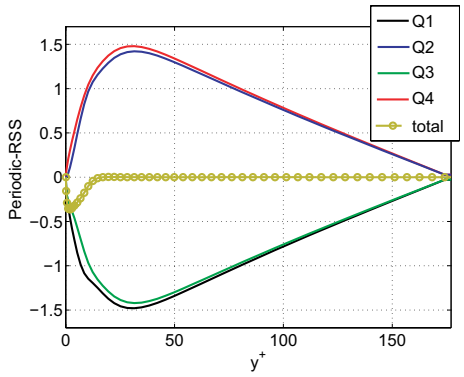

Figure 3.17: Quadrant decomposed periodic-RSS at $a = 0.1$, $c = -5.0$, and $k = 0.5$.

which is defined as

$$f = \sum_{k'=0}^{N} \widehat{f}_{k'} e^{-ik'x}, \tag{3.85}$$

where the hat denotes the Fourier coefficient. The phase difference between the Fourier coefficients of the streamwise and wall-normal velocities is

$$\phi = \arg\widehat{\widehat{u}}_k - \arg\widehat{\widehat{v}}_k + \frac{\pi}{2}, \tag{3.86}$$

where the wavenumber of the Fourier coefficients is chosen at $k' = k$, which corresponds to the input wavenumber of the traveling wave.

Figure 3.18 shows the phase profile of the Fourier coefficient, $\widehat{u}'_k$, $\widehat{v}'_k$, and the difference of them, ϕ. The non-quadrature, $\phi \neq 0$, appears in the region near the wall, which contributes to generation of the negative RSS according Eq. (2.19). This non-quadrature due to the phase shift of the streamwise component has the same trend as that observed in the analysis of the laminar flow.

The control effect by the downstream traveling wave also is investigated at $c = 4$ and $k = 0.5$. Figure 3.19(a) shows the profiles of the "total-", "periodic-", and "random-" RSSs. The total-RSS remarkably increases due to the increasing random- and periodic-RSS, which produces large skin-friction drag. The periodic-RSS increases in the region near the wall and it is slightly negative around $y^+ \approx 20$ while it is zero far from the wall. The random-RSS is found to increase, which indicates enhancement of the QSV by the control. The phase analysis for the periodic component

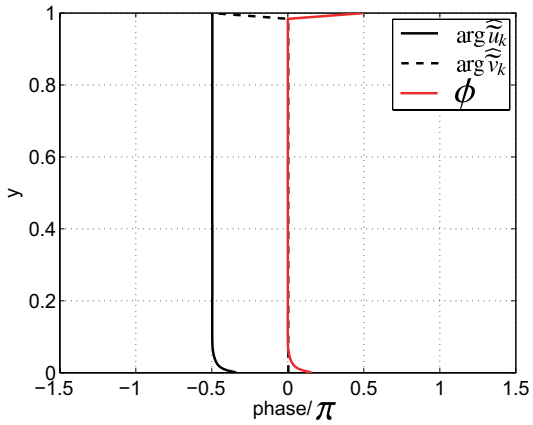

Figure 3.18: Profiles of phases of the Fourier coefficients at $k' = k$ in drag reducing case by the upstream traveling wave in turbulent flow ($a = 0.1$, $k = 0.5$ and $c = -5$).

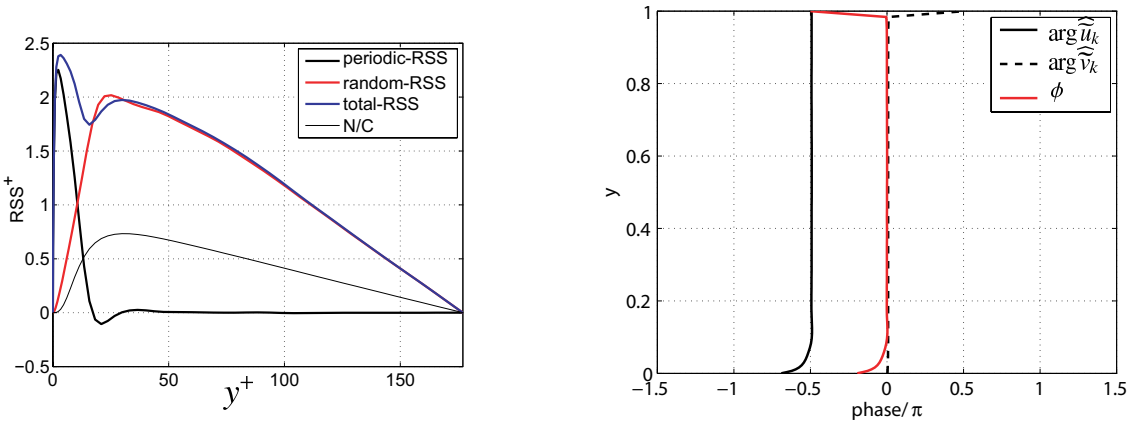

Figure 3.19: Left, RSS profile compared with the uncontrolled channel flow; right, phase profile for the periodic component for the downstream traveling wave at $a = 0.1$, $c = 4$, and $k = 0.5$.

is also displayed in Fig. 3.19. The negative phase difference, which contributes to the increase of skin-friction drag, is found in the region near the wall because $u'_{k=k'}$ has a phase lag (i.e., negative phase shift). This phenomena corresponds to the observation in Chap. 2.

Figure 3.20 displays the distribution of the periodic and random-velocities and the products. For the periodic-component, the cellular structure is also observed. Because

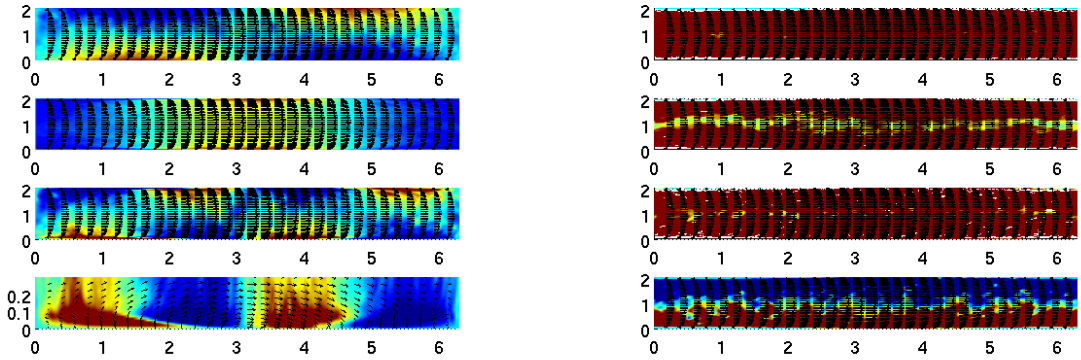

Figure 3.20: Left column is the distributions of the periodic velocities: top, $\widetilde{v}$; second, $\widetilde{u}$; third, $-\widetilde{u}\widetilde{v}$; bottom, the zoom-up view of $-\widetilde{u}\widetilde{v}$. Right column is the distribution of the random velocity components: top, $u''u''$; second, $v''v''$; third, $w''w''$; bottom, $-u''v''$. The parameters are $c = 4$, $k = 0.5$, and $a = 0.1$.

the pumping effect works to drive the flow to the upstream direction, the backward flow is found in the region near the wall. It is also found that the random-component increases significantly.

Figure 3.21 gives an explanation of the instability of the flow by the upstream traveling wave. Due to the pumping effect (Hoepffner and Fukagata, 2009), backward flow is induced in the region near the wall. Therefore, an inflection point appears in the mean streamwise velocity, which triggers instability of the flow. In other word, the gradient of the mean velocity, which is included in the production term, increases.

In order to analyze the transport of the energy among three components, the transport equation of the TKE budget is considered here. In the same manner as the three component decomposition, the transport equation of the periodic-TKE, $\widetilde{k} = \frac{1}{2}\widetilde{u}_i\widetilde{u}_i$, reads

$$0 = \widetilde{P}^{mp}_{\widetilde{k}} - \widetilde{P}^{pr}_{\widetilde{k}} - \widetilde{\varepsilon}_{\widetilde{k}} + \widetilde{d}_{\widetilde{k}}, \tag{3.87}$$

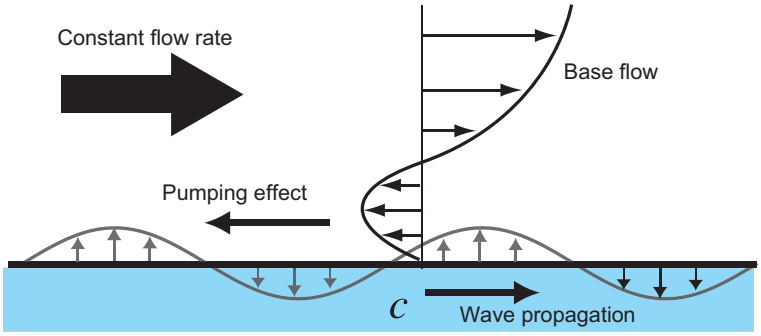

Figure 3.21: Schematic of the velocity profile when the wave travels in the downstream direction.

and that of the random-TKE, $k'' = \frac{1}{2}u_i''u_i''$, reads

$$0 = P_{k''}^{mr} + P_{k''}^{pr} - \varepsilon_{k''} + d_{k''}, \tag{3.88}$$

where P, ε, and d denote the production, dissipation, and diffusion terms, respectively. Three production terms appear in the above equations:

$$P^{mp} = -\overline{\widetilde{u}\widetilde{v}\frac{\partial \overline{u}}{\partial y}}, \tag{3.89}$$

$$P^{pr} = -\overline{u''v''\frac{\partial \widetilde{u}}{\partial y}}, \tag{3.90}$$

$$P^{mr} = -\overline{u'v'}\frac{\partial \overline{u}}{\partial y}, \tag{3.91}$$

where P^{mp}, P^{pr}, and P^{mr} indicate the TKE transfer from the mean to periodic components, from the periodic to random components, and from the mean to random components, respectively. Note that only non-zero term is displayed here when averaged in the homogeneous directions.

Figure 3.22 shows the profiles of these production terms under the control of traveling wave-like blowing/suction together with that of the uncontrolled flow. For the upstream traveling wave, P^{pr} and P^{mr} are found to remarkably decrease while P^{mp} is largely negative in the region near the wall. The transfer of the TKE from the periodic to random components is suppressed. Moreover, the negative P^{mp} implies the

backward transfer of the TKE from the periodic to random components. For the downstream traveling wave, all the production terms are found to be positive and increase; namely the random-TKE is remarkably increased. The schematic of this energy transfer is shown in Fig. 3.23: the direction of energy transfer from the mean to periodic components is opposed to each other.

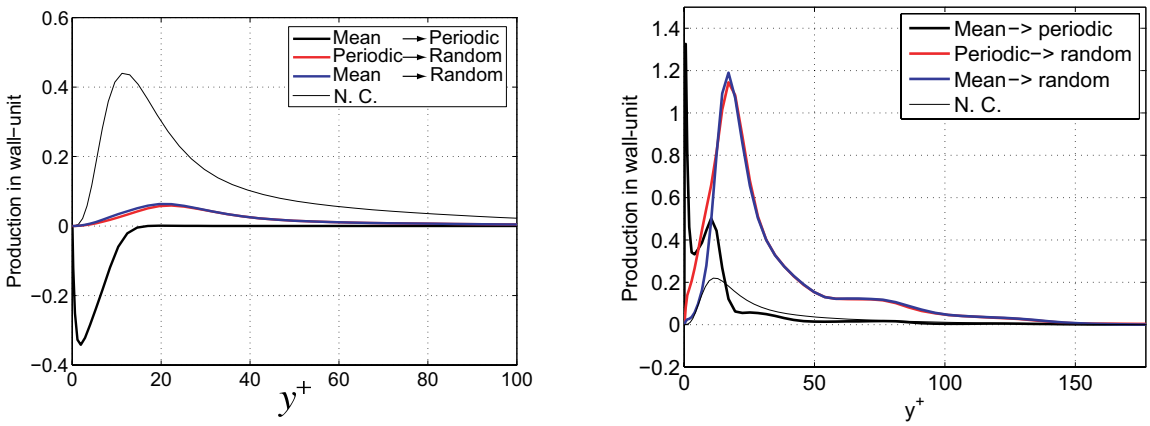

Figure 3.22: Production terms decomposed into three components ($a = 0.1$): left, the upstream traveling wave at $c = -5$ and $k = 0.5$; right, the downstream traveling wave at $c = 4$ and $k = 0.5$.

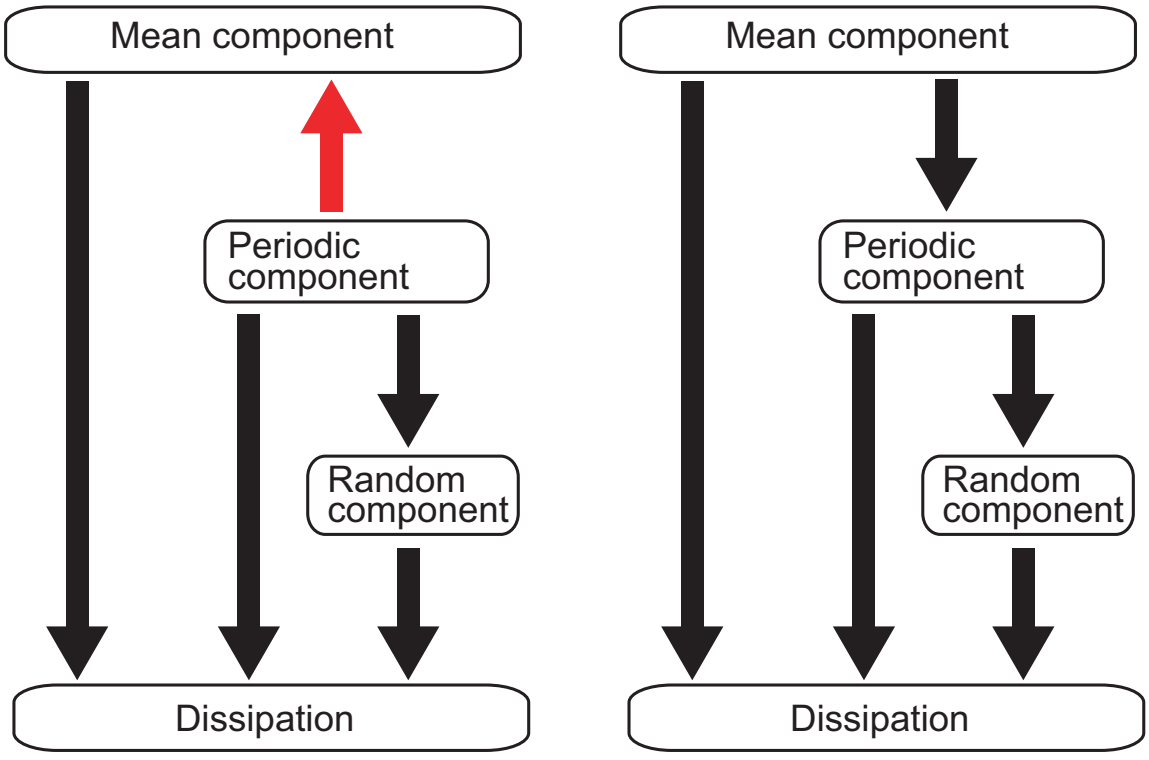

Figure 3.23: Schematic of the energy chart for the upstream traveling wave (left) and the downstream traveling wave (right).

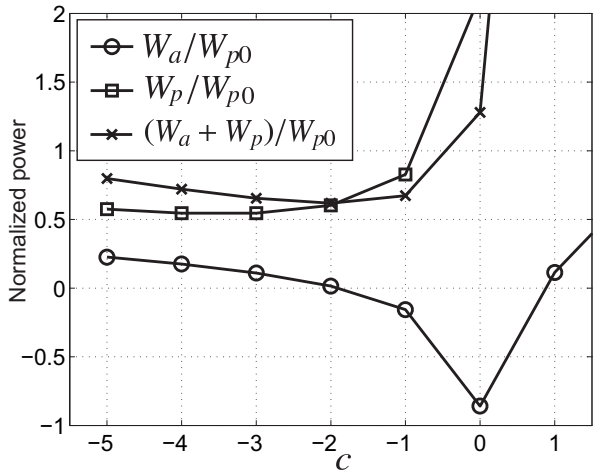

Figure 3.24: Actuation and pumping power normalized by the pumping power of the uncontrolled flow. The black and red lines indicate the actuation and pumping works, respectively. The parameters are $k = 0.5$ and $a = 0.1$.

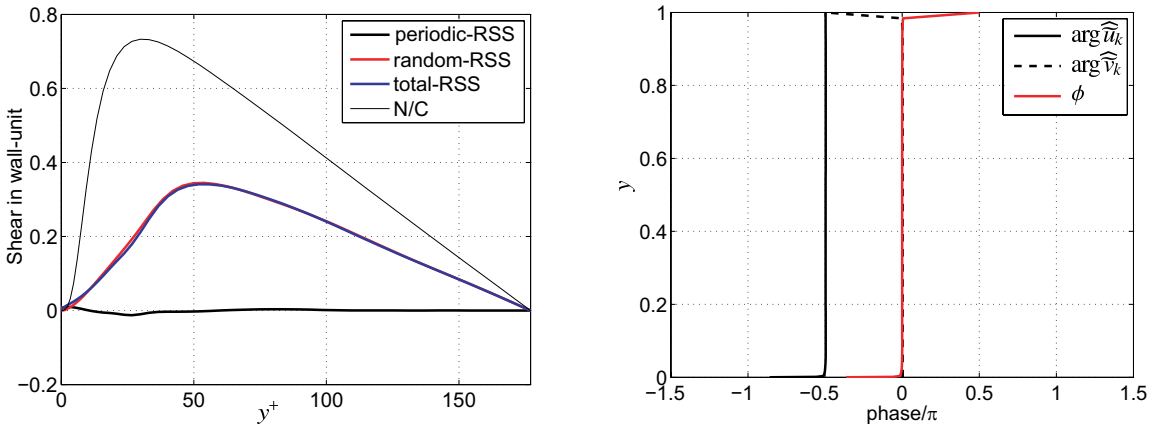

Figure 3.25: Left, RSS profile; right, phase profile for the periodic component for the upstream traveling wave at $a = 0.1$, $c = -2$, and $k = 0.5$.

The skin-friction drag reduction due to the decrease of the periodic-RSS can be explained by the detailed phase analysis. Here, we consider the flow controlled by the upstream traveling wave at $c = -2.0$ which induces the maximum net saving rate at $k = 0.5$.

The net saving rate is calculated by the actuation and pumping powers as defined in Eq. (3.67). Figure 3.24 shows the actuation and pumping powers normalized by the

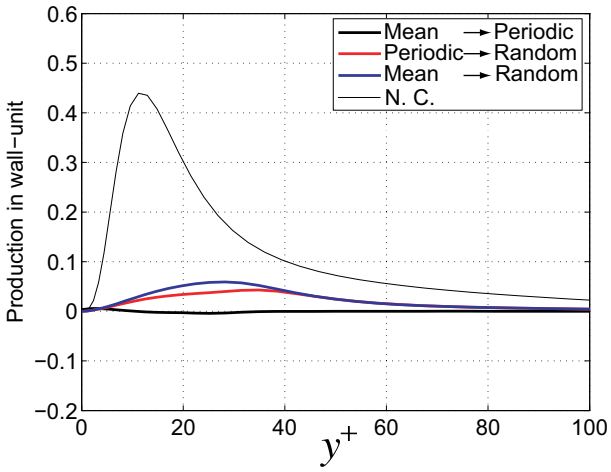

Figure 3.26: Production terms decomposed into three components at $a = 0.1$, $c = -2$ and $k = 0.5$.

pumping power of the uncontrolled flow as a function of wavespeed at $k = 0.5$. The actuation power is positive at $c \leq -2$ or $c > 1$ and the drag is decreased at $c \leq -1$. Since $|W_a|$ is found to be minimum with drag reduction at $c = -2.0$, the maximum net saving rate is obtained. The net saving rate becomes poor at faster upstream traveling wave due to increasing $|W_a|$.

Figure 3.25 shows the RSS profile at $k = 0.5$ and $c = -2.0$. The total-RSS is found to decrease and it almost corresponds to the random-RSS, i.e., the periodic-RSS is very small. The phase profiles of Fourier coefficient and the difference of them are also shown. Since the phase difference is almost zero which indicates that the velocities are in quadrature, the periodic-RSS is almost zero in the whole channel. The actuation power is deduced to be required to induce the periodic-RSS. Therefore, the maximum net saving rate is obtained at $c = -2.0$ because the periodic-RSS is very small.

The decrease of this random-RSS can be explained by the indirect and stabilization effects. Strictly speaking, the periodic-RSS is found to be slightly negative, which decreases the random-RSS due to the indirect effect. Moreover, the profile of this phase difference is similar to that of the downstream traveling wave (Lee et al., 2008; Lieu et al., 2010; Moarref and Jovanovic, 2010).

Figure 3.26 shows the three component decomposed production term at $k = 0.5$ and $c = -2.0$. The production term, P^{mp}, is very small while that at $c = -5.0$ is negative in

the region near the wall. On the other hand, P^{mr} and P^{pr} are found to decrease, which are lower than that at $c = -5.0$.

3.3.4 Parametric study

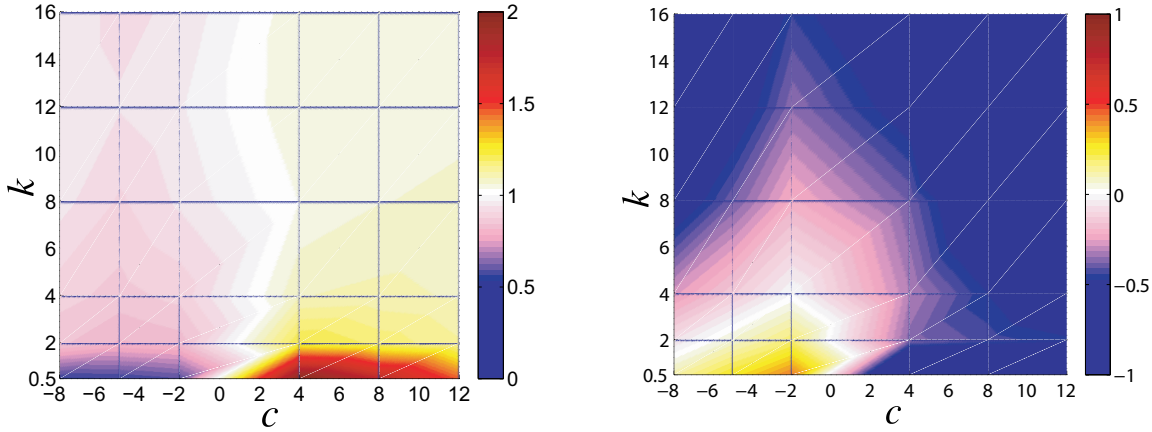

Figure 3.27: Left, normalized skin-friction coefficient, C_f/C_{f0}; right, net saving rate, S ($a = 0.1$ and $\mathrm{Re}_b = 5600$).

A parametric study is made for a range of $k = 0.5$, 2, 4, 8, 12, and 16; $c = -5$, -2, 4, 8, and 12; namely, 30 parameter sets are simulated at $a = 0.1$ and $\mathrm{Re}_{\tau 0} \approx 177$.

Figure 3.27 shows the normalized skin-friction coefficient, C_f/C_{f0}, and the net saving rate, S, as a function of the wavenumber and wavespeed. Skin-friction drag decreases for $c < 0$ whereas it increases for $c > 0$. As increasing k, the increment of skin-friction drag from the uncontrolled level is found to decrease. This trend is similar to the result of the varicose mode of the laminar flow confirmed in Fig. 2.25. For the net saving rate, it is possible to have a positive value in such a fully turbulent channel flow, whereas it is impossible in a laminar flow in accordance with a mathematical proof by Fukagata et al. (2009) and Bewley (2009). Actually, $S > 0$ is obtained by $c < 0$ and $k > 0$ while $S < 0$ for the other parameter sets. The poor S is due to a massive actuation power required.

Again, Eq. (3.80) indicates that the drag increment from the laminar level consists of the periodic and random components. The contributions of them are mapped in Fig. 3.28. The periodic contribution is negative for $c < 0$ and positive for $c > 0$, which is a consistent with laminar flow. The random contribution is found to be positive for all parameters because it reflects the QSV, which induces positive random-RSS.

Figure 3.29 displays the volume averaged $\widetilde{u}\widetilde{u}$ and the random-TKE in the channel domain, i.e., $\frac{1}{V}\int_V \widetilde{u}\widetilde{u}dv$ and $\frac{1}{V}\int_V u''u''dv$. For the small wavenumber, $\frac{1}{V}\int_V \widetilde{u}\widetilde{u}dv$ is found

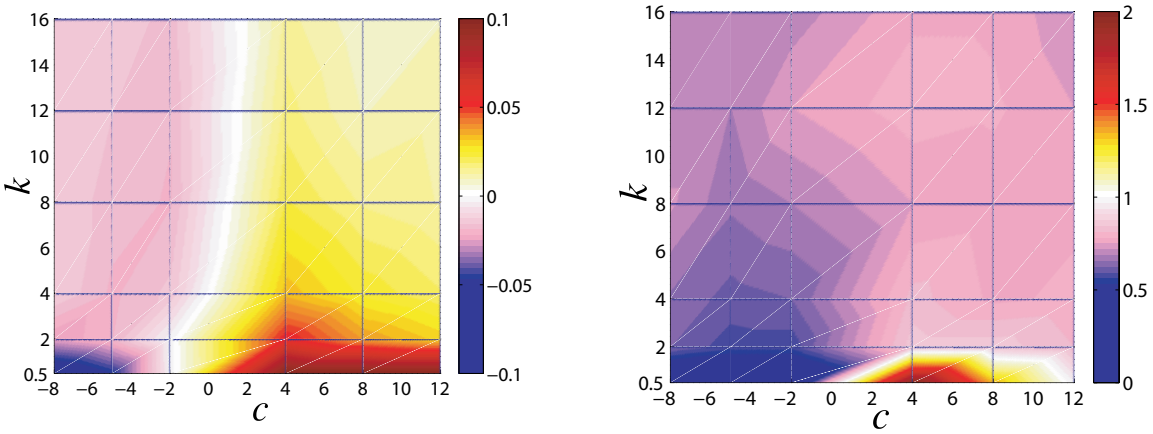

Figure 3.28: Contribution to skin-friction drag coefficient: left, periodic contribution ($C_{f,\,\mathrm{periodic}}/C_{f0}$); right, random contribution ($C_{f,\,\mathrm{random}}/C_{f0}$).

to be large regardless of the wavespeed, which indicates that the periodic component dominates the flow at low wavenumbers. The random-TKE is found to decrease except the parameter set which enhances the drag. Because a decreased random-TKE is observed for the larger wavenumber, the traveling wave-like control potentially decreases the QSV. In other words, it would have an effect of stabilization of flow.

Figure 3.30 shows the scaled influence layer thickness, $\delta_{b/s}\sqrt{|c|k\mathrm{Re}_b}$, and the phase shift, α. The definition of an influence layer thickness, $\delta_{b/s}$, is the same as that in Chap. 2, i.e., the peak location of the periodic-RSS. The resultant scaled influence layer thickness exhibits an almost constant value regardless of the control input except for $c<0$ and $k<2$. Roughly speaking, an analogy with the Stokes' problem is found to hold in turbulent channel flows, too.

The phase shift, α, is determined by using the phase of the wall-normal velocity of the periodic-component as

$$\alpha = \arg\widetilde{u}_k - (-\frac{\pi}{2}), \tag{3.92}$$

where the peak of the periodic-RSS exists in the lower half of the channel. Since the phase relationship under an inviscid flow with a traveling wave-like blowing/suction is not compared with that under a viscous flow, the phase shift is defined as the difference between $\arg\widetilde{u}_k$ and $-\frac{\pi}{2}$ in contrast to Eq. (2.24).

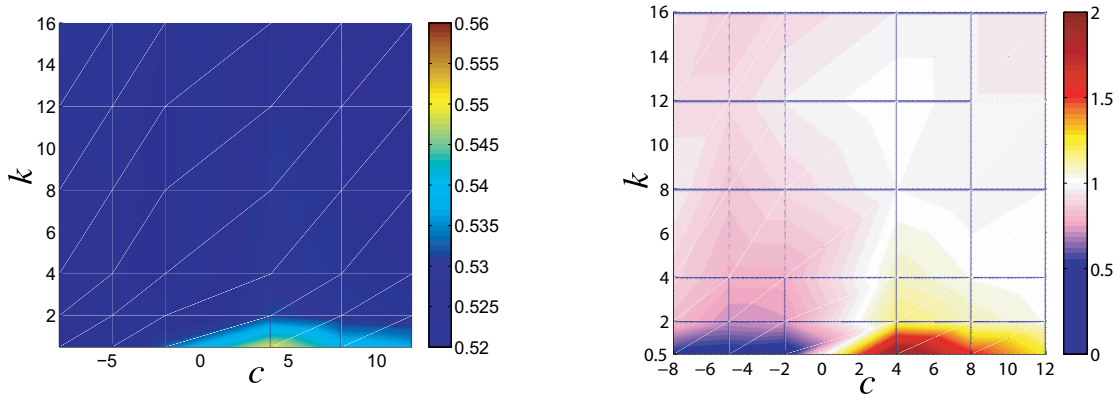

Figure 3.29: Left, volume averaged $\widetilde{u}\widetilde{u}$; right, random-TKE normalized by uncontrolled one.

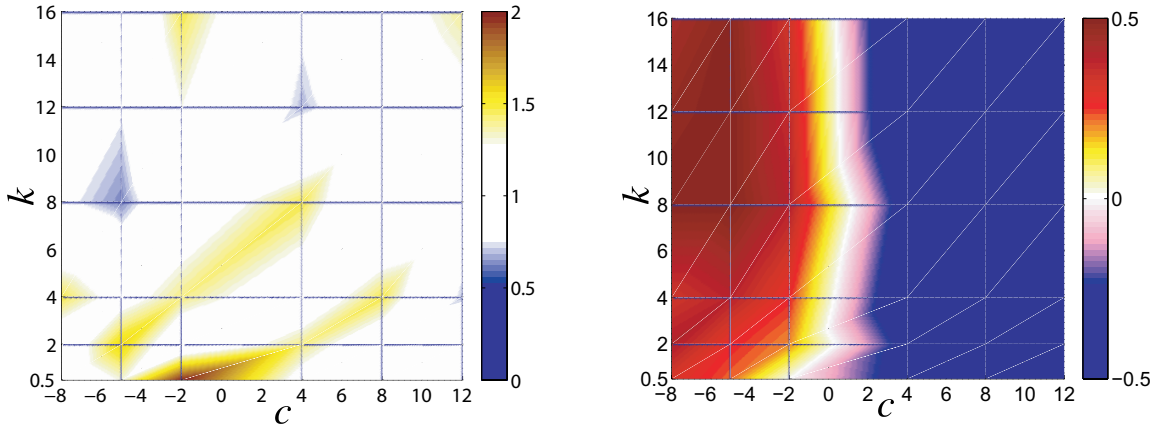

Figure 3.30: Left, scaled influence layer thickness $\left(\delta_{b/s}\sqrt{|c|k\mathrm{Re}_\mathrm{b}}\right)$; right, phase shift ($\alpha$).

Since $\arg\widetilde{u}_k = 0$ and only varicose mode is considered, the phase difference, ϕ, which decides the profile of the periodic-RSS, is expressed as

$$\phi = \arg\widehat{\widetilde{u}}_k - \arg\widehat{\widetilde{v}}_k + \frac{\pi}{2}, \tag{3.93}$$

$$= \alpha. \tag{3.94}$$

According to Eqs. (2.20)-(2.21), the drag reduction and increase of the periodic components are obtained by the upstream and downstream traveling waves, respectively, as confirmed by Fig. 3.28. This explanation is in accordance of that for the laminar flow.

3.4 Wall-normal Lorenz force

The traveling wave-like blowing/suction control sustains the sublaminar drag since it induces the negative RSS in the region near the wall. The three component decomposition showed that the periodic-RSS is possible to be negative in the region near the wall whereas the random-RSS is always positive.

In order to discuss this negative RSS, the traveling wave-like wall-normal Lorenz force is also investigated in this section. This control, shown later, is found to decrease the skin-friction drag at $c = 0$ and generate the negative RSS in the region near the wall. While the boundary condition and the control input are different from the blowing/suction case, it is worth to discuss the generation of the negative-RSS by the wall-normal Lorenz force.

As a control input, the traveling wave-like Lorenz force distribution is considered instead of the blowing/suction. The mathematical form of this traveling wave-like wall-normal Lorenz force, which is F_i in Eq. (3.2), is

$$\begin{cases} F_x &= F_z = 0, \\ F_y &= I \exp\left(-\dfrac{y^+}{\Delta^+}\right) \cos\left(k\left(x - ct\right)\right), \end{cases} \tag{3.95}$$

in the lower half of the channel. The opposed sign of this profile is applied in the upper half region of the channel. Here, I and Δ^+ are the amplitude and penetration length of the Lorentz force, respectively. The wall-normal body force is distributed sinusoidally in the streamwise direction and damping in the wall-normal direction (Berger et al., 2000). The superscript of $+$ denotes the wall units. The wavenumber and wavespeed are denoted as k and c, respectively.

Figure 3.31 shows the drag reduction rate as a function of the wavespeed for different wavenumbers. The penetration length and amplitude are fixed at $\Delta^+ = 10$ and $I = 1.0$. The drag reduction rate is found to be positive (i.e., the drag reduction) at $c = 0$ and it is almost zero or negative when the wave travels. Namely, only the standing wave decreases the skin-friction drag in contrast to the case of blowing/suction (Min et al., 2006).

Figure 3.32(a) shows the drag reduction rate by the standing wave as a function of wavenumber for two different penetration lengths. The maximum drag reduction

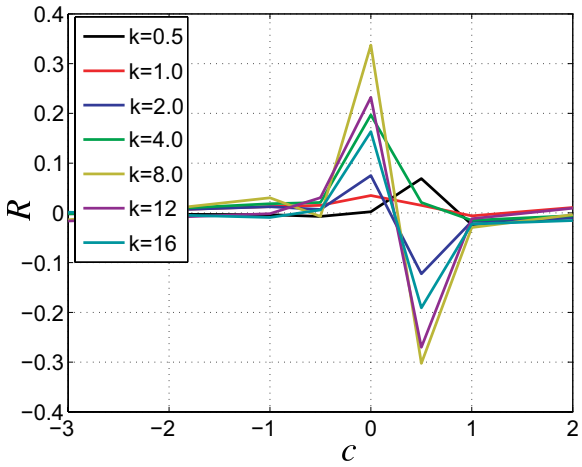

Figure 3.31: Drag reduction rate as a function of wavespeed for different wavenumber ($I = 1.0$ and $\Delta^+ = 10$).

is obtained at $k = 8$ for both penetration lengths. Figure 3.32(b) shows the net saving rate, S, as a function of wavenumber. Here, the actuation work, W_{in}, is defined as

$$W_{in} = \int_v F_i v_i dv. \tag{3.96}$$

The net saving rate, however, is found to be poor or negative for considered parameters because the body force requires larger amount of actuation power than the blowing/suction does. In the following, a parameter set of ($I = 1$, $c = 0$, $k = 8$, and $\Delta^+ = 10$), which induces the maximum drag reduction, is chosen as a reference case.

Figure 3.33 visualizes the vortex cores in the lower half of the channel in the reference case achieving 35% drag reduction. While the QSV is found to disappear, the spanwise roller-like vortex is observed. Such spanwise roller-like vortex is known to induce the slip velocity and lead to drag reduction (Bewley, 2001; Fukagata et al., 2005b; Koumoutsakos, 1998).

In the following, three component decomposition is introduced to analyze the spanwise roller-like vortex. Figure 3.34 shows the rms values of the random velocity component in the reference case compared with the total rms value in the uncontrolled case. The peak of the streamwise component in the reference case is found to shift toward the wall, while it is below the uncontrolled one, i.e., $y^+ > 18$. The other components in the reference case are also found to decrease.

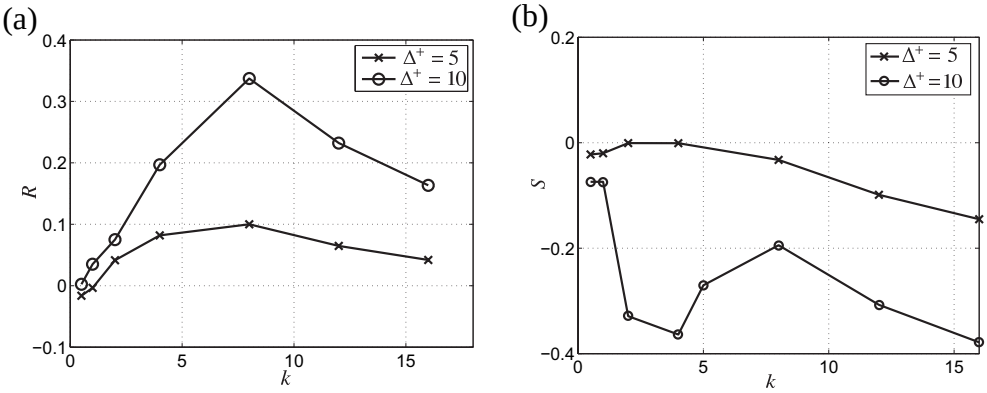

Figure 3.32: (a) Drag reduction rate and (b) net saving rate by the standing wave as a function of wavenumber for different penetration lengths ($I = 1.0$).

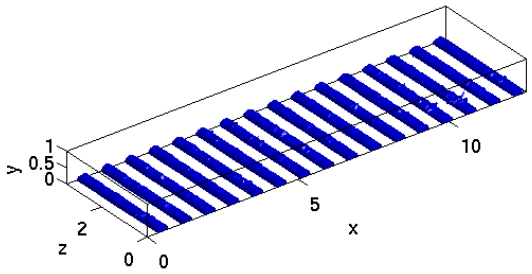

Figure 3.33: Visualization of vortical structures ($Q^+ = -0.05$) in the lower half of the channel: top, uncontrolled flow; bottom, controlled by wall-normal Lorentz force (reference case: $I = 1.0$, $\Delta^+ = 5$, $k = 8.0$, and $c = 0.0$).

Figure 3.35(a) shows the profiles of these RSSs in the reference case. The RSS is found to be negative in the region near the wall due to the negative phase-RSS in $0 < y^+ < 40$. The random-RSS is found to decrease but kept positive. This tendency is similar to that of the blowing/suction case. Figure 3.35(b) shows the phase relationship among the phase averaged velocities and the phase difference where the wavenumber of the Fourier coefficient is chosen at that of the input traveling wave. Non-quadrature (i.e., $\phi \neq 0$ or $\pi/2$) appears in $0 < y < 0.1$, which corresponds to the layer of negative

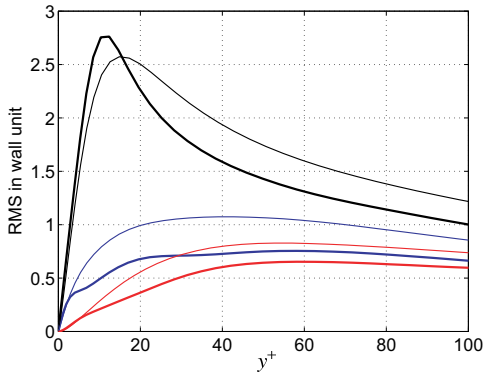

Figure 3.34: Rms values of random velocity component on the reference case (thick line) compared with the total rms value on the uncontrolled case (thin line): Black, streamwise; red, wall-normal; blue, spanwise components.

(a) (b)

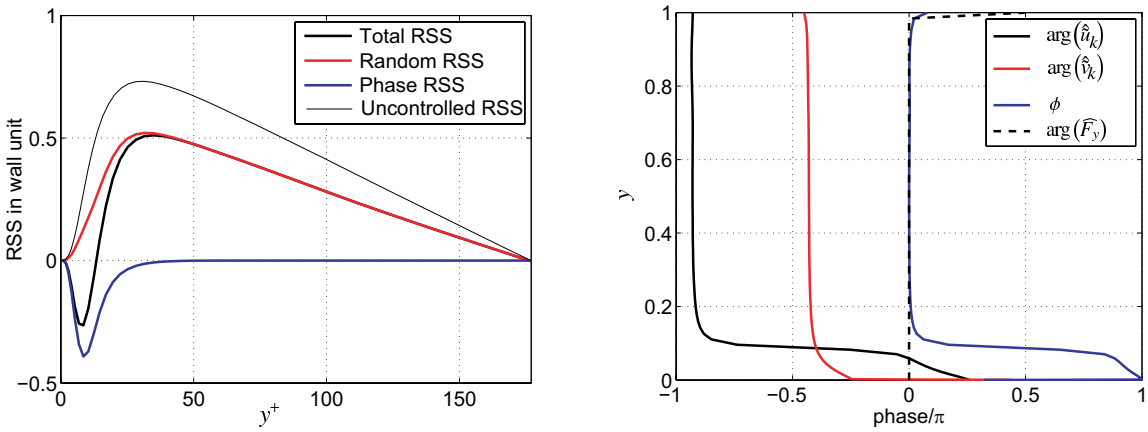

Figure 3.35: (a) Reynolds shear stress; (b) phase of the Fourier coefficients of velocities and body force.

phase-RSS. This non-quadrature is due to the phase reversal of $\tilde{u}$ in the region near the wall.

Figure 3.36(a) shows the distribution of wall-normal Lorenz Force together with the phase-averaged velocity vector in the region near the wall. Spanwise roller-like vortices appear in the region where the Lorenz force is positive, while the flow is expanded in the negative body force region. Figure 3.36(b) shows the distribution of

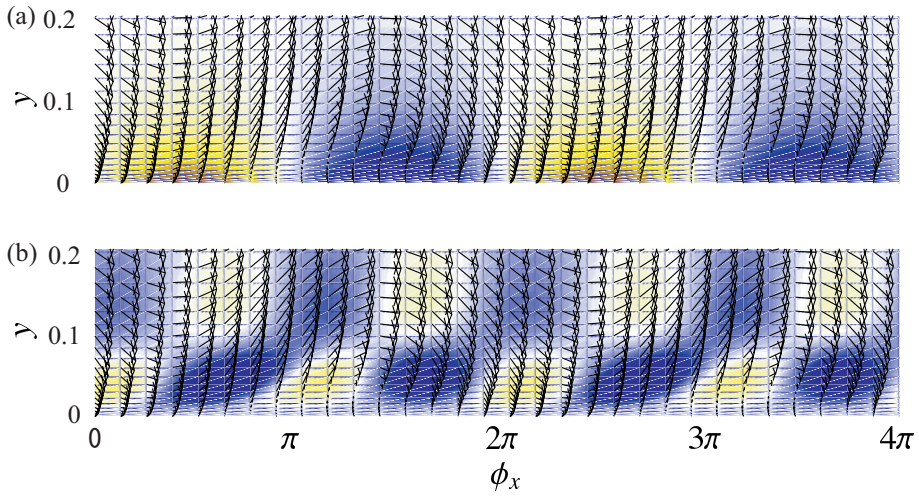

Figure 3.36: (a) Body force (the standing wave-like wall-normal Lorenz force); (b) product of the phase velocities, $-\widetilde{u}\widetilde{v}$, with velocity vector in the region near the wall of the reference case. The domain for the streamwise direction is extended for twice. The color of red and blue indicates the positive and negative value, respectively.

the product of the phase velocities, $-\tilde{u}\tilde{v}$. The negative and positive regions are found around and inside the spanwise roller-like vortices, which contributes to $-\overline{\tilde{u}\tilde{v}} < 0$ as shown in Fig. 3.35(a).

The quadrant decomposition for the periodic-RSS are shown in Fig. 3.37. Here, the same manner of the quadrant analysis defined in Eqs. (3.81)-(3.84) is employed. Large $Q1$ and $Q3$ events, which contribute to decrease the skin-friction drag, are observed upstream and inside of the spanwise roller-like vortex, respectively. On the other hand, $Q2$ and $Q4$ events, which increase the skin-friction drag, are observed inside and downstream of the spanwise roller-like vortex.

Figure 3.38 explains the mechanism how the negative phase-RSS is produced around the spanwise roller-like vortex. The positive and negative $-\tilde{u}\tilde{v}$ are generated inside this vortex due to the rotation of vortex, where $\tilde{u} < 0$. Above this spanwise roller-like vortex, the fluid is accelerated because this vortex induces a slip velocity on the surface of the vortex and the bulk velocity is kept constant at any streamwise positions. Therefore, the fluid particle, labeled as "Fluid 1" , brings $\tilde{u} > 0$ and travels into the region near the wall due to the downward rush ($\tilde{v} < 0$) of the roller-like vortex, where

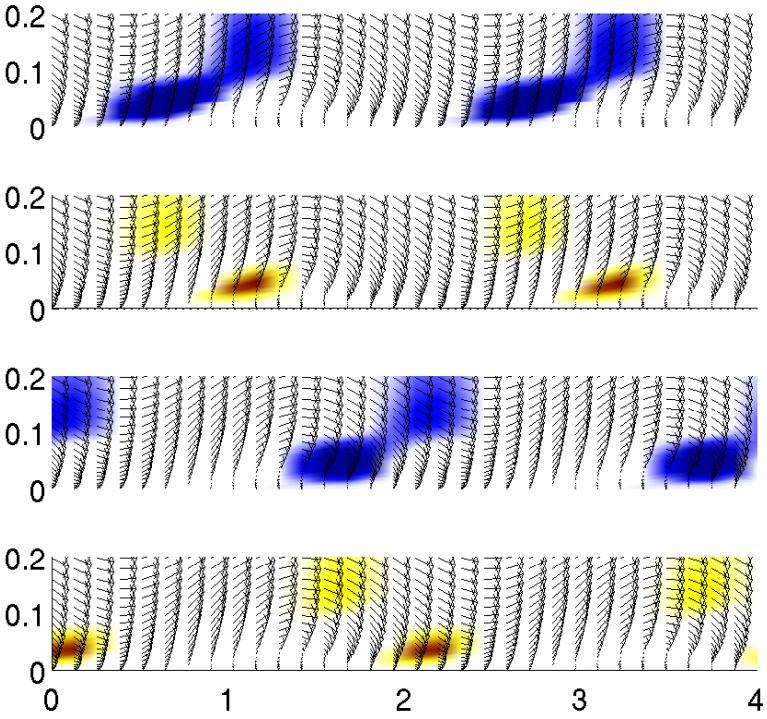

Figure 3.37: Decomposition of periodic-RSS: top, Q1; second, Q2; third, Q3; bottom, Q4.

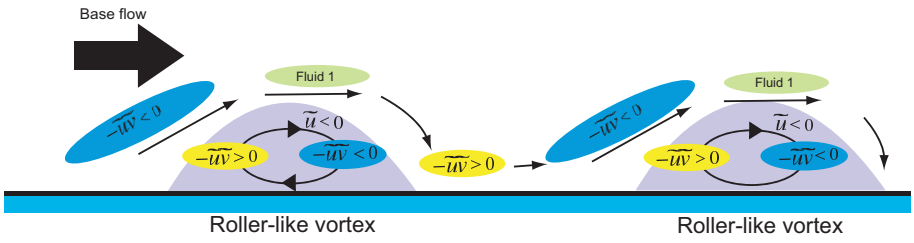

Figure 3.38: Mechanism how the phase RSS is generated around and inside the spanwise roller-like vortex.

$-\tilde{u}\tilde{v} > 0$ is generated. After the convection of "Fluid 1" in the downstream direction, it is pushed up by the upward rush induced by the rotation of the spanwise roller-like vor-

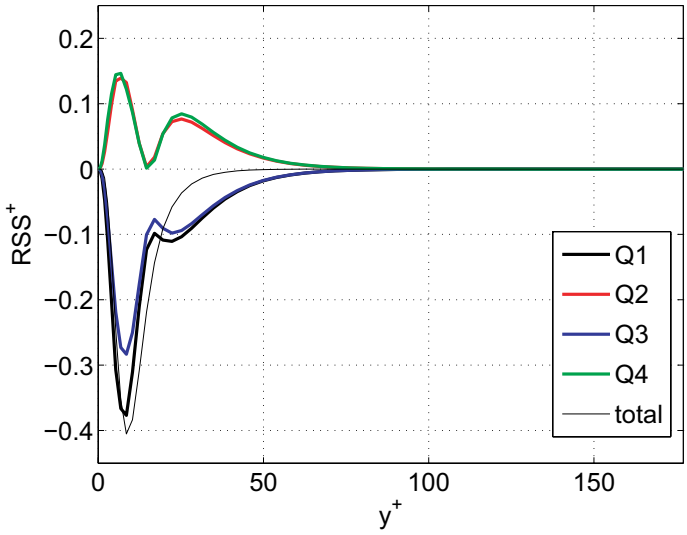

Figure 3.39: Profile of the quadrant decomposed periodic-RSS.

tex; thus, $-\tilde{u}\tilde{v} < 0$ is generated. Because the mean velocity is imposed, more $-\tilde{u}\tilde{v} < 0$ is generated than $-\tilde{u}\tilde{v} > 0$.

Figure 3.39 shows the profile of the streamwise averaged $Q1$-$Q4$ against the wall-normal coordinate. The contribution from the $Q1$ and $Q3$ overcomes that of the $Q2$ and $Q4$ in the region near the wall, whereas these are cancelled each other in the far-wall region. Consequently, the skin-friction drag reduction is obtained.

3.4.1 Comparison with linear analysis

In the fully developed turbulent channel flow, the negative phase-RSS is generated by the spanwise roller-like vortex induced by the forcing in the region near the wall. Here, the phase-averaged velocity is compared with the laminar flow case of the same input parameters. The controlled laminar velocity field is obtained by using the linear analysis presented in Sec. 2.

The governing equations are two-dimensional and linearized: $u = \overline{u} + \widetilde{u}$, $v = \widetilde{v}$, and $p = \overline{p} + \widetilde{p}$ are substituted into the continuity and a Navier-Stokes equations and the

higher-order terms of phase component are neglected, i.e.,

$$\frac{\partial \widetilde{u}}{\partial x}+\frac{\partial \widetilde{v}}{\partial y} = 0, \tag{3.97}$$

$$\overline{u}\frac{\partial \widetilde{u}}{\partial x}+\widetilde{v}\frac{\partial \overline{u}}{\partial y} = -\frac{\partial \widetilde{p}}{\partial x}+\frac{1}{\mathrm{Re}_b}\frac{\partial^2 \widetilde{u}}{\partial x_k \partial x_k}, \tag{3.98}$$

$$\overline{u}\frac{\partial \widetilde{v}}{\partial x} = -\frac{\partial \widetilde{p}}{\partial y}+\frac{1}{\mathrm{Re}_b}\frac{\partial^2 \widetilde{v}}{\partial x_k \partial x_k}+F_y. \tag{3.99}$$

Here, the flow is steady because the control input is steady. Since the flow in this case is not turbulent, the laminar Poiseuille flow profile is employed for the base flow under the same Reynolds number, $\mathrm{Re}_b = 5600$. These equations are solved by using the Fourier transform for the streamwise direction and the Chebyshev collocation method for the wall-normal direction. As a control input, the same form of the wall-normal Lorenz force is added as the body force term of Eq. (3.99). The control parameters are set the same as those of the reference case of the turbulent flow.

Figure 3.40(a) shows the comparison between the phase-RSSs, $-\widetilde{u}\widetilde{v}$, of the laminar and turbulent flows. In both cases, negative RSS is obtained in the region near the wall, while the negative peak in the turbulent flow is lager than that in the laminar flow. Figure 3.40(b) shows the phase profile of the Fourier coefficient, which is identical to that of the turbulent flow. Figure 3.41 shows that the distribution of the body force and the product of $\widetilde{u}$ and $\widetilde{v}$ (with the velocity vector) are also similar to the results of the turbulent flow. Therefore, it can be concluded that the spanwise roller-like vortex is well described by the linearized Navier-stokes equation.

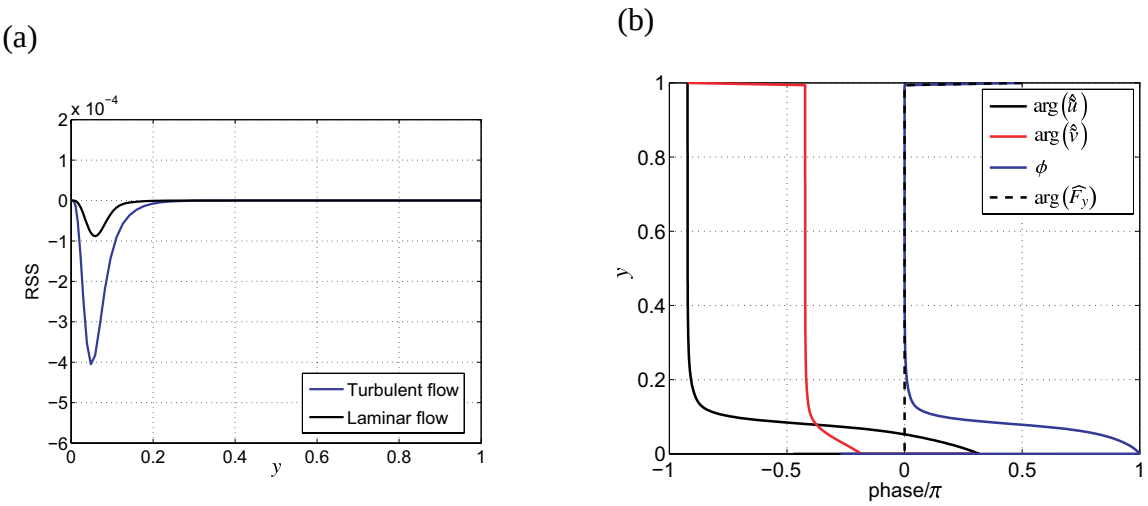

Figure 3.40: (a) Comparison of phase-RSS in the turbulent and laminar flows. (b) Phase profiles of the Fourier coefficient of the velocities and the body force in the laminar flow.

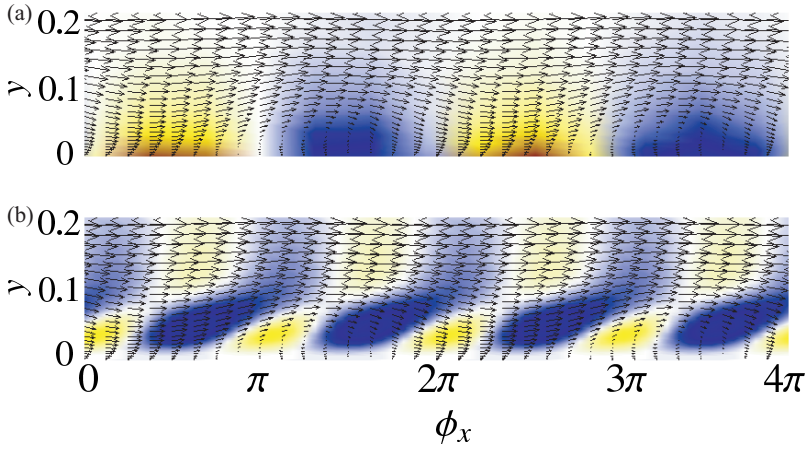

Figure 3.41: (a) Body force and (b) product of phase velocities, $-\widetilde{u}\widetilde{v}$, with the velocity vector in the laminar flow. The control parameter is set to the same as the reference case.

3.5 Comparison between blowing/suction and wall-normal forcing

Table 3.4 summarizes a comparison between the traveling wave-like blowing/suction control and standing wave-like wall-normal forcing. For both controls, skin-friction drag reduction is obtained not only by the decrease of RSS below the uncontrolled level, but also the generation of the negative RSS. The blowing/suction control decreases the drag when the wave travels to the upstream direction while the wall-normal forcing control decreases the drag when the wave stands. The reason of this difference is originated from the control input and the boundary condition for the velocities. For the blowing/suction case, the input wall-normal velocity from the wall induces non-quadrature between the streamwise and wall-normal velocities, which contributes to the increment of the skin-friction drag of the periodic component. This non-quadrature is found to be maximum on the wall. On the other hand, for the wall-normal forcing case, the body force is applied instead of the wall transpiration; namely the no-slip condition for the velocity is imposed on the wall. The spanwise roller-like structure appears and induces non-quadrature in the region near the wall, i.e., not on the wall. Actually, quadrature is held on the wall due to the no-slip condition.

In term of efficiency, the wall-normal forcing does not induce positive gain because the generation of the fluid motion by the body force requires more energy than the applying the wall velocity directly.

Table 3.4: Comparison between blowing/suction and Lorenz force

	Blowing/suction	Lorenz force
Re_b	5600	5600
Velocity at wall	$\begin{cases} u_w &= 0 \\ v_{w\pm} &= \mp a\sin((x-ct)) \\ w_w &= 0 \end{cases}$	no-slip
Body force	none	$\begin{cases} F_x &= 0 \\ F_y &= I\exp\left(-\frac{y^+}{\Delta^+}\right)\cos(k(x-ct)) \\ F_z &= 0 \end{cases}$
Drag decreases by	upstream traveling wave	standing wave
Phenomena	phase shift	spanwise roller-like vortex
periodic-RSS	negative	negative

3.6 Summary

A series of direct numerical simulations is performed an fully developed turbulent channel flows. The mean flow is driven by a mean pressure gradient in order to keep the constant flow rate at $\mathrm{Re}_b = 5600$ that corresponds to $\mathrm{Re}_\tau \approx 177$.

First, validation and verification of the employed DNS code are presented without any control. The statistics, i.e., the mean velocity, Reynolds stress component and budget of the transport equation of the Reynolds stress are in excellent agreement with the data obtained by the spectral method.

Second, the flows subjected to the traveling wave-like blowing/suction were investigated. The upstream traveling wave not only decreases skin-friction drag but also gains positive efficiency, whereas the downstream traveling wave increases skin-friction drag. Negative RSS appears in the region near the wall, which contributes to the significant drag reduction due to the traveling wave control, while it is not generated for the opposition control and the suboptimal control. Actually, the skin-friction drag is more reduced by the upstream traveling wave than the opposition and the suboptimal control.

The three-component decomposition (i.e., mean, periodic, and random component) is employed to discuss the mechanism of the drag reduction effect. When the wave travels to the upstream direction, the periodic RSS is found to be negative in the region near the wall but zero in the far wall region. The random-RSS, however, is positive in the whole channel, while the profile is below the uncontrolled level. Not only the random-RSS, but also the random-RNS is found to be decreased by the upstream traveling wave. The decrease of this random component can be explained by the indirect effect. The phase analysis introduced in Chap. 2 explains the mechanism for the negative periodic-RSS: the non-quadrature between the streamwise and wall-normal velocities of the periodic component contributes to generate the negative RSS profile in the region near the wall. This explanation is confirmed for the wider range of wavespeed and wavenumber. The periodic-RSS is almost zero when the wavespeed is small and negative (e.g., $c = -2$ for $k = 0.5$), which induces the maximum net saving rate due to the actuation work is very small. The decrease of the random components in this case can be explained by the indirect effect due to the constraint of constant flow rate and the stabilization effect.

Finally, the control effect of the traveling wave-like wall-normal forcing is considered inspired by the blowing/suction control. The flow behavior in the region near the wall is expected to similar to that induced by the blowing/suction control. The standing wave (i.e., $c = 0$) is found to decrease the skin-friction drag in contrast to the blowing/suction case, while the positive efficiency is not obtained. Due to the wave-like wall-normal forcing, the spanwise roller-like vortical structure appears, which generates negative RSS in the region near the wall. The resultant phase relationship between the velocity component of the periodic component is similar to that of the linear analysis.

Chapter 4

Higher Reynolds number turbulent flow

Control effect at a relatively higher Reynolds number fully developed turbulent channel flow is studied by means of large eddy simulation (LES). As a preliminary, a mathematical background of the LES with the coherent structure Smagorinsky model proposed by Kobayashi (2005) is introduced. These simulation results are compared with the DNS database at $\mathrm{Re}_\tau \approx 177$, 395, 595 and 1020. Second, a control effects of the opposition control are compared with Chang et al. (2002) in order to validate this model. Third, the control effect by the traveling wave-like blowing/suction control and Reynolds number dependency of drag reduction rate is shown.

4.1 Large eddy simulation

While DNS can provide accurate data of a flow, flow analysis using DNS is limited to low Reynolds numbers due to the computational resources: the number of grid points, N, requiring for DNS, which can resolve the scale of the Kolmogorov length, is estimated as

$$N = \mathcal{O}(\mathrm{Re}^{9/4}). \tag{4.1}$$

This equation indicates that a huge number of grid points is required to resolve in the high Reynolds number flow i.e., a computational cost increases. Actually, DNS at

such Reynolds number is investigated by only some research groups to best of authors' knowledge. On the other hand, large eddy simulation (LES) is one of the handy tools to simulate such a higher Reynolds number flow, because it is possible to decrease a computational cost i.e., a lot of control parameter sets can be investigated. While the LES cannot provide the accurate data due to use turbulence models, the tendency of a drag reduction rate and a net saving rate for the input parameter can be obtained.

The concept of LES is that the vortex scales is divided into the grid scale (hereafter referred to as GS) and the sub-grid scale (SGS). The GS vortex is computed directly and the SGS vortex is modeled. In the following, the Smagorinsky model, which is the most popular SGS model (Smagorinsky, 1963), is explained following Kajishima's monograph (Kajishima, 1999b).

In order to separate GS and SGS scales, we define a filtering procedure as

$$\overline{f}(x) = \int_{\infty}^{\infty} G(y) f(x-y) dy, \tag{4.2}$$

where $G(y)$ is a filter function, which satisfies

$$\int_{\infty}^{\infty} G(y) dy = 1. \tag{4.3}$$

The bar denotes the grid filter operator, which indicates GS component. The sub-grid scale (SGS) component, f', is defined as difference between instantaneous f and $\overline{f}$, which reads

$$f' = f - \overline{f}. \tag{4.4}$$

The filtered continuity and Navier-Stokes equations are, respectively,

$$\frac{\partial \overline{u_i^*}}{\partial x_i^*} = 0, \tag{4.5}$$

$$\frac{\partial \overline{u_i^*}}{\partial t} + \frac{\partial}{\partial x_j^*} \overline{u_j^* u_i^*} = -\frac{1}{\rho^*} \frac{\partial \overline{p^*}}{\partial x_i^*} + \frac{\partial}{\partial x_j^*} \left(2\nu^* \overline{S_{ij}^*} \right), \tag{4.6}$$

where the GS strain tensor, S_{ij}^*, is

$$S_{ij}^* = \frac{1}{2} \left(\frac{\partial \overline{u_i^*}}{\partial x_j^*} + \frac{\partial \overline{u_j^*}}{\partial x_i^*} \right) \tag{4.7}$$

The asterisk denotes the dimensional variable. In Eq. (4.6), $\overline{u_i^* u_j^*}$ is an unknown variable. This equation is rewritten as follows:

$$\frac{\partial \overline{u_i^*}}{\partial t} + \frac{\partial}{\partial x_j^*}\overline{u}_j^* \overline{u}_i^* = -\frac{1}{\rho^*}\frac{\partial \overline{p^*}}{\partial x_i^*} + \frac{\partial}{\partial x_j^*}(-\underbrace{(\overline{u_i^* u_j^*} - \overline{u}_i^* \overline{u}_j^*)}_{\tau_{ij}^*} + 2\nu^* \overline{S_{ij}^*}). \tag{4.8}$$

Then, GS components, $(\overline{\mathbf{u}_i^*}, \overline{p^*})$ are obtained as the solution of the filtered equations (4.5) and (4.8) with an eddy viscosity model for τ_{ij}.

Equations (4.5) and (4.8) are nondimensionalized by the channel half-width, δ^*, and the bulk velocity, u_b^*, i.e.,

$$\frac{\partial \overline{u_i}}{\partial x_i} = 0, \tag{4.9}$$

$$\frac{\partial \overline{u_i}}{\partial t} + \frac{\partial}{\partial x_j}\overline{u}_j \overline{u}_i = -\frac{\partial \overline{p}}{\partial x_i} + \frac{\partial}{\partial x_j}\left(\frac{1}{\mathrm{Re_b}}\frac{\partial \overline{u_i}}{\partial x_j} - \tau_{ij}\right), \tag{4.10}$$

Here, we apply the eddy viscosity model for τ_{ij} as

$$\tau_{ij} = -2\nu_t S_{ij}, \tag{4.11}$$

where ν_t is eddy viscosity. From the dimension analysis and the assumption of local equilibrium between GS and SGS energies, the eddy viscosity, ν_t, in Eq. (4.11) becomes

$$\nu_t = (C_s \Delta)^2 |\overline{S}_{ij}|, \tag{4.12}$$

where C_s is the Smagorinsky constant and Δ is the grid width.

In order to determine C_s, the simplest way is to use the constant Smagorinsky model (CSM). Lilly (1967) estimated C_s from the statistical theory as

$$C_s = 0.235\alpha^{-3/4}, \tag{4.13}$$

where α is the Kormogrov constant, $\alpha = 1.5$. The disadvantage of the CSM are following (Kobayashi, 2005): (1) this value is not universal, viz., it depends on the flow field, (2) the wall-dumping function, f_s,

$$f_s = 1 - \exp\frac{-y^+}{A^+}, \tag{4.14}$$

should be used to suppress the near-wall eddy viscosity (where A^+ is the dimensionless constant, $A^+ \approx 25$), (3) the laminarization cannot be captured.

On the other hand, Germano et al. (1991) proposed a new idea to improve the drawbacks of the CSM, i.e., the dynamic Smagorinsky model (DSM). In the DSM (Germano et al., 1991; Lilly, 1992), the Smagorinsky constant is computed by using a test filter, but assuming not constant value for C_s. Therefore, C_s is determined locally and temporally. The other problems, however, appear: (1) the computational instability appears because negative value of C_s, which induces inverse energy cascade, can appear. (2) the cost of the computation increases due to the test filtering procedure.

Kobayashi (2005) proposed a new model, in which C_s is determined based on the coherent structure in the region near the wall. According to this coherent structure Smagorinsky model (CSSM), the Smagorinsky constant for a channel flow can be determined as

$$C = C_1 \left| \frac{Q}{E} \right|^{3/2}, \tag{4.15}$$

where C_1 is a constant, $C_1 = \frac{1}{20}$, and Q and E are defined as

$$Q = \frac{1}{2}\left(W_{ij}W_{ij} + S_{ij}S_{ij}\right). \tag{4.16}$$

$$E = \frac{1}{2}\left(W_{ij}W_{ij} - S_{ij}S_{ij}\right). \tag{4.17}$$

The velocity-strain and vorticity tensor are defined, respectively, as

$$S_{ij} = \frac{1}{2}\left(\frac{\partial u_j}{\partial x_i} + \frac{\partial u_i}{\partial x_j}\right), \tag{4.18}$$

$$W_{ij} = \frac{1}{2}\left(\frac{\partial u_j}{\partial x_i} - \frac{\partial u_i}{\partial x_j}\right). \tag{4.19}$$

Equation (4.15) assumes that the turbulent kinetic energy is dissipated around the near-wall vortex. The Smagorinsky constant is computed depending on the instantaneous flow field; namely the damping function is not necessary and the relaminarization can be captured. The computational cost does not increase because we do not apply the test filtering procedure. Thus, this model is expected to be suitable to simulate the controlled high Reynolds number flows.

4.2 Validation and verification

Validation and verification of the uncontrolled flow under the constant flow rate computed by the CSSM-LES are presented. The numerical conditions are tabulated in Table 4.1.

Figure 4.1 shows the statistics of the flow: the mean velocity, shear balance, and rms value for velocity fluctuations at different friction Reynolds numbers i.e., $\mathrm{Re}_\tau \approx 177$, 395, 595, 1020. The size of computational domain and number of grid points are those of Case 3, 7, and 9 at $\mathrm{Re}_\tau \approx 177$, 395, and 595, respectively, in Table 4.1. The mean velocity and the shear balance computed by the CSSM-LES are in a good agreement with those of DNS data. Whereas the rms of streamwise velocity fluctuation is overestimated as compared to the DNS results, that of the wall-normal and spanwise velocities are underestimated. This trend was reported in the original paper of the CSSM-LES by Kobayashi (2005). This is because the pressure-strain term, which redistributes energy among different velocity directions, is not modeled, while the RSS is modeled by using the eddy viscosity. The same trend is also observed for the DSM-LES.

The number of grid points in the wall-normal direction is enough with $N_y = 96$ according to the simulation of the uncontrolled flow. Kobayashi (2005) used $N_y = 64$ to simulate the uncontrolled channel flow and obtained the result which had a good agreement on the mean velocity and u'_{rms} with the DNS result. However, the simulation for the controlled flow requires a higher resolution in the region near the wall, since the transpiration is applied from the wall. In fact, Chang et al. (2002), who studied the Reynolds number dependency of the effect of opposition control by means of the DSM-LES, used $N_y = 149$ at $\mathrm{Re}_\tau \approx 590$. Additionally, the filtering procedure of Eq. (4.3) is applied only in the homogeneous directions, not to inhomogeneous direction i.e., y. Thus, the number of grid points in the wall-normal direction is set to be $N_y = 192$ and 288 at $\mathrm{Re}_\tau = 395$ and 595, respectively, for the simulation of the flow under the opposition and the traveling wave-like blowing/suction controls in this thesis. This number of grid points is approximately equal to that used in DNS at $\mathrm{Re}_\tau \simeq 180$.

Figure 4.2 displays the profile of the rms values and the RSS for different Reynolds number as a function of y. As increasing the Reynolds number, their peaks are shifted toward the wall. The RSS is shown in Fig. 4.6 as a function of y^+. According to

Eq. (1.3), the turbulent contribution for the skin-friction drag coefficient is the integration of the RSS. Therefore, it is confirmed that the RSS in the far-wall region has a large contribution in a high Reynolds number flow.

Table 4.1: Domain size and number of grid points used in the CSSM-LES.

	Method	Re_b	$\mathrm{Re}_{\tau 0}$	$L_x \times L_y \times L_z$	$N_x \times N_y \times N_z$	Δ_x^+	$\Delta_{y,min}^+$	Δ_z^+
	DNS	5600	177	$4\pi \times 2 \times 3.5$	$128 \times 96 \times 128$	8.67	0.089	4.86
Case 1	CSSM-LES	5600	192	$4\pi \times 2 \times 3.5$	$64 \times 96 \times 64$	34.8	0.089	9.68
Case 2	CSSM-LES	5600	186	$4\pi \times 2 \times 3.5$	$32 \times 96 \times 64$	73.0	0.089	9.68
Case 3	CSSM-LES	5600	183	$4\pi \times 2 \times 3.5$	$32 \times 96 \times 32$	71.9	0.089	19.4
	DNS[1]	14000	392	$2\pi \times 2 \times 3.5$	$256 \times 193 \times 192$	10	0.03	6.5
Case 4	CSSM-LES	14000	418	$2\pi \times 2 \times 3.5$	$32 \times 192 \times 64$	83.1	0.085	23.1
Case 5	CSSM-LES	14000	418	$4\pi \times 2 \times 3.5$	$128 \times 96 \times 64$	40.3	0.205	22.4
Case 6	CSSM-LES	14000	423	$4\pi \times 2 \times 3.5$	$64 \times 96 \times 64$	80.5	0.205	22.4
	DNS[1]	21600	587	$2\pi \times 2 \times \pi$	$384 \times 257 \times 384$	9.7	0.04	7.2
Case 7	CSSM-LES	21600	589	$2\pi \times 2 \times 3.5$	$64 \times 288 \times 64$	57.8	0.053	32.2
Case 8	CSSM-LES	21600	594	$2\pi \times 2 \times 3.5$	$64 \times 96 \times 64$	58.3	0.297	32.5
Case 9	CSSM-LES	21600	589	$2\pi \times 2 \times 3.5$	$32 \times 96 \times 64$	116	0.295	32.2
	DNS[2]	41441	1020	$12.8 \times 2 \times 6.4$	$2048 \times 448 \times 1536$	6.38	0.15	4.25
	CSSM-LES	41441	1039	$2\pi \times 2 \times 3.5$	$128 \times 96 \times 128$	50.1	0.5	27.9

[1] Moser et al. (1999)
[2] Abe et al. (2004)

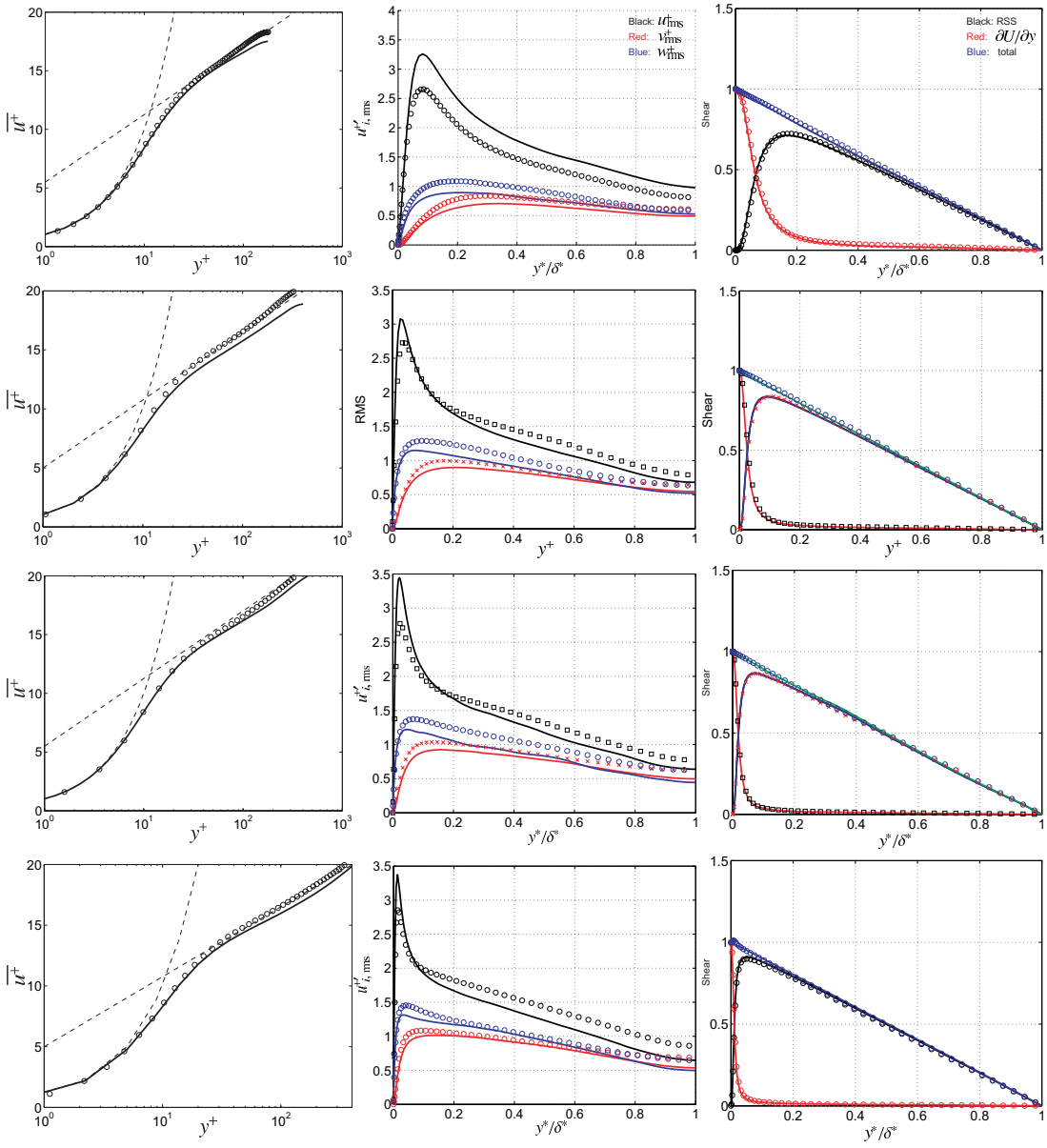

Figure 4.1: Profiles of mean velocity (left), rms values of the velocity fluctuations (center), and shear balance (right). The Reynolds number is 177 (top) in Case 3, 395 (second) in Case 5, 595 (third) in Case 7, and 1020 (bottom). The profiles are compared with the DNS data for $\mathrm{Re}_{\tau 0} \approx 177$, 395, 595 and 1020, denoted by symbols.

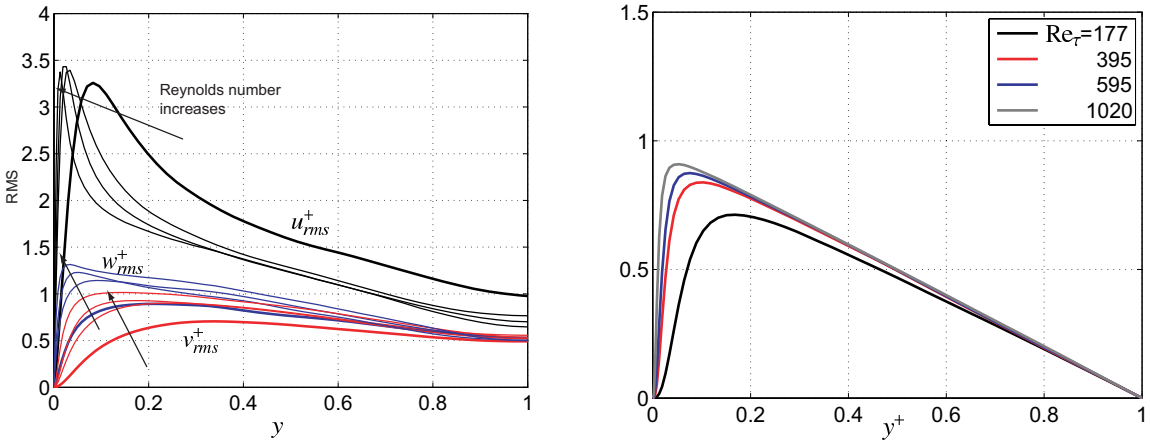

Figure 4.2: Reynolds number dependency of the rms velocities (left) and the RSS (right).

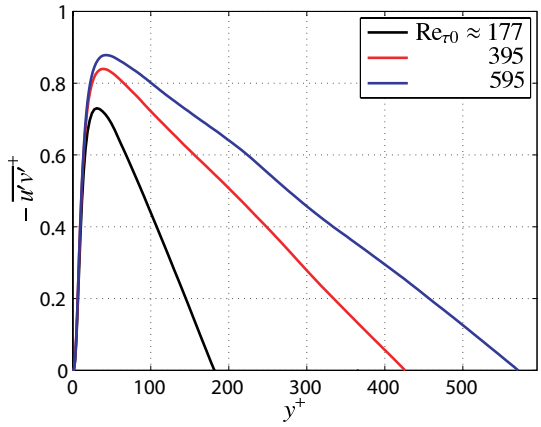

Figure 4.3: Reynolds shear stress as a function of as a function of y^+.

4.3 Opposition control

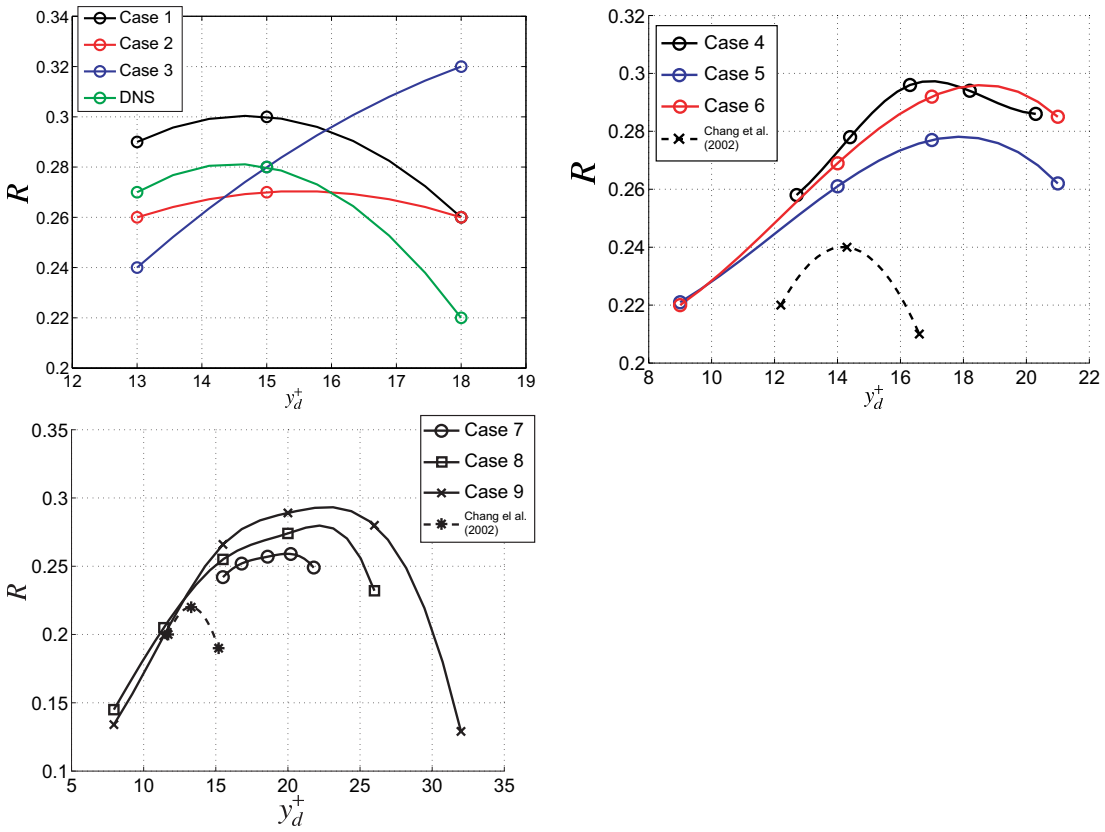

Figure 4.4: Drag reduction rate as a function of detection plane height for different bulk Reynolds numbers: top left, $\mathrm{Re}_{\tau 0} \approx 177$; top right, $\mathrm{Re}_{\tau 0} \approx 395$; top left, $\mathrm{Re}_{\tau 0} \approx 595$.

The control effect due to the *v*-control, (Choi et al., 1994) defined in Eq. (3.73) is investigated by means of CSSM-LES at $\mathrm{Re}_{\tau 0} \approx 180$, 395, and 595. The size of computational domain size and the number of grid points are tabulated in Table 4.1.

Figure 4.4 shows the drag reduction rate as a function of the sensing location. At $\mathrm{Re}_\tau \approx 180$, the optimal sensing location in Case 1 is found to be $y_d^+ \approx 15$, which is in accordance with the DNS result. The value of optimal R, however, is larger than that in DNS. In Case 2, the optimal sensing location is similar to that of DNS, but it is below that of the DNS. At $\mathrm{Re}_\tau \approx 395$ and 595, the present LES predicts higher R than that of the DSM-LES by Chang et al. (2002). The optimal sensing location is shifted away from the wall as increasing Reynolds number, while Chang et al. (2002) showed that it becomes closer to the wall.

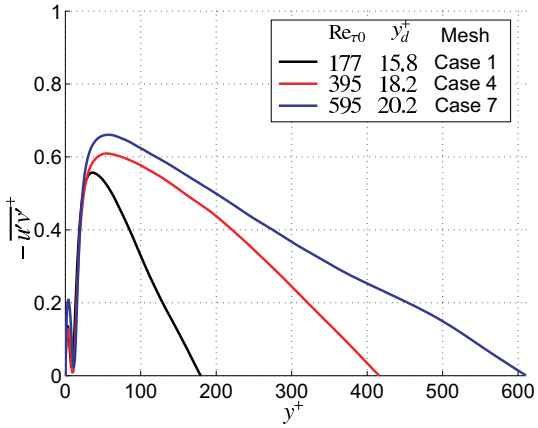

Figure 4.5: RSS profile for different Reynolds numbers under *v*-control.

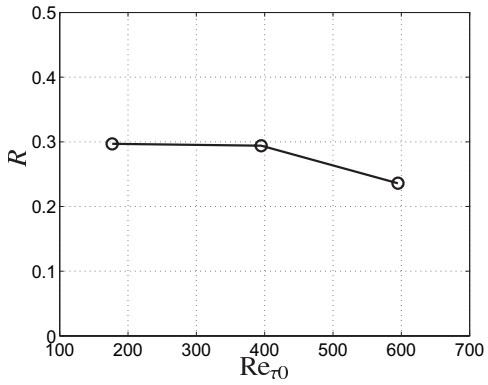

Figure 4.6: The maximum drag reduction rate as a function of the Reynolds number.

Figure 4.5 shows the RSS profile under the *v*-control for different Reynolds numbers. The so-called virtual wall, where $-\overline{u'v'} \approx 0$, appears in the region near the wall. Figure 4.6 also represents the maximum drag reduction rate as a function of the Reynolds number. The effectiveness of the drag reduction decreases as increasing the Reynolds numbers because the contribution from the far-wall region becomes much larger as shown in Fig. 4.5.

4.4 Traveling wave-like blowing/suction

The control effects by the traveling wave-like blowing/suction at $\mathrm{Re}_\tau \approx 177$, 395, and 595 are studied by means of CSSM-LES. The form of this control is identical to Eq. (3.64); therefore, the input parameters are the waveamplitude, wavenumber and wavespeed normalized by the channel half-width and the twice bulk mean velocity.

Figure 4.7 shows the drag reduction rate and the net saving rate as a function of wavespeed. Reasonable agreements in the resultant R and S are confirmed between LES and DNS for each Reynolds number at $k = 1.0$ and $a = 0.1$: $R > 0$ and $S > 0$ for the upstream traveling wave while $R < 0$ and $S < 0$ for the downstream traveling wave. When the wave travels to the upstream direction, R is almost unchanged for each Reynolds number. The net saving rate gradually decreases as increasing wavespeed at $\mathrm{Re}_{\tau 0} \approx 180$, while it is almost unchanged at $\mathrm{Re}_{\tau 0} \approx 395$ and 595. Apparent dependency for the number of grid points is not found at $\mathrm{Re}_{\tau 0} \approx 177$. The drag reduction rate is positive in Case 4, while it is negative for Cases 5 and 6 at $\mathrm{Re}_{\tau 0} \approx 395$, which implies that the flow is sensitive in the range of $-2 < c < 0$. The similar trend is also found for $\mathrm{Re}_{\tau 0} \approx 595$.

Figure 4.8 shows the mean streamwise velocity, the rms value of the velocity fluctuations, and the RSS under the upstream traveling wave for different numbers of grid points compared with controlled and uncontrolled DNS data. The reasonable agreements are obtained between LES and DNS: the mean streamwise velocity decreases in the buffer layer ($y^+ \approx 10$); the rms values are significantly increased; the RSS is found to decrease in the far-wall region, while it slightly increases in the region near the wall.

Figure 4.9 represents the Reynolds number dependency of R and S. The drag reduction rate, R, is found to almost be unchanged at $c = -5.0$, while it gradually decreases as increasing the Reynolds number at $c = -3.0$. On the other hand, S is improved as increasing the Reynolds number for both wavenumbers because the definition of actuation work permits $W_a < 0$ as described in Eq. (3.68). In fact, the negative W_a is observed for $\mathrm{Re}_\tau \approx 395$ and 595 as shown in Fig. 4.10.

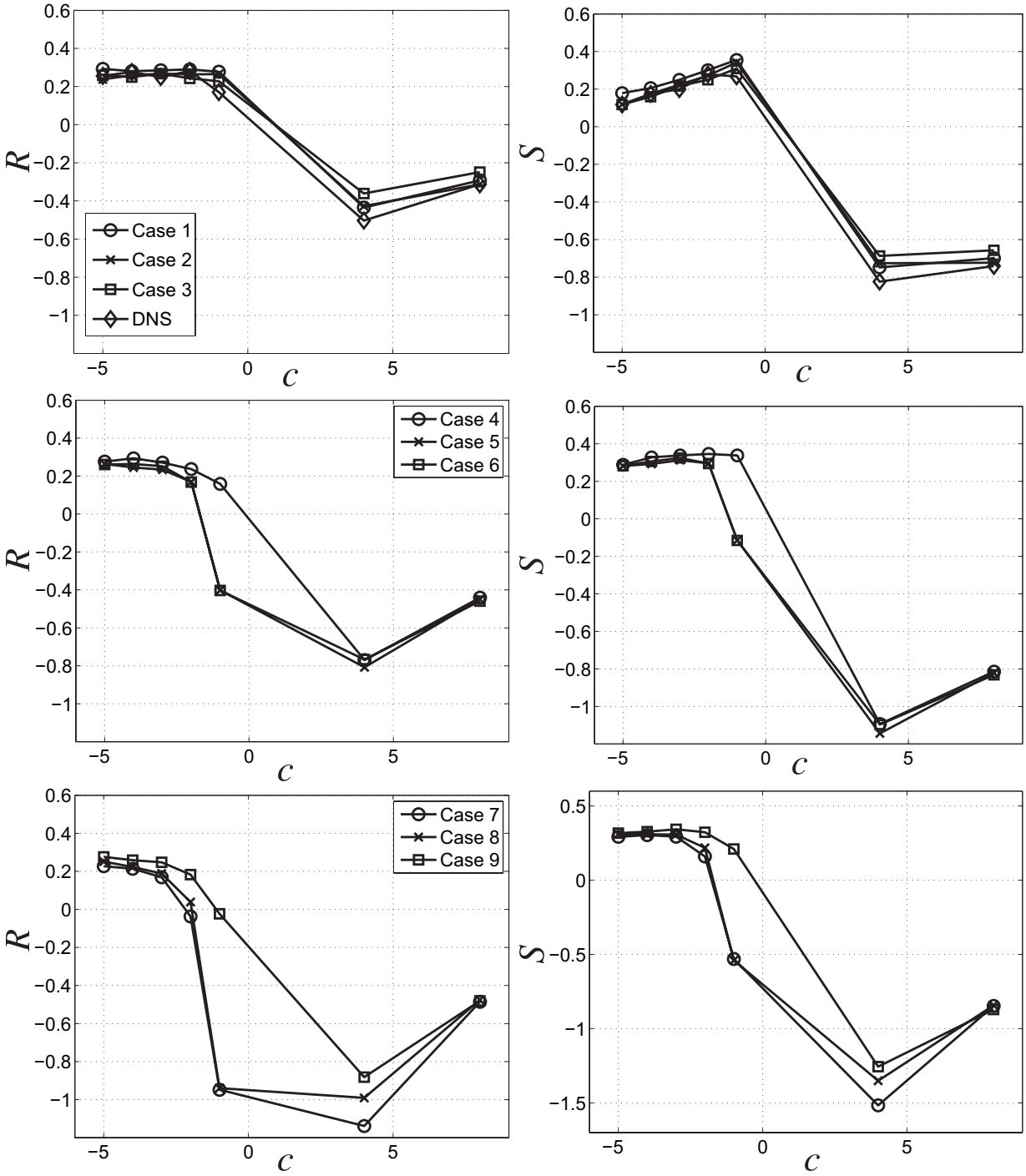

Figure 4.7: Drag reduction rate (left) and net saving rate (right) as a function of wavespeed: top, $\mathrm{Re}_{\tau 0} \approx 177$; middle, $\mathrm{Re}_{\tau 0} \approx 395$; bottom, $\mathrm{Re}_{\tau 0} \approx 595$.

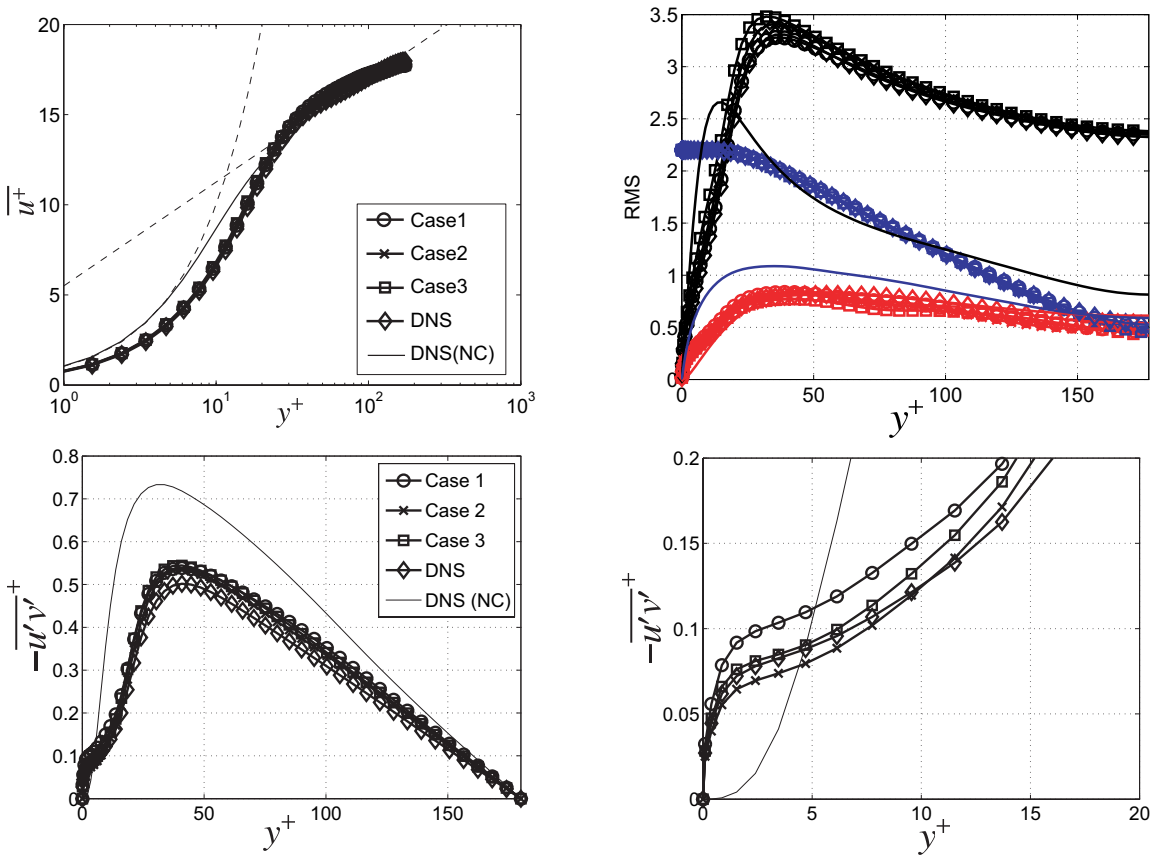

Figure 4.8: Mean streamwise velocity (top, left); rms value of velocity fluctuations (top, right), Reynolds shear stress (bottom, left); zoom-up view of the near-wall RSS (bottom, right). The input parameters are $c = -2.0$, $k = 1.0$, and $a = 0.1$ at $\mathrm{Re}_\tau \approx 180$.

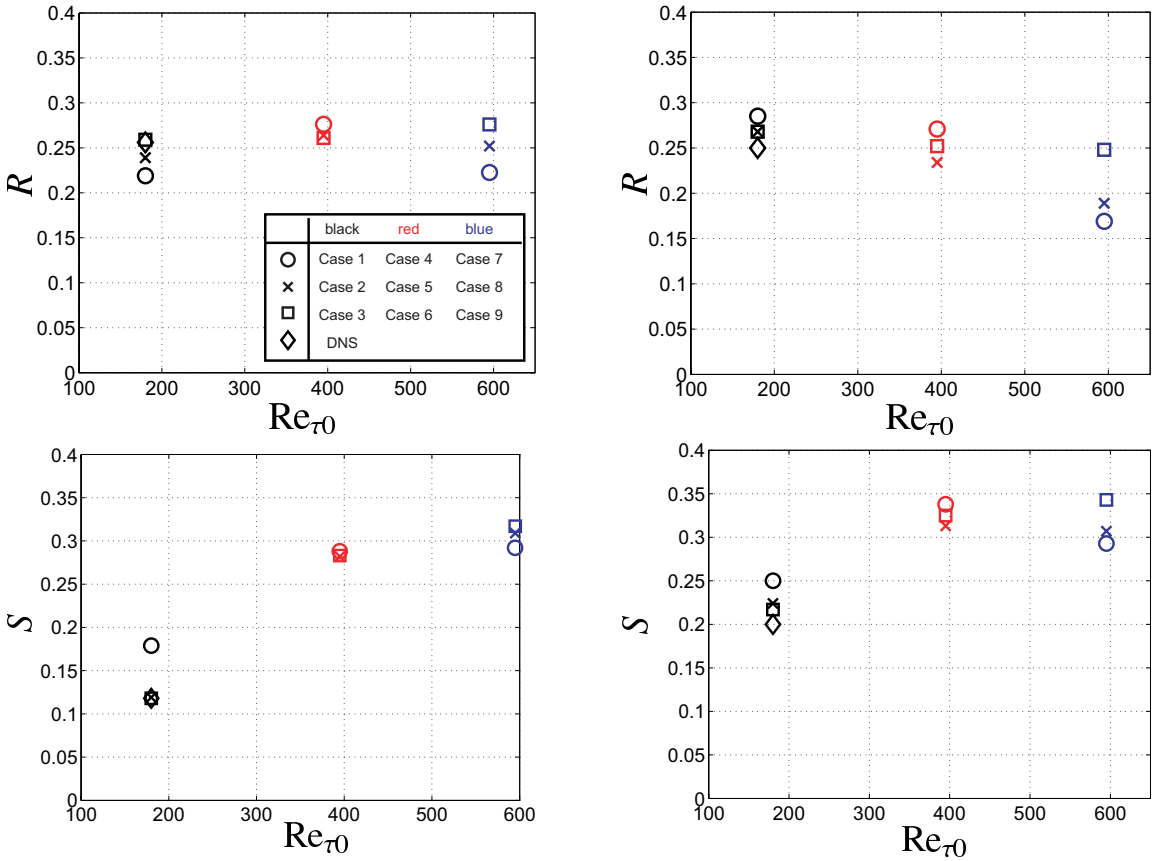

Figure 4.9: Drag reduction rate (top), R, and net saving rate (bottom), S as a function of friction Reynolds number: left, $c = -5.0$ and $k = 1.0$; right, $c = -3.0$ and $k = 1.0$.

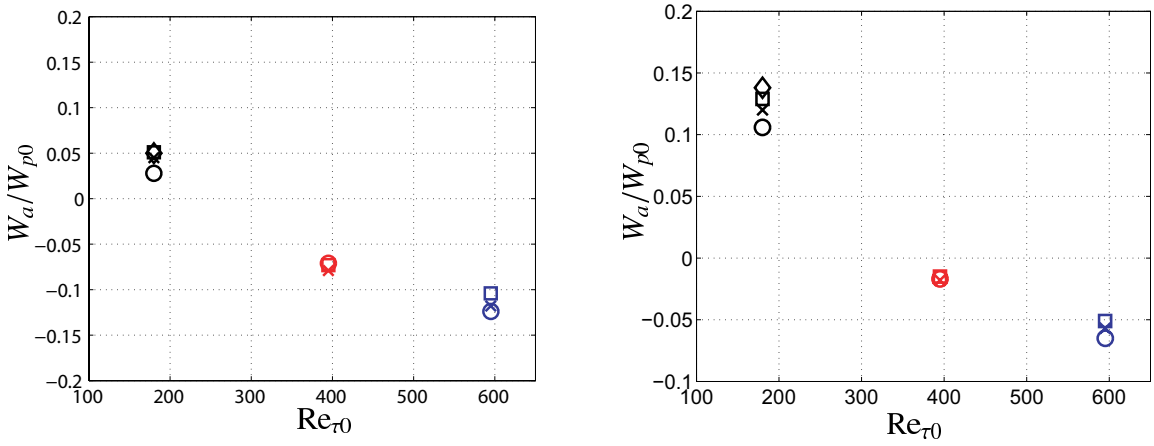

Figure 4.10: Normalized actuation work, W_a/W_{p0}, as a function of friction Reynolds number: left, $c = -5.0$ and $k = 1.0$; right, $c = -3.0$ and $k = 1.0$.

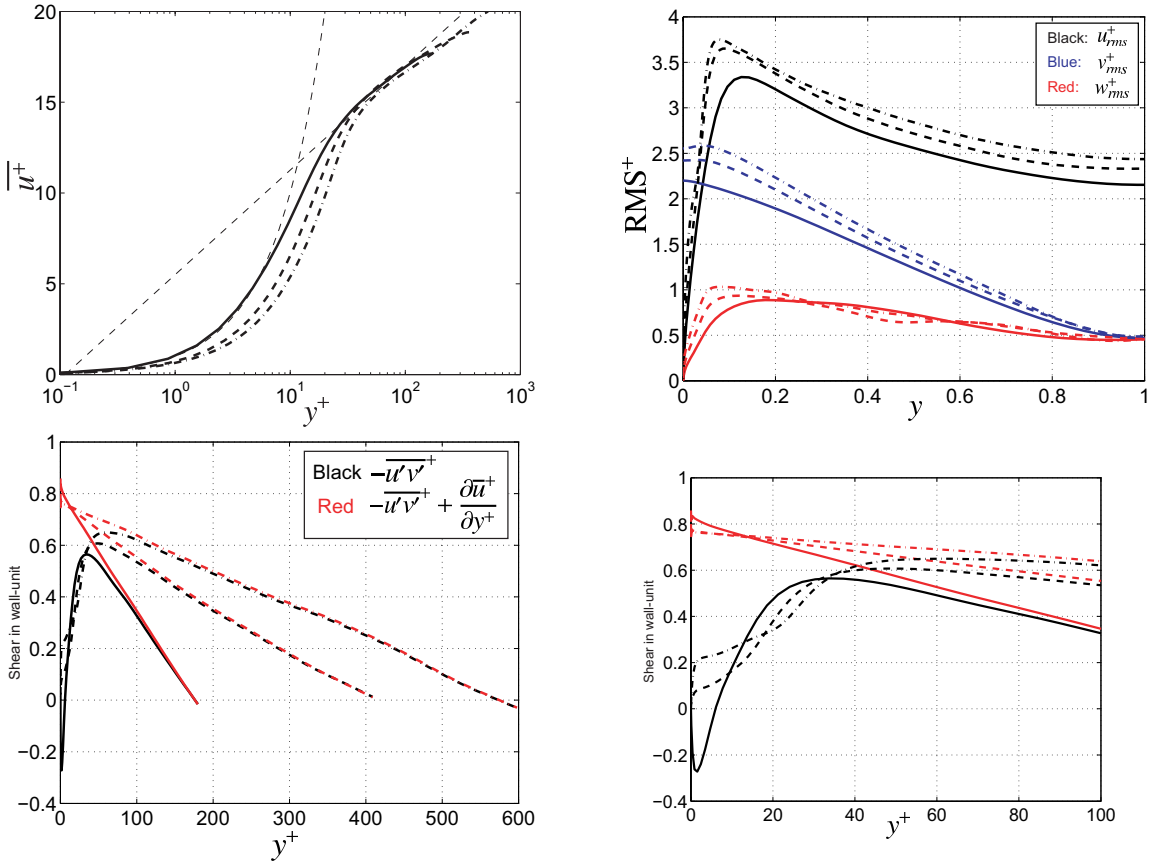

Figure 4.11: Reynolds number dependency of mean streamwise velocity (top, left), rms value of velocity fluctuations (top, right), Reynolds shear stress (bottom, left), and zoom-up view of the near-wall RSS (bottom, right): solid line, $\mathrm{Re}_\tau \approx 180$; broken line, $\mathrm{Re}_\tau \approx 395$; dashed-dotted line, $\mathrm{Re}_\tau \approx 595$. The input parameters are $c = -5.0$, $k = 1.0$, and $a = 0.1$.

Figure 4.11 shows the statistics at $c = -5.0$, $k = 1.0$, and $a = 0.1$ computed by using Case 1 for $\mathrm{Re}_{\tau 0} \approx 180$, Case 4 for $\mathrm{Re}_{\tau 0} \approx 395$, and Case 7 for $\mathrm{Re}_{\tau 0} \approx 595$. As increasing the Reynolds number, the near-wall velocity decreases in the buffer layer and the rms value of velocity fluctuations is found to increase. All RSS are found to decrease compared with uncontrolled RSS as shown in Fig. 4.6. The negative RSS appears in the region near the wall at $\mathrm{Re}_{\tau 0} \approx 180$, while it is positive at $\mathrm{Re}_{\tau 0} \approx 395$ and 595. Because the contribution from the far-wall region increases as increasing the Reynolds number, the drag reduction rate is almost unchanged, i.e., the sum of RSS and dU/dy is approximately 0.8 at $y^+ = 0$.

4.5 Summary

A series of the large eddy simulation with the coherent structure Smagorinsky model (Kobayashi, 2005) is presented for a fully developed turbulent channel flows at relatively high Reynolds numbers. The Reynolds number is set at $\mathrm{Re}_{\tau 0} \approx 177$, 395, and 595, and 1020.

Validation of the CSSM-LES code is made for the uncontrolled case. The mean velocity and shear balance are in reasonable agreement with the DNS data, while the rms velocity is not. This trend is due to the lack of modeling for the pressure-strain term.

As for the control effect of the *v*-control, the resultant maximum drag reduction rate is overestimated as compared to that of the DSM-LES. The maximum drag reduction rate, however, is found to decrease as increasing the Reynolds number.

As for the control effect of the traveling wave-like blowing/suction, the similar trend to the DNS result of Chap. 3 is obtained: the drag decreases by the upstream traveling wave, while it increases by the downstream traveling wave. The drag reduction rate is found to slightly decrease as increasing the Reynold number.

As increasing the Reynolds number, the contribution in the far-wall region to the skin-friction drag increases. Because the considered controls, i.e., the *v*-control and traveling wave-like blowing/suction, modify only the turbulence in the near-wall region, the effectiveness of drag reduction drops as increasing the Reynolds number.

Chapter 5

Conclusions

A series of numerical analyses for a traveling wave-like blowing/suction in a fully developed channel flow is presented. The effects due to this control are studied in a laminar flow, a turbulent flow at low and relatively high Reynolds numbers. Here, the important findings and major contributions of the present study are summarized.

5.1 Achievements

5.1.1 Laminar flow

The present linear analysis perfectly reproduced Min et al. (2006)'s results on the laminar channel flow. The detailed phase analysis and parametric study for wider range of input parameters revealed the mechanism of skin-friction drag reduction as follows:

1. the base phase relationship between the streamwise and wall-normal velocities agrees with that of the solution of inviscid flow;

2. the viscosity in the region near the wall induces phase shift of the streamwise velocity fluctuations and the sign of phase shift depends on the wave direction;

3. non-quadrature appears due to the combination of the base phase relationship and near-wall phase shift;

4. non-zero (negative) RSS is generated due to this non-quadrature;

5. the drag increment from the laminar value occurs because it is the integration of the y-weighted RSS.

The presented drag reduction mechanism is closer to the actual phenomena than that pointed out by Min et al. (2006). Additionally, the analogy with Stokes' problem is confirmed: the scaled influence layer thickness is kept constant regardless of the wave mode, wavenumber, wavespeed, and Reynolds number.

5.1.2 Turbulent flow at a low Reynolds number

An investigation is done by mean of direct numerical simulation of a fully developed turbulent channel flow under a constant flow rate at $\mathrm{Re}_{\tau 0} \approx 177$. The traveling wave-like blowing/suction is applied. It is found that the upstream traveling wave reduces skin-friction drag, whereas the downstream traveling wave increases it.

The upstream traveling wave decreases skin-friction drag and induces positive efficiency, while the downstream traveling wave does not. The upstream traveling wave creates the negative RSS in the region near the wall. The three-component decomposition reveals that the periodic-RSS is negative in the region near the wall and zero at far-wall region, while the random-RSS is positive in the whole channel but decreases below the uncontrolled level. The generation of this negative periodic-RSS is explained by the similar mechanism to that in Chap. 3. This mechanism is confirmed for wider range of parameter. On the other hand, the decrease of the random-RSS can be explained by the indirect effect due to the constraint of constant flow rate and the stabilization effect.

The traveling wave-like wall-normal forcing control is also considered. The standing wave is found to decrease the skin-friction drag in contrast to the traveling wave-like blowing/suction. This standing wave generates the spanwise roller-like vortex, which induces the negative periodic-RSS in the region near the wall. This spanwise roller-like vortex is observed not only in the turbulent flow, but also in the laminar flow.

5.1.3 Turbulent flow at higher Reynolds number

The control effect in relatively high Reynolds number turbulent flows is investigated by mean of large eddy simulation with the coherent structure Smagorinsky model

(Kobayashi, 2005) at $Re_{\tau 0} \approx 177$, 395, 595, and 1020. The resultant mean velocity and shear balance of the uncontrolled flow are found to be reasonable agreement with those of DNS, while the rms of velocity fluctuations is underestimated.

For the *v*-control, the maximum drag reduction rate is found to be larger than that presented by the dynamic Smagorinsky model (Chang et al., 2002). The maximum drag reduction rate decreases as increasing the Reynolds number, which is in accordance with the result of DSM-LES. For the traveling wave-like blowing/suction, a similar trend to that of DNS is obtained: skin-friction drag decreases (increases) by the upstream (downstream) traveling waves. The drag reduction rate by the upstream traveling wave is found to slightly decrease as increasing the Reynold number.

5.2 Direction for future research

Although the traveling wave-like blowing/suction control is attractive due to the large amount of drag reduction, positive efficiency, and simple control scheme, realization of this control is considered difficult. Actually, the existing devices induce blowing/suction in the traveling-wave form. At least, not only numerical studies but also experimental studies are needed. In that sense, the traveling wave-like wall-deformation control (Hoepffner and Fukagata, 2009; Nakanishi et al., accepted) has a possibility for realization. Very recently, Urano et al. (2011) studied the drag reduction effect in a channel, in which one side wall is vibrating in a traveling wave form, while another side is a plane wall. Another possibility is the wall-normal forcing by using a plasma actuator. In fact, DNS performed by Murai and Fukagata (2011) confirmed the drag reduction effect of the blowing device by using the opposed plasma actuator. This control effect is expected to be confirmed experimentally.

While we have only considered a channel flow, which is a one of internal flows investigation of the traveling wave-like control should be extended for an external flow. For example, Kametani (2009) studied the control effect by the traveling wave-like blowing/suction in a boundary layer flow: the resultant drag reduction effect, however, is found to be very small compared to the that of the uniform blowing (Kametani and Fukagata, 2011).

Large eddy simulation is a handy tool to investigate a high Reynolds number turbulent flow. The rms of velocities, however, is found to be overestimated or underestimated. This trend is the common both in the constant and dynamic Smagorinsky models. Because the pressure-strain term is not modeled, while only the SGS stress is modeled by the eddy viscosity, redistribution of energy among each velocity component can not be captured. This point should be mentioned in order to improve the existing model in the future. Additionally, a model which can predict controlled flows should be developed.

As increasing the Reynolds number, effectiveness of drag reduction by the considered control is found to decrease because the contribution to the skin-friction drag from Reynolds shear stress in the far-wall region increases. Therefore, control should be designed to modify turbulence not only in the near-wall region but also in the far-wall region.

Bibliography

Abe, H., Kawamura, H., Matsuo, Y., 2004. Surface heat-flux fluctuations in a turbulent channel flow up to Re_τ = 1020 with Pr = 0.025 and 0.71. Int. J. Heat Fluid Flow 25, 404–419.

Abergel, F., Temam, R., 1990. On some control problem in fluid mechanics. Theor. Comput. Fluid Dyn. 1, 303–325.

Auteri, F., Baron, A., Belan, M., Campanardi, G., Quadrio, M., 2010. Experimental assessment of turbulent drag reduction by traveling waves in a turbulent pipe flow. Phys. Fluids 22, 115103.

Berger, T. W., Kim, J., Lee, C., Lim, J., 2000. Turbulent bounday layer control utilizing the Lorenz force. Phys. Fluids 12, 631.

Bewley, T., 2009. A fundamental limit on the balance of power in a transpiration-controlled channel flow. J. Fluid Mech. 632, 443–446.

Bewley, T. R., 1999. Optimal and robust control and estimation of transition, convection, and turbulence. Ph.D. thesis, Stanford University.

Bewley, T. R., 2001. Flow control: new challenges for a new renaissance. Prog. Aerospace Sci. 39, 1579–1606.

Bewley, T. R., Aamo, O. M., 2004. A win-win mechanism for long-drag transients in controled two-dimensinal channel flow and its implication for sustained drag reduction. J. Fluid Mech. 499, 183–196.

Bewley, T. R., Moin, P., Temam, R., 2001. DNS-based predictive control of turbulence: an optimal benchmark for feedback algorithms. J. Fluid Mech. 447, 179–225.

Cambon, C., Scott, J. F., 1999. Linear and nonlinear models of anisotropic turbulence. Annu. Rev. Fluid Mech. 31, 1–53.

Cattafesta III, L. N., Sheplak, M., 2011. Actuators for active flow control. Annu. Rev. Fluid Mech. 43, 247–272.

Chang, Y., Collis, S., Ramakrishnan, S., 2002. Viscous effects in control of near-wall turbulence. Phys. Fluids 14, 4069–4080.

Choi, H., Moin, P., Kim, J., 1993. Direct numerical simulation of turbulent over the riblets. J. Fluid Mech. 255, 503–539.

Choi, H., Moin, P., Kim, J., 1994. Active turbulence control for drag reduction wall-bounded flows. J. Fluid Mech. 262, 75–110.

Choi, J.-l., Xu, C.-X., Sung, Y. H., 2002. Drag reduction by spanwise wall oscillation in wall-bounded turbulent flows. AIAA J. 40, 842–850.

Chung, M. Y., Talha, T., 2011. Effectiveness of active flow control for turbulent skin friction drag reduction. Phys. Fluids 23, 025102.

Collis, S. S., Chang, Y., Kelloggz, S., Prabhux, R., 2000. Large eddy simulation and turbulence control. AIAA Paper, 2000–2564.

Corke, T. C., Post, M. L., Orlov, D. M., 2009. Single dielectric barrier discharge plasma enhanced aerodynamics: physics, modeling and applications. Exp. Fluids 46, 1–26.

Desjardins, O., Blanquart, G., Balarac, G., Pitsch, H., 2008. High order conservative finite difference scheme for variable density low mach number turbulent flows. J. Comput. Phys. 227, 7125–7159.

Drazin, P. G., Reid, W. H., 1981. Hydrodynamic Stability. Cambridge.

Du, Y., Karniadakis, G. E., 2000. Suppresssing wall turbulance by means of a transverse traveling wave. Science 288, 1230–1234.

Du, Y., Symeonidis, V., Karniadakis, G. E., 2002. Drag reduction in wall-bounded turbulance via a transverse traveling wave. J. Fluid Mech. 457, 1–34.

Endo, T., Himeno, R., 2002. Direct numerical simulation of turbulent flow over a compliant surface. J. Turbulence 3, 007.

Endo, T., Kasagi, N., Suzuki, T., 2000. Feedback control of wall turbulence with wall deformation. Int. J. Heat Fluid Flow 21, 568–575.

Fukagata, K., 2011. Drag reduction by wavy surfaces. J. Fluid Sci. Technol. 6, 2–13.

Fukagata, K., Iwamoto, K., Kasagi, N., 2002. Contribution of Reynolds stress distribution to the skin friction in wall-bounded flows. Phys. Fluids 14, L73–L76.

Fukagata, K., Iwamoto, K., Kasagi, N., 2005a. Novel turbulence control strategy for simultaneously achieving friction drag reduction and heat transfer augmentation. In: Proc. 4th Int. Symp. Turbulence and Shear Flow Phenomena, Williamsburg. pp. 307–312.

Fukagata, K., Kasagi, N., 2002. Highly energy-conservative finite difference method for the cylindrical coordinate system. J. Comput. Phys. 181, 478–498.

Fukagata, K., Kasagi, N., 2003. Drag reduction in turbulent pipe flow with feedback control applied partially to wall. Int. J. Heat Fluid Flow 24, 480–490.

Fukagata, K., Kasagi, N., 2004. Suboptimal control for drag reduction via suppression of near-wall Reynolds shear stress. Int. J. Heat and Fluid Flow 25, 341–350.

Fukagata, K., Kasagi, N., Koumoutsakos, P., 2006. A theoretical prediction of friction drag reduction in turbulent flow by superhydrophobic surfaces. Phys. Fluids 18, 051703.

Fukagata, K., Kasagi, N., Sugiyama, K., 2005b. Feedback control achieving sublaminar friction drag. In: Proc. 6th Symp. on Smart Control of Turbulence. pp. 143–148.

Fukagata, K., Kern, S., Chatelain, P., Koumoutsakos, P., Kasagi, N., 2008. Evolutionary optimization of an anisotropic compliant surface for turbulent friction drag reduction. J. Turbulence 9, N35, 1–17.

Fukagata, K., Sugiyama, K., Kasagi, N., 2009. On the lower bound of net driving power in controlled duct flows. Physica D. 238, 1082–1086.

Fukagata, K., Yamada, S., Ishilawa, H., 2010. Plasma actuators: fundamentals and research trends. Nagare 29, 243–250 (in Japanese).

Gad-el-Hak, M., 1994. Interactive control of turbulent boundary layers: A futuristic overview. AIAA J. 32, 1753.

Gad-el-Hak, M., 1996. Modern development in flow control. Appl. Mech. Rev. 49, 365–379.

Germano, M., Piomelli, U., Moin, P., Cabot, H., 1991. A dynamic subgrid-scale eddy viscosity model. Phys. Fluids A 3, 1760–1765.

Gomez, T., Flutet, V., Sagout, P., 2009. Contribution of Reynolds stress distribution to the skin friction in compressible turbulent. Phys. Rev. E 79, 035301.

Ham, F. E., Lien, F. S., Strong, A. B., 2002. A fully conservative second-order finite difference scheme for incompressible flow on nonuniform grids. J. Comput. Phys. 177, 117–133.

Hamilton, J. M., Kim, J., Waleffet, F., 1994. Regeneration mechanisms of near-wall turbulence structures. J. Fluid Mech. 287, 317–348.

Hammond, E. P., Bewley, T. R., Moin, P., 1998. Observed mechanisms for turbulence attenuation and enhancement in opposition-controlled wall-bounded flows. Phys. Fluids 10, 2421.

Harlow, F. H., Welch, J. E., 1965. Numerical calculation of time-dependent viscous incompressible flow of fluid with free surface. Phys. Fluids 8, 2182–2189.

Hasegawa, Y., Kasagi, N., 2011. Dissimilar control of momentum and heat transfer in a fully developed turbulent channel fow. J. Fluid Mech. 683, 57–93.

Higashi, K., Mamori, H., Fukagata, K., in press. Simultaneous control for friction drag reduction and heat transfer augmentation by traveling wave-like blowing/suction. Comput. Therm. Sci.

Hoepffner, J., Fukagata, K., 2009. Pumping or drag reduction? J. Fluid Mech. 635, 171–187.

Hoyas, S., Jimenez, J., 2006. Scaling of the velocity fluctuations in turbulent channels up to Re_τ= 2003. Phys. Fluids 18, 011702.

Hussain, A. K. M. F., Reynolds, W. C., 1970. The mechanics of an organized wave in turbulent shear flow. J. Fluid Mech. 41, 241–258.

Iwamoto, K., Fukagata, K., Kasagi, N., Suzuki, Y., 2004. DNS of turbulent channel flow at Re_τ = 1160 and evaluation of feedback control at practical Reynolds numbers. In: Proc. 5th Symp. on Smart Control of Turbulence. pp. 327–333.

Iwamoto, K., Kasagi, N., Suzuki, Y., 2005. Direct numerical simulation of turbulent channel flow at Re_τ = 2320. In: Proc. 6th Symp. on Smart Control of Turbulence.

Iwamoto, K., Koshi, M., Murata, A., Fukagata, K., 2009. On the identity equation between skin-friction coefficient and Reynolds shear stress for plane boundary layer. In: Proc. 2009 Annual Meeting of Japan Society of Fluid Mechanics. Paper No. 35024.

Iwamoto, K., Suzuki, Y., Kasagi, N., 2002. Reynolds number effect on wall turbulence: toward effective feedback control. Int. J. Heat Fluid Flow 23, 678–689.

Javanovic, M. R., Moarref, R., You, D., 2006. Turbulence suppression in channel flows by means of a streamwise traveling wave. pp. 481–494.

Jimenez, J., Moin, P., 1991. The minimal flow unit in near-wall turbulence. J. Fluid Mech. 225, 213–240.

Kajishima, T., 1999a. Finite-difference method for convective terms using non-uniform grid. Trans. JSME/B 633, 1607–1623 (in Japanese).

Kajishima, T., 1999b. Numerical simulation of turbulent flows. Yoken-do (in Japanese).

Kametani, Y., 2009. Numerical simulation of friction drag reduction control in spatially developing turbulent boudnary layer. Master's thesis, Keio Univ. (in Japanese).

Kametani, Y., Fukagata, K., 2011. Direct numerical simulation of spatially developing turbulent boundary layer with uniform blowing or suction. J. Fluid Mech. 681, 154–172.

Kang, S., Choi, H., 2000. Active wall motions for skin-friction drag reduction. Phys. Fluids 12, 3301–3305.

Karniadakis, G. E., Choi, K.-S., 2003. Mechanism on transverse motion in turbulent wall flow. Annu. Rev. Fluid Mech. 35, 45–62.

Kasagi, N. (Ed.), 2009. Turbulent flow enegineering handbook. Asakura shoten (in Japanese).

Kasagi, N., Hasegawa, Y., Fukagata, K., Sept. 7-10 2009a. Toward cost-effective control of wall turbulence for skin friction drag reduction. In: Proc. 12th EUROMECH European Turbulence Conference. Marburg, pp. 189–200.

Kasagi, N., Hasegawa, Y., Fukagata, K., Iwamoto, K., 2012. Control of turbulent transport: Less friction and more heat transfer. J. Heat Transfer 134, 031009, 10 pp.

Kasagi, N., Sumitani, Y., Suzuki, Y., Iida, O., 1995. Kinematics of the quasi-coherent vortical strucure in near-wall turbukence. Int. J. Heat Fluid Flow 16, 2–10.

Kasagi, N., Suzuki, Y., Fukagata, K., 2009b. Microelectromechanical system-based feedback control of turbulence for skin friction drag. Annu. Rev. Fluid Mech. 41, 231–251.

Kawamura, H., 1995. Direct numerical simulation of turbulence by finite difference scheme. The Recent Developments in Turbulence Research, Int. Academic Publishers.

Kim, J., 2011. Physics and control of wall turbulence for drag reduction. Phil. Trans. R. Soc. A 369, 1396–1411.

Kim, J., Moin, P., Moser, R., 1987. Turbulent statistic in fully developed channel flow at low Reynolds number. J. Fluid Mech. 177, 133–166.

Kobayashi, H., 2005. The subgrid-scale models based on coherent structure for rotating homogeneous turbulence and turbulent channel flow. Phys. Fluids 17, 045104.

Koumoutsakos, P., 1998. Vorticity flux control for a turbulent channel flow. Phys. Fluids 11, 248–250.

Launder, B. E., Reece, G. J., Rodi, W., 1975. Progress in the development of a Reynolds stress turbulence closure. J. Fluid Mech. 68, 537–566.

Le Dauphin, C., Fukagata, K., 2011. Opposition control of turbulent taylor-couette flow. In: Proc. ASME-JSME-KSME Joint Fluids Engineering Conf. 2011 (AJK2011). Paper AJK2011-25007, 9 pp.

Lee, C., Kim, J., Choi, H., 1998. Suboptimal control of turbulent channel flow for drag reduction. J. Fluid Mech. 358, 245–258.

Lee, C., Kim, J., D., B., Goodman, R., 1997. Application of neural networks to turbulence control for drag reduction. Phys. Fluids 9, 1740–1747.

Lee, C., Min, T., Kim, J., 2008. Stability of a channel flow subject to wall blowing and suction in the forme of a traveling wave. Phys. Fluids 20, 101513.

Li, F.-C., Kawaguchi, Y., Yu, B., Wei, J.-J., Hishida, K., 2008. Experimental study of drag-reduction mechanism for a dilute surfactant solution flow. Int. J. Heat and Mass Transfer 51, 835–843.

Lieu, B. K., Moaddref, R., Jovanovic, M. R., 2010. Controlling the onset of the turbulence by stremwise traveling waves. part. 2. direct numrical simulation. J. Fluid Mech. 663, 100–119.

Lighthill, S. J., 1978. Acoustic streaming. J. Sound Vib. 61, 391–418.

Lilly, D. K., 1967. The representation of small-scale turbulence in numerical simulation. IBM Form, 195–210.

Lilly, D. K., 1992. A proposed modification of the germano subgrid-scale closure method. Phys. Fluids A 4, 633–635.

Luchini, P., 2008. Acoustic streaming and lower-than-laminar drag in controlled channel flow.

Mamori, H., Fukagata, K., Hoepffner, J., Obi, S., 2009. Drag reduction in channel flow by traveling wave-like surface heating/cooling. In: Proc. 6th Int. Symp. on Turbulence and Shear Flow Phenomena. pp. 581–586.

Mansour, N. N., Kim, J., Moin, P., 1988. Reynolds-stress and dissipation-rate budgets in a turbulent channel flow. J. Fluid Mech. 194, 15–44.

Martell, M. R., Perot, J. B., P., R. J., 2009. Direct numerical simulation of turbulent flows over superhydrophobic surface. J. Fluid Mech. 620, 31–41.

Martell, M. R., Rothstein, J. P., Perot, J. B., 2010. An analysis of superhydrophobic turbulent dra reduction mechanisms using direct numerical simul. Phys. Fluids 22, 065102.

Marusic, I., Joseph, D. D., Mahesh, K., 2007. Laminar and turbulent comparisons for channel flow and flow control. J. Fluid Mech. 570, 467–477.

Min, T., Kang, S. M., Speyer, J. L., Kim, J., 2006. Sustained sub-laminar drag in a fully developed channel flow. J. Fluid Mech. 558, 309–318.

Moarref, R., Jovanovic, M. R., 2010. controlling the onset of turbulence by stremwise traveling waves. part1. receptivity analysis. J. Fluid Mech. 663, 70–99.

Moin, P., Bewley, T., 1994. Feedback control of turbulence. Appl. Mech Rev. 47, S3–S13.

Morinishi, Y., Lund, T. S., Vasilyev, O. V., Moin, P., 1998. Fully conservative higher order finite difference scheme for incompressible flow. J. Comput. Phys. 143, 90–124.

Morinishi, Y., Vasilyev, O. V., Ogi, T., 2004. Fully conservative finite difference scheme in cylindrical coordinates for incompressible flow simulations. J. Comput. Phys. 197, 686–710.

Moser, R. D., Kim, J., Mansour, N. N., 1999. Direct numerical simulation of turbulent channel flow up to Re_τ=590. Phys. Fluids 11, 943.

Murai, Y., Fukagata, K., 2011. Direct numerical simulation of turbulent friction drag reduction by traveling wave-like blowing using plasma actuator. In: Proc. ASME-JSME-KSME Joint Fluids Engineering Conf. 2011 (AJK2011).

Nakanishi, R., Mamori, H., Fukagata, K., accepted. Relaminarization of turbulent channel flow using traveling wave-like wall deformation. Int. J. Heat Fluid Flow.

Nikitin, N., 2006. Finite-difference method for incompressible navier-stokes equations in arbitrary orthogonal curvilinear coordinates. J. Comput. Phys. 217, 759–791.

Oishi, Y., Murai, Y., Tasaka, Y., Takeda, Y., 2009. Frictional drag reduction by wavy advection of deformable bubbles. J. Phys.: Conf. Ser. 147, 012020.

Orszag, S. A., Patterson, G. S., 1972. Numerical simulation of three-dimensional homogeneous isotropic turbulence. Phys. Rev. Lett. 28, 76–79.

Piacsek, S. A., Williams, G. P., 1970. Conservation properties of convection difference sheme. J. Comput. Phys. 6, 392–405.

Quadrio, M., Floryan, J. M., Luchini, P., 2007. Effect of stremwise-periodic wall transpriation on turbulent friction drag. J. Fluid Mech. 576, 425–444.

Quadrio, M., Ricco, P., Viotti, C., 2009. Streamwise-travelling waves of spanwise wall velocity for turbulent drag reduction. J. Fluid Mech. 627, 161–178.

Rebbeck, H., Choi, K.-S., 2006. A wind-tunnel experiment on real-time opposition control of turbulance. Phys. Fluids 18, 035103.

Ricco, P., Quadrio, M., 2008. Wall-oscillation conditions for drag reduction in turbulent channel flow. Int. J. Heat Fluid Flow 29, 601–612.

Riley, N., 2001. Steady streaming. Annu. Rev. Fluid Mech. 33, 43–65.

Robinson, S. K., 1991. Coeherent motions in the trubulent boundary layer. Annu. Rev. Fluid Mech. 23, 601–639.

Rothstein, J. P., 2009. Slip on superhydrophobic surfaces. Annu. Rev. Fluid Mech. 42, 89–109.

Sbragaglia, M., Sugiyama, K., 2007. Boundary induced nonlinearities at small Reynolds numbers. Physica D 228, 140–147.

Schmid, P. J., Hennningson, D. D., 2000. Stability and Transition in Shear Flow. Springer.

Shen, L., X., Z., Yue, Y. P., S., T. M., 2003. Turbulent flow over a flexible wall undergoing a streamwise travelling wave motion. J. Fluid Mech. 484, 197–221.

Shyy, W., Jayaraman, B., Andersson, A., 2002. Modeling of glow discharge-induced fluid dynamics. J. Appl. Phys. 92, 6434–6443.

Sirovich, L., Karlsson, S., 1997. Turbulent drag reduction by passive mechanisms. Nature 1997, 753–755.

Smagorinsky, J., 1963. General circulation experiments with the primitive equations. Mon. Weath. Rev. 91, 99–164.

Smith, C. R., Metzler, S. P., 1983. The characteristics of low-speed streaks in the near-wall region of a turbulent boundary layer. J. Fluid Mech. 129, 27–54.

Smits, A. J., McKeon, B. J., Marusic, I., 2011. High-Reynolds number wall turbulence. Annu. Rev. Fluid Mech. 43, 353–375.

Suzuki, T., Kawamura, H., 1994. Consistency of finite-difference scheme in direct numerical simulation of turbulence. Trans. JSME/B 60, 3280–3286.

Takada, M., 2010. The suboptimal control based on Reynolds stress transport equation for the turbulent skin friction drag redcuction. Bachelor's thesis, Keio Univ.(in Japanese).

Taneda, S., Tomonari, Y., 1973. An experiment on the flow around a waving plate. J. Phys. Soc. Jpn. 36, 1683–1689.

Urano, S., Iwamoto, K., Murata, A., 2011. Experimental study of turbulent channel flow on traveling wavy wall for drag reduction. In: Annual Meeting of Japan Society of Fluid Mechanics, Tokyo. (in Japanese).

Walsh, M. J., 1983. Riblets as a viscous drag reduction technique. AIAA J. 21, 485–486.

Weidman, J. A. C., Reddy, S. C., December 2000. A matlab differentiation matrix suite. ACM Trans. Math. Software 26 (4), 465–519.

White, C. M., Mungal, M. G., 2008. Mechanics and prediction of turbulent drag reduction with polymer additives. Annu. Rev. Fluid Mech. 40, 235–256.

White, F. M., 2006. Viscous Fluid flow. McGraw-Hill.

Woodcock, J. D., Sader, J. E., Marusic, I., 2012. Induced flow due to blowing and suction flow control: An analysis of transpriation. J. Fluid Mech. 690, 366–398.

Xu, S., Rempfer, D., Lumley, J., 2003. Turbulence over a compliant surface: numerical simulation and analysis. J. Fluid Mech. 478, 11–34.

Yakeno, A., Hasegawa, Y., Kasagi, N., 2010. Mechanism of drag reduction by predetermined spatio-temporally periodic control of wall turbulence. Trans. JSME/B 76, 555–562.

Yang, D., Shen, L., 2009. Characteristics of coherent vortical structures in turbulent flows over progressive surface waves. Phys. Fluids 21, 125106.

Yoon, H. S., El-Samni, O. A., Chun, H. H., 2006. Drag reduction in turbulent channel flow with periodically arrayed heating and cooling strips. Phys. Fluids 18, 025104.

Yoshino, T., Suzuki, Y., Kasagi, N., 2008. Drag reduction of turbulance air channel flow with distributed micro sensors and actuatiors. J. Fluid Sci. Technol. 3, 137–148.

During this thesis had been written,
huge earthquake and a tunami induced by it hit north east of Japan.
I would like to express my sympathy to the decreased due to this disaster.